Superconducting Resonators on Thin Film Flexible Substrates

by

Rujun Bai

A dissertation submitted to the Graduate Faculty of
Auburn University
in partial fulfillment of the
requirements for the Degree of
Doctor of Philosophy

Auburn, Alabama
December 10, 2016

Keywords: superconductor, resonator, Kapton, polyimide (PI-2611 and HD-4100)

Approved by

Michael C. Hamilton, Chair, Associate Professor of Electrical and Computer Engineering
Fa Foster Dai, Professor of Electrical and Computer Engineering
Lloyd S. Riggs, Professor of Electrical and Computer Engineering
Michael E. Baginski, Associate Professor of Electrical and Computer Engineering
Minseo Park, Professor of Physics

Abstract

In cryogenic electronics applications and experiments, i.e., for cold detectors and low temperature quantum computing, the base temperature is typically below 100 milli-Kelvin. In order to reach this temperature range, a significant effort is undertaken to reduce the thermal load of the system by using microwave and dc cables with a low thermal conductivity. As the number of connections increase in superconducting cryogenic computers, the more difficult it becomes to cool the system down. One practical solution to address this issue is to reduce the cross-sectional area of the cables used in the cryogenic system. For cryogenic cables and interconnects that deliver microwave signals, we want low loss dielectric materials to interface different kinds of microwave devices, especially superconductor devices. Therefore, we want to minimize losses in the substrate by selectively choosing dielectrics that are low-loss and mechanically compliant when used as free-standing flex cables.

Half-wavelength, capacitively coupled superconducting microstrip resonators have been constructed on various flexible substrates including 50.8 μm (2 mil) thick free-standing Kapton polyimide and 20 μm thick spin-on polyimide. Cu normal conducting and Nb superconducting resonators were designed and fabricated on these substrates. We extracted the complex dielectric permittivity of the films over a wide frequency range and at cryogenic temperatures below 9 K. In order to better characterize these thin and low loss dielectric films, we require high-quality factor resonators to allow extraction of the dielectric properties. We designed these resonators to be weakly coupled to reduce the coupling loss, this involved several iterative designs and measurements at cryogenic temperatures. The metal stack-up of these superconducting resonators mainly consisted of a 250 nm thick superconducting Nb film to limit conductor loss. The fabricated resonators exhibited high-quality factors (Q) at a temperature of ~1.2 K of 7000 for E-series Kapton film, 13 000 for a spin-on PI-2611 and

17 000 for a spin-on HD-4100 in the 2-10 GHz frequency range. These results imply the loss tangent of all the materials measured is less than 0.00016 at 2 GHz. These high-Q measurement results provide evidence that spin-on polyimide film, as well as commercially available Kapton can be potentially useful as a microwave substrate material for flexible superconducting interconnects or cables, which are of great interest for use in cryogenic electronics systems.

In this work, we also investigated how different under layers and capping layers of the Nb films impacted the conductor losses in the GHz frequency range. We mainly studied how the different thickness of a Ti (10 and 50 nm) under-layer for adhesion impacted the superconductor losses. This is important, as Ti is a commonly used metal for adhesion to various substrate materials. We also studied Cu (10, 50, 100, and 200 nm) capping layers and how they affect the conductor loss. Conductor loss studies were carried out on 20 μm thick spin on polyimide (PI-2611) films and were characterized at different cryogenic temperatures. The results indicate normal-to-superconductor (Ti/Nb) and superconductor-normal (Nb/Cu) bi-layer structures have more surface resistance, which leads to an increase of RF loss when compared to “bare” Nb conductor traces. We quantified this additional loss by measuring Q-factors at different cryogenic temperatures (4.2 K, 3.6 K, 3.0 K, and 1.2 K). This work provides experimental support for the fabrication and performance of bi-layer normal-superconducting structures on these types of thin dielectric films.

Lastly, we investigated embedded superconducting resonators on thin polyimide (PI-2611 and HD-4100). We built a series of embedded superconducting edge coupled half-wavelength microstrip transmission line resonators (MTLR) with a top layer dielectric that was half of the thickness of the bottom dielectric. These resonators provided useful information for building other multi-layer polyimide based microwave structures such as stripline transmission lines and stripline resonators that are expected to be fabricated in future efforts. From these measurement results, we determined superconducting Nb film quality can be degraded during the top polyimide layer curing process, even at a reduced curing temperature of 225°C. We observed that an Al/Nb/Al (20 nm/250 nm/20 nm) metal stack-up can effectively prevent this degradation from occurring. We expect that the degradation is related to oxidation of the thin Nb due to exposure to H_2O or O_2, though determination of the exact mechanism was not the focus of this work. These experiments were studied on both types of polyimide PI-2611 (low-stress) and HD-4100 (photo-definable). Both of these films exhibited similar results, which leads to the conclusion that Al/Nb/Al metal-stackup may be useful for more complex multi-layer structures, such as stripline.

Acknowledgments

Foremost, I would like to express my sincere gratitude to my advisor Dr. Hamilton and to Dr. Tuckerman for their guidance in conducting this research and for the financial support in pursuit of this degree. Their instruction helped foster a deep understanding of the work undertaken and helped me to become a better researcher. The success of this work would not have been possible without the extensive laboratory support from Dr. Ellis, Mr. Baugh, and Ms. Yang Cao.

I also extend my gratitude and appreciation to my dissertation committee: Dr. Fa Foster Dai, Dr. Lloyd Riggs, Dr. Michael Baginski, and Dr. Minseo Park, for their help in reviewing my dissertation, insightful comments, and suggestions.

I sincerely thank my lab mate George A. Hernandez for providing insight into the fabrication processes and countless discussions of this work. I also thank for my lab mates, Dr. Pingye Xu, Dr. Phillip Bailey, Mr. Jordan Hullett who were always open to discussions about my ongoing research. Lastly, I thank all my friends in Auburn who helped me successfully conquer the many difficulties encountered through my pursuit of this degree.

Lastly, and most importantly I wish to thank my parents, Shiyu Bai and Peiyan Li for their consistent support, understanding and encouragement. I would like to dedicate this dissertation to my parents.

Table of Contents

List of Figures

List of Tables

List of Abbreviations

$\Delta(0)$	Energy gap at T 0 K
ϵ_r	Relative permittivity (Dielectric constant)
λ_L	London penetration depth
ξ	Coherence length
k_B	Boltzmann constant
L_k	Kinetic inductance
Q_c	Quality factor related to conductor loss
Q_d	Quality factor related to dielectric loss
Q_{extra}	Extra quality factor
Q_{unload}	Unloaded quality factor
R_s	Surface resistance
R_{sq}	Sheet resistance
S_{21}	Insertion loss
T_c	Critical temperature
Z_s	Surface impedance
ADS	Advance Design System
BCS	Bardeen Cooper Schrieffer

CBCPW	Conductor backed coplanar wave guide
CPW	Coplanar wave guide
dc	Direct current
E-beam	Electron-beam physical evaporation
GL	Ginzburg-Landau
LCP	Liquid crystalline polymer
MKID	Microwave kinetic inductance detector
MTLR	Half-wavelength microstrip transmission line resonator
Polyimide	PI-2611, HD-4100
PT	Pulse tube
Q	Quality factor (loaded Q)
QED	Quantum electrodynamics
qubits	Quantum bits
RF	Radio frequency
RT	Room temperature
UBM	Under bump metal

Chapter 1

Introduction

1.1 Scientific motivation

Recently, cryogenic computing, especially quantum computing, has had a rapid development. The operation temperature of these quantum computing devices is usually in the milli-Kelvin range by using a dilution refrigerator. Currently, most research groups using coaxial cables to transfer microwave signal since it not only can provide a good microwave performance but it is also easy to make connections with other microwave devices. But most of the RF coaxial cables introduce a significant thermal load, which will extend the system cooling time and limited the number of connections between temperature stages. Some of the cryogenic coaxial cables have low thermal loads but very high conductor resistance, which result in high transmission losses. Additionally, the physical volume capacity of the dilution refrigerator is limited. One of the solutions to this problem is to reduce the cross sectional area of these cables to reduce the thermal load on the cryogenic system and shrink the size of the cables. If we can build microwave transmission lines on thin film dielectrics, it will significantly reduce the substrate cross section area compared to currently used coaxial cables. Furthermore, this can allow us to build high-density multi-signal transmission lines cables with limited crosstalk on the thin film dielectric. An overall goal of this project was to build superconducting microwave transmission line flexible cables with a reduced thermal footprint and minimal RF attenuation to be used in deep cryogenic systems.

Therefore, it is important to characterize the dielectric properties, such as loss tangent and dielectric constant of the different materials of interest. The dielectric constant information of these thin film dielectrics at cryogenic temperature can help us make appropriate microwave transmission line designs. The loss tangent value of these materials will help us estimate the transmission loss in these cables as a function of frequency. For cryogenic computing, we want a mechanically robust dielectric substrate material with minimal losses that can lead to the best microwave performance of these superconducting flexible cables. Therefore, we purposefully built a series of superconducting flexible resonators on the different types of dielectrics and characterized them at cryogenic temperatures and at frequencies up to 20 GHz.

1.2 Important concepts for low temperature superconductors

A superconductor is an element or metallic alloy in which the dc resistance goes to zero when the temperature is decreased below a certain critical transition temperature (T_c). There are different ways to classify superconductors such as by their response to magnetic field (Type I and Type II), by a theory to explain the superconductivity (conventional and un-conventional), by their critical temperature, or by its material parameters (single elements, alloys, ceramics...), etc. If we classify a superconductor by critical temperature, it can be classified as a high-temperature superconductor (HTS) when the critical temperature is above the liquid nitrogen temperature of 77 K and as a low-temperature superconductor (LTS) when critical temperature is below 77 K [1,2].

Most pure metals show superconductivity when the temperature is below their T_c as shown in Figure 1.1 [3]. The exceptions include good conductors such as copper, silver, and gold, noble metal as well as magnetic materials shown as white in Figure 1.1. Material such as copper, silver, and gold do not exhibit superconductivity at any temperature due to the inability of these metals to form Cooper pairs [4]. Cooper pairs are electrons bound by an electron-phonon interaction with a material-dependent binding energy. At temperatures below T_c, the Cooper pairs carry a super current that exhibits no dc loss. To break a pair, the excitation energy is expressed in equation 1.1:

$$2\Delta = 3.5 k_B T_c \tag{1.1}$$

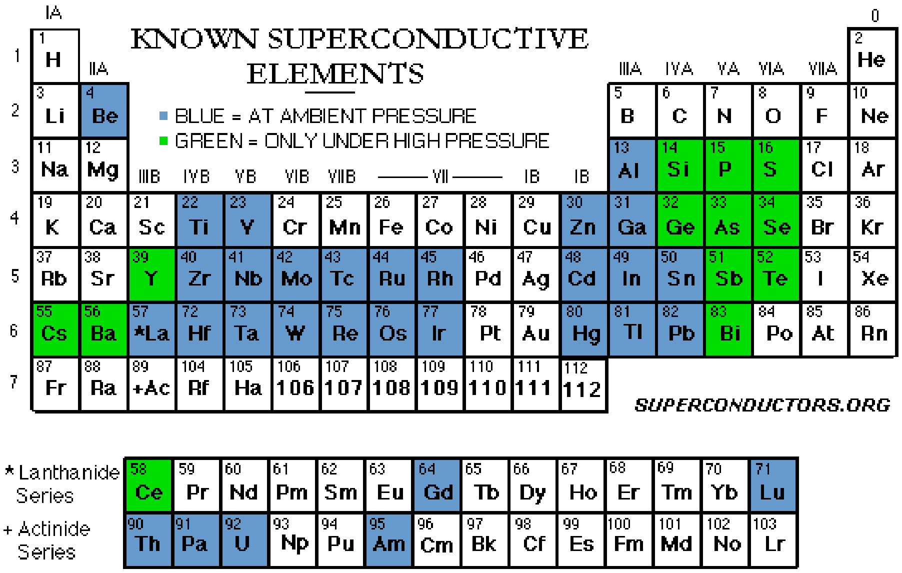

Figure 1.1: Periodic table of known superconductor elements. Adapted from [5].

where T_c is the superconducting transition temperature. Δ is the gap energy of the superconductor, and k_B is Boltzmann constant. This relationship is true for temperatures well below T_c.

1.2.1 Surface impedance

When the temperature is below T_c, the dc current travels through the superconductor without any resistance. For ac current, there is a nonzero impedance. If an electric field is applied near the surface of a superconductor, it will cause the Cooper pairs to accelerate converting their motion into a kinetic energy. Since there is no dissipation in the superconductor, this energy may be extracted by reversing the electric field. Energy may also be stored in the magnetic field inside the superconductor. The cumulative effect is that a superconductor has a complex surface impedance due to the reactive energy flow between the electrons in the superconductor and the electromagnetic field [6–8]. The surface impedance can be expressed as in equation 1.2 [9]:

$$Z_s = R_s + i\omega L_k \tag{1.2}$$

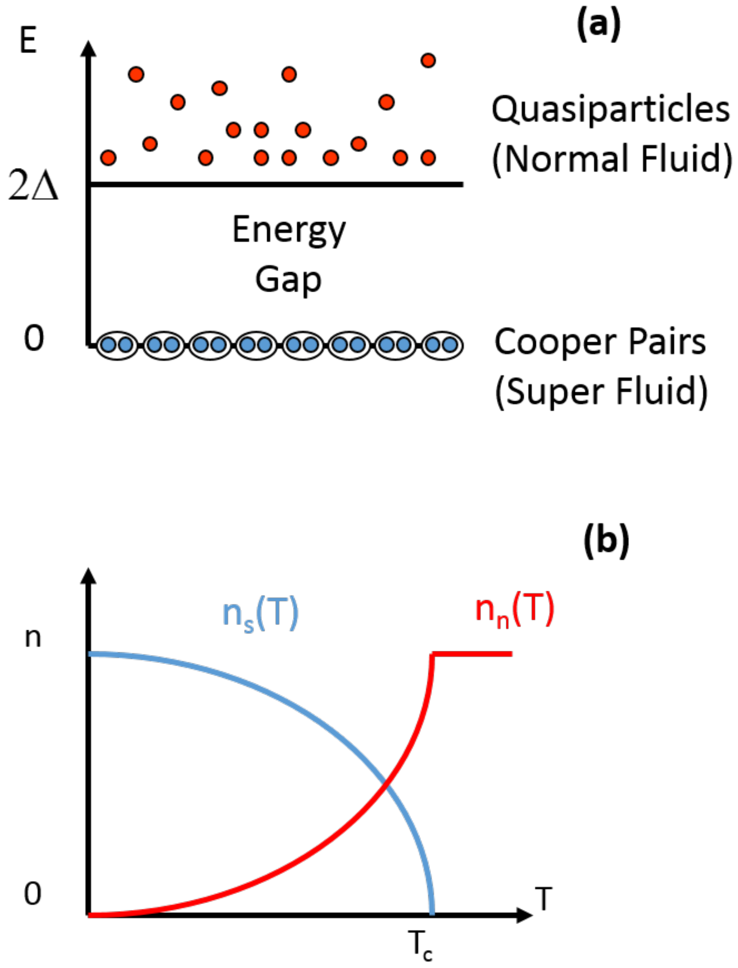

Figure 1.2: (a) The gap energy relationship for quasi-particles and Cooper pairs. (b) Quasi-particle and Cooper pair density relationship. Adapted from [10].

where the surface impedance (Z_s) includes a surface resistance (R_s) term, which describes losses at an angular frequency (ω) caused by the small fraction of electrons that are not in Cooper pairs, i.e. quasi-particles. L_k is a kinetic inductance, which originates from energy stored in the movement of the Cooper pairs. The gap energy relationship between quasi-particles and Cooper pairs is shown in Figure 1.2 (a). The density of these two types of particles in the superconductor depend on temperature and the relationship is shown in Figure 1.2 (b), where $n_n(T)$ is the density of un-paired (normal) electrons and $n_s(T)$ is the density of paired (superconducting) electrons.

1.2.2 Coherence length and London penetration depth

Coherence length (ξ) is related the size or extent of the Cooper pairs. There are two main theories to explain this phenomenon: Ginzburg-Landau (GL) and Bardeen Cooper Schrieffer (BCS). In addition, different superconductor films, based on their deposition conditions and fabrication methods may have different coherence lengths due to the quality of the superconducting material. In our work, we primarily used Nb, whose quality is related to the deposition conditions and surface properties of the substrate. In the next section, we will discuss what room temperature parameters are of interest that quantify the quality of the Nb. An important parameter that reflects the quality of any superconducting film is the London penetration depth (λ_L), which is similar to the skin depth of normal conductors and characterizes the depth a magnetic field penetrates into the superconductor [11–13].

The relationship between coherence length and London penetration depth of both types of superconductors (Type I and Type II) is shown in Figure 1.3. For example, a Nb film thickness less than the coherence length can cause superconductivity suppression [14] (metal film does not shown zero dc resistance, no Cooper pair formation, etc.). If the Nb film is thicker than the London penetration depth, then the film can carry more current, but the critical current density will be maintained approximately the same. Nb is a type-II superconductor, and therefore the coherence length is generally less than the London penetration depth. Our Nb film thickness is consistent $\sim$ 250 nm, which is equal to the estimated value of Nb coherence length at 4.2 K. The calculation detail is based on the dirty limitation equation [15]:

$$\xi_{GL} = 0.85(\xi_o l)^{1/2}(1 - \frac{T}{T_c}) \tag{1.3}$$

where ξ_0 is the coherence length at 0 K. For ideal Nb film, ξ_0 = 39 nm. l is electron mean free path. In this calculation, we use $l = 0.078$ cm, which is based on relationship $\rho l = 3.7 \times 10^{-6}$ Ωcm^2 [15]. ρ is the measurement resistivity of our Nb film right before transition temperature. For rough estimation, our penetration depth is approximately 255

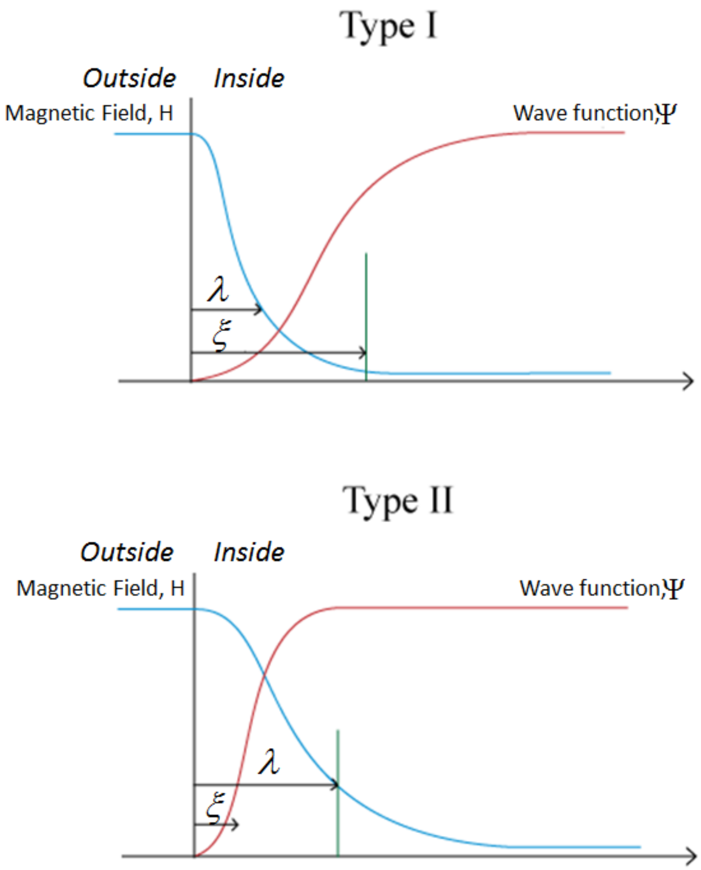

Figure 1.3: Relationship between coherence length and London penetration depth for type-I and type-II superconductors. Adapted from [24].

nm based on the radio of $\xi_0/\lambda_L = 1.02$ [16]. Therefore, we choose our Nb film thickness to be between the coherence length and London penetration depth. The reader is directed to excellent references including [17–23] for details on the theory of LTS.

1.2.3 Superconducting proximity effect

In the present work, we have also studied structures comprised of stalks of superconductor material plus normal conductor material. In structures such as this the materials can be affected by the superconducting proximity effect. The superconducting proximity effect describes the behavior when a superconductor has an electrical contact with a normal metal or another superconductor. This bilayer structure can realize superconductivity, but may

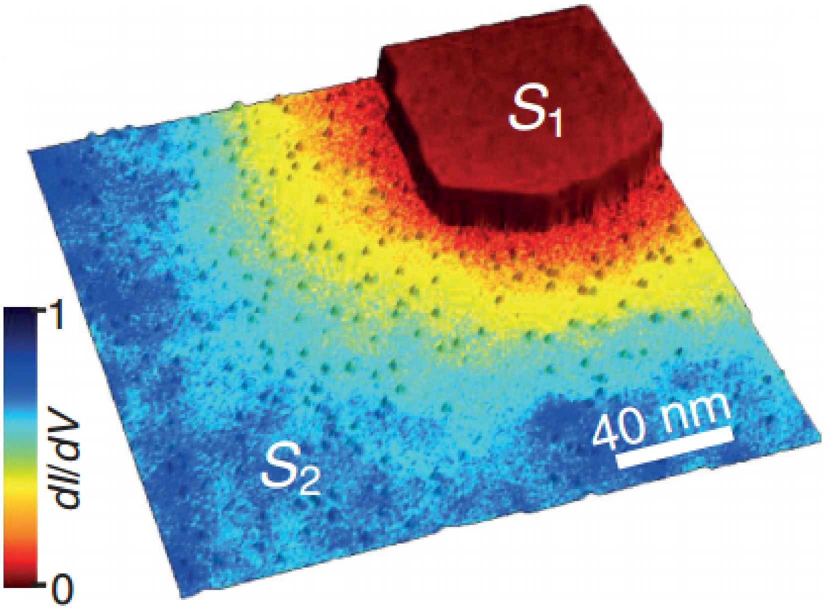

Figure 1.4: Topographic STM image of the sample showing proximity effect at 0.3 K for two superconductors. The spectroscopy map allows visualization of the proximity effect. Adapted from [29].

show a certain level of suppression in the T_c. When the bilayer is below transition temperatures, Cooper pairs will leak into the normal metal (or another superconductor) region as shown in the Figure 1.4. This can be explained by Cooper pairs having a coherence length that is macroscopic in distance, even after penetrating into the normal metal [25]. Another perspective is that the wave function of the superconducting state of one superconductor penetrates into the other superconductor or normal conductor, thereby proximity electrons into the superconducting state. This impacts electrons in the normal metal layer, by also inducing pairing, but with a coherence length that is different from the coherence length in the superconductor layer. The penetration distance is limited by the interface contact, quality of superconductor, normal metal type, etc. There is a significant amount of on-going research in this area from both the experimental and theoretical sides [26–28].

1.3 Flexible dielectric materials

There are a lot of ways to reduce the thermal load in a cryogenic measurement system. Shrinking the cross-section area of the cables were used in these systems was considered one of the best solutions. There are significant efforts have been taken into this area by replacing the coaxial cables to thin polymer-based flexible cables. But most of the researchers focus on building superconducting dc flexible cable or Cu RF and dc cable on these types of thin flexible dielectric material [30–32]. Our work focuses on making superconducting RF cable on these types of dielectric materials such as free-standing Kapton film and spin-on polyimide.

1.3.1 Free-standing Kapton film

Kapton polyimide is a commonly used flexible substrate material that provides several benefits compared to other flexible materials, such as a low cost, range of available thicknesses and good mechanical stress tolerance [33, 34]. Based on its low thermal conductivity, Kapton has been widely used for thermal isolation in cryogenic systems [35, 36]. Though it is an often used material in low temperature systems, there are limited reports on the microwave properties of these materials at deep cryogenic temperatures. A. Harris, et al., have reported Kapton loss information at 77 K [37] and several other groups have reported loss information at 4.2 K, but only at low frequencies (∼1 MHz) due to limitations in their measurement methods [38–40]. Furthermore, there are few reports of superconducting microwave structures on commercially available Kapton, presumably due to fabrication challenges related to defects present on the Kapton surface [41].

1.3.2 Spin-on polyimide

Spin-on polyimide is another commonly used dielectric for microelectronics packaging and integration structures. For cryogenic interconnects that deliver microwave signals, we desire low loss dielectric materials to eventually fabricate transmission lines that can interface to different types of microwave devices, especially superconducting devices, which are extremely sensitive to environmental noise and thermal fluctuations. Therefore, our intentions were to minimize losses in the substrate by selectively choosing dielectrics that are low-loss and mechanically compliant when used as free-standing microwave flex cables. Polyimide based materials have been widely used as cryogenic thermal isolation layers and packaging materials since they have very low thermal conductivity [42, 43]. To be a useful microwave flexible substrate material, a relatively low loss at microwave frequencies is an important characteristic. Therefore, several groups have characterized the loss information of different types of polyimide at cryogenic temperatures to determine its applicability in cryogenic electronics, though, the majority of the characterization was focused on the low frequency region ($\leq$ MHz) [38–40].

1.3.3 Potential alternative dielectric materials

LCP (liquid crystalline polymers) are commonly used as a substrate material with low loss over a very wide frequency range [44]. Therefore, LCP has been widely used as a flexible microwave substrate for transmission lines, antennas [45–49], packaging material, as well as interconnect material [50–54]. Similar to free standing Kapton, LCP can be found in various thicknesses. There are also several groups who have studied the thermal performance of this material [55–57]. Given that LCP has shown to be a suitable substrate material at room temperature, it would be worth noting that its cryogenic microwave properties have not yet been studied using superconducting metals. We did not investigate LCP for cryogenic flex cables, though this is an area of future research that could be undertaken to characterize this material at low temperatures and the structures and techniques described in this dissertation should be applicable to such an effort.

1.4 Low temperature superconducting materials

Nb is one of the most common low-temperature superconductors studied. Nb has an ideal, bulk T_c of 9.3 K, which is > 4.2 K and one of the highest of any elemental superconductor. Moreover, Nb can be easily deposited through a sputtering process, and it is not difficult to achieve reasonable thicknesses without impacting the superconductivity. We have been able to deposit controllable quality Nb film in our lab sputtering chamber. We have noticed the Nb film quality is sensitive to the chamber conditions such as oxygen level in the chamber, sputtering pressure, and Nb target changes. We judge the Nb film quality by measuring the room temperature sheet resistance of Nb films on a witness die with an SiO_2 surface. M. D. Henry, et al., showed there is a relationship between a superconductor's normal room temperature (RT) sheet resistance and superconducting critical transition temperature, which is shown in Figure 1.5 [58]. Therefore, as the sheet resistance at RT decreases, the Nb T_c shows an improvement, which moves closer to the bulk T_c. Based on this relationship, we track the sheet resistance of the Nb film to note any increases or decreases in the sheet resistance and we proceed with further sample characterization if the Nb quality is deemed sufficient.

Due to a higher transition temperature than Nb, we briefly studied niobium nitride (NbN), which is a good low-temperature superconductor material candidate. Similar to Nb, the sputtering parameters must be carefully chosen to obtain high-quality films and the gas composition (ratio of N_2 and Ar) must be carefully chosen to yield high quality NbN films.

M. Lucci, et al., studied NbN growth on different types of substrates [59]. They found the deposition of NbN on different substrates impacted transition temperature and transition width (slope from normal resistance to zero dc resistance), which the authors noted was related to the crystalline (single, poly, or amorphous) nature of the underlying substrate. The exhibited transition temperature trend for the different substrates is shown in Figure 1.6. For flexible substrates, such as Mylar and Kapton (lack of crystallinity), the T_c was

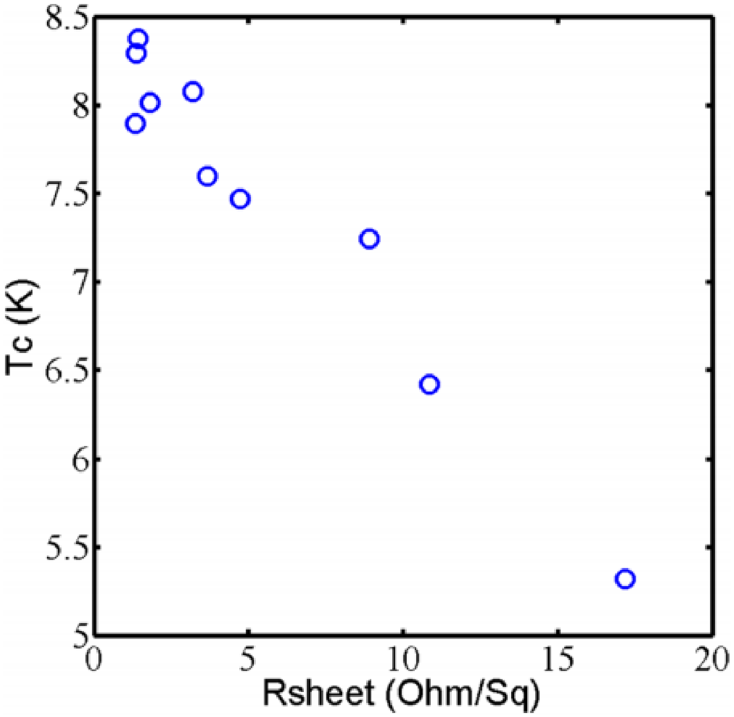

Figure 1.5: Nb film critical temperature as a function of sheet resistance. Adapted from [58].

lower and the transition width was larger with respect to crystalline substrates, such as magnesium oxide (MgO).

Other commonly studied low temperature superconductors include MgB_2 and Al. Al is a good material due to its robust oxide and reasonable transition temperature of 1.2 K, though it is below our desired $T_c > 4.2$ K. Researchers commonly use Al resonators patterned on sapphire substrates because it provides a stable radio frequency (RF) performance and can be easily wire bonded. Moreover, researchers in high-profile research groups have been able to build resonators with extremely high quality factors (Q) above one million and can therefore be used for quantum bit applications [60, 61].

1.5 Overview of superconducting flexible cables

Thermal loading and heat leakage from a higher temperature to a lower (colder) temperature stage is a concern for cryogenic experiments performed in the mK range. Recently,

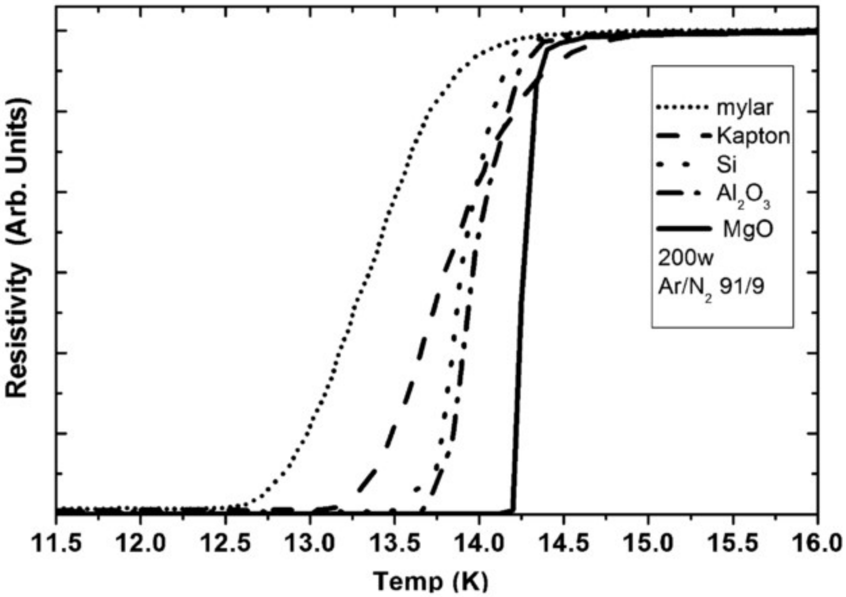

Figure 1.6: Resistivity vs. temperature plot of NbN film on various substrates. Adapted from [59].

there has been significant interest in the development of quantum computing using superconducting qubits, which has lead to a desire for advancements in technology for cryogenic systems. One source of thermal loading is the measurement cables, both dc and RF coaxial cables. The RF cables are generally attenuated at different temperature stages to reduce thermal noise. Therefore researchers use materials that are poor thermal conductors, such as stainless steel, but this type of cryogenic coax cable has high conductor resistance[1], which results in additional attenuation at high frequencies. Another type of cryogenic coax cable uses superconductors to limit thermal leakage, which leads to more efficient use of the cryogenic system[2]. Furthermore, using superconductor metals to replace the normal metals reduces the microwave conductor losses of the cables. Generally, though, the more cables that are loaded into the cryogenic system, the longer the cool down time for the system. One approach to solve this problem is to reduce the cross sectional area of the cables, thereby reducing the thermal load on the cooling system.

---

[1] `http://www.lakeshore.com/products/cryogenic-accessories/cable/pages/overview.aspx`

[2] `http://www.keycom.co.jp/eproducts/upj/upj6/page.htm`

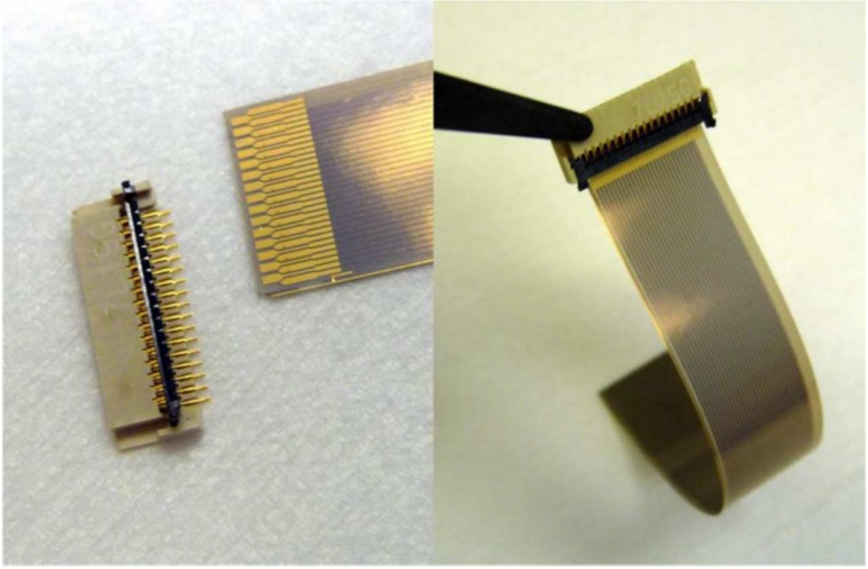

Figure 1.7: Direct current (dc) flexible cable on YSZ tape. Adapted from [30].

There are several research groups working on the development of superconducting flexible dc cables such as C. S. Yung, et al. [30], M. Y. Cheng, et al. [31] and T. Tighe, et at. [32]. C. S. Yung, et al., successfully built a flexible flat cable with 33 traces on 200 μm wide, 300 nm thick MgB_2 deposited on a flexible yttria-stabilized zirconia (YSZ) substrate and compatible with commercially available dc connectors, as shown in Figure 1.7 [30].

Most of the deep cryogenic computing use microwave connections to interface to low-loss substrates. Therefore, there is a need for efficient (high speed) and low cross-talk, flexible RF cables to replace traditional coax connections. This would allow researchers more connections in a single cable to interface to multiple RF connections. A. Harris, et al., designed and built a 10 cm long, 7 parallel microstrip transmission line cable on DuPont Pyralux AP-8555R stock substrate as shown in Figure 1.8. The substrate was 5 mil thick and had standard copper cladding of 0.5 oz. (17 μm thick) [37]. Based on the dielectric thickness, they designed the signal traces to be 11 mil wide, which allowed this group to solder directly to the flex cable using standard edge launch SMA connectors.

A. Harris, et al., measured loss and cross-talk for arrays of microstrip lines in flex circuit technology at 297 K and 77 K, which showed good RF performances up to 20 GHz. They also built resonators to characterize the Kapton substrate from 297 to 77 K. The result shows the dielectric constant (ϵ_r) of Kapton changes very little in this temperature range. Meanwhile, the loss of the substrate dropped by a factor of approximately two, from tanδ = 0.013 to 0.007. In order to reduce the thermal loading, they also patterned the ground plane under the signal lines, which reduces the heat flow by a factor of three, compared to a solid ground plane, which reduced cross-talk at the expense of higher thermal conductivity. The microwave performance of this flexible cable is shown in Figure 1.9. In order to relate the impact of the dielectric loss tangent to insertion loss (S_{21}) measurements, we simulated the same length microstrip transmission line (without the edge launch structure) on Kapton substrate with various loss tangent values as shown in Figure 1.10. We can clearly see the dielectric loss tangent can dominate the insertion loss, even when there is no conductor loss. Therefore, it is critical to measure the dielectric loss tangent of the underlying substrate to quantify the loss solely due to the substrate. They proposed future work to include reducing the thickness of the substrate, but mentioned that the fabrication and measurement would be a challenge (this would change the trace width) [37].

Thin-film cables fabricated at a wafer level using convectional photolithgraphy, present an excellent opportunity to significantly reduce the cross-sectional area of multi-conductor superconducting flexible cables. The use of normal conductors would result in excessive losses since the dimensions are small (i.e., thickness ~250 nm and width ~50 μm). Therefore, we explored the use of superconductors, which allow very small conductor traces with insignificant loss over a wide frequency range (up to 20 GHz).

1.6 Characterization of dielectric materials using resonators

There are several methods that can be used to obtain the microwave properties of a dielectric material. One of the dielectric characterization techniques is based on using microstrip transmission line resonators. There are many types of transmission line resonators based on microstrip, stripline, CPW, etc. These include both ring and line resonators. We

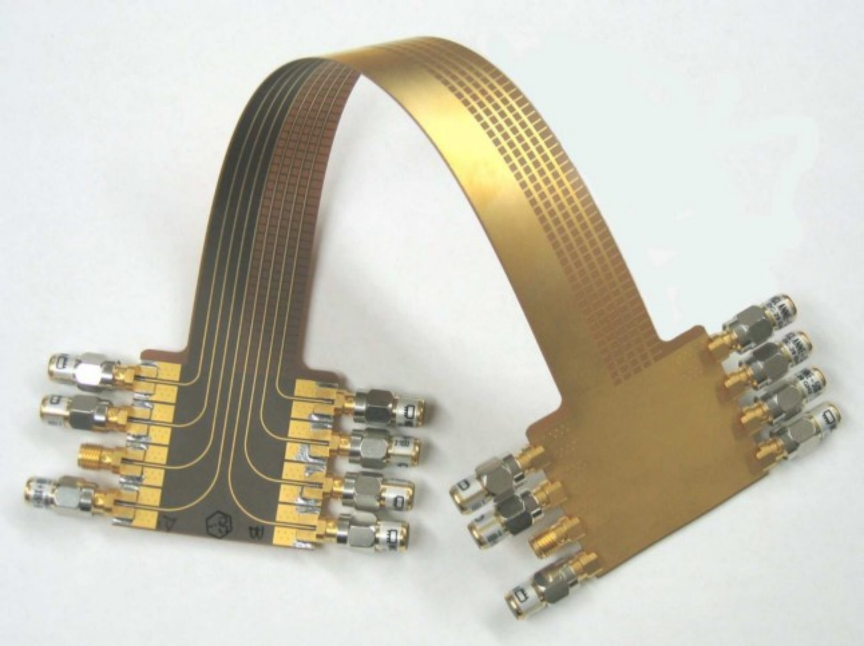

Figure 1.8: Cu microstrip flexible cable on free-standing Kapton. Adapted from [37].

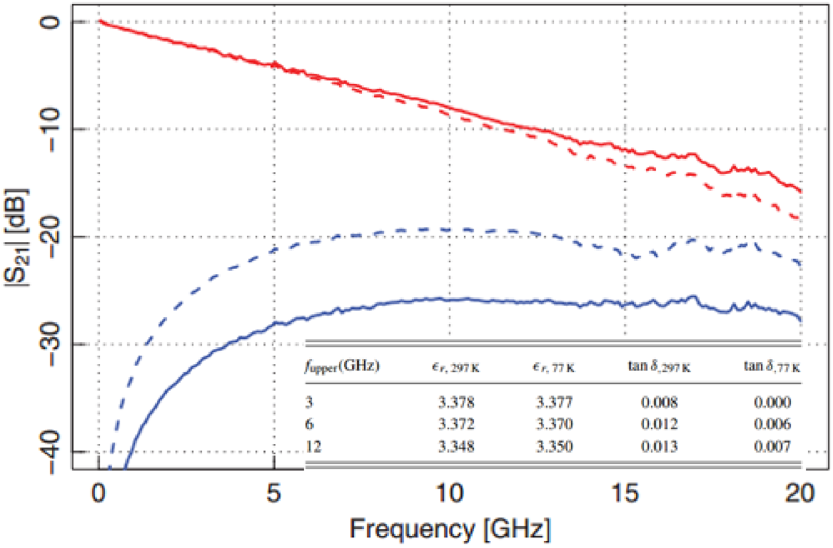

f_{upper}(GHz)	$\epsilon_{r,\,297\,\text{K}}$	$\epsilon_{r,\,77\,\text{K}}$	$\tan\delta_{,297\,\text{K}}$	$\tan\delta_{,77\,\text{K}}$
3	3.378	3.377	0.008	0.000
6	3.372	3.370	0.012	0.006
12	3.348	3.350	0.013	0.007

Figure 1.9: 27 cm long Cu microstrip flexible cable (Kapton) RF performance at room temperature (297 K). Inset table is the summary of the dielectric constant and loss tangent measurement at 297 K and 77 K. Adapted from [37].

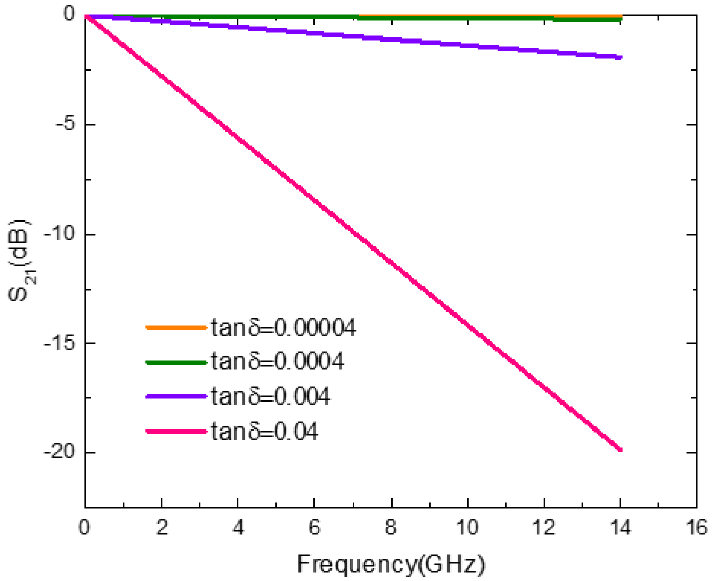

Figure 1.10: Agilent Advance Design System (ADS) simulation result of a 27 cm long microstrip with varying loss tangent on a Kapton substrate. The metal layer is perfect conductor in this simulation, to observe the losses due to the dielectric.

will introduce ring resonator first. A ring resonator configuration is shown in Figure 1.11, which included a ring loop in series with two small capacitors on each end. This type of resonator has negligible radiation losses but also has disadvantages including: (a) effects of curvature, (b) local radiation distortion of the electric field in the vicinity of the coupling gaps, (c) possible field interactions across the ring, (d) possibility of resonant splitting due to non-uniformities around the line width of the ring. If the ring radius is large enough (generally the width of the ring divided by the radius of the ring resonator is smaller than 0.2), one can minimize the problems listed as a-c [62]. The design detail and layout will be explained in chapter 3.1.

Straight transmission line resonators can be made in two forms: a half-wavelength transmission line in series with small coupling capacitors on each end, as shown in Figure 1.12, or a quarter-wavelength resonator coupled in shunt directly to the feeding line, as shown in Figure 1.13.

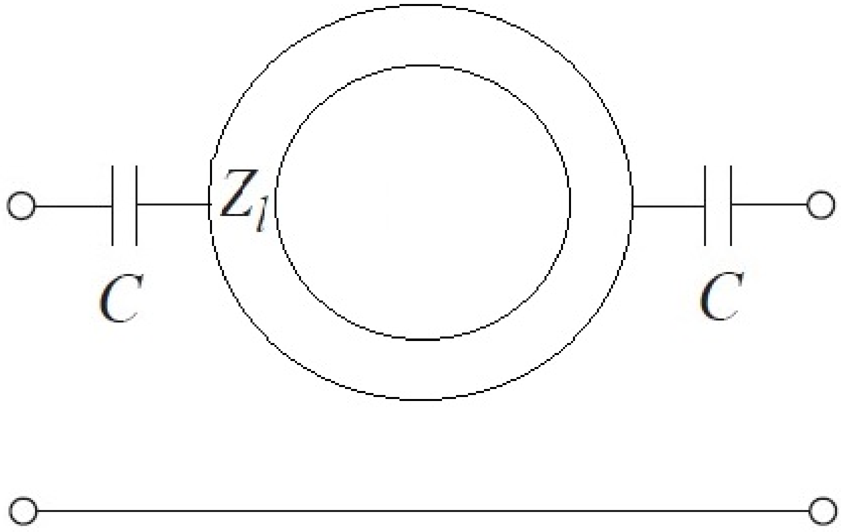

Figure 1.11: A ring resonator with series capacitors for input and output coupling. The characteristic impedance of the line is Z_l.

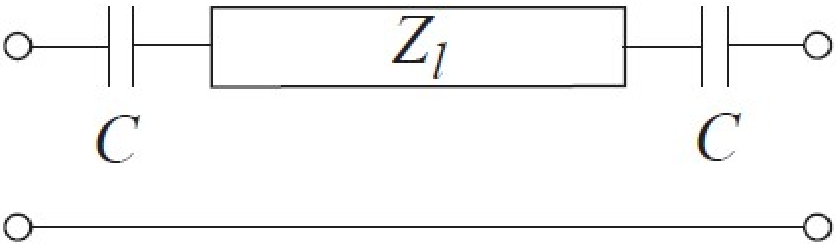

Figure 1.12: A half-wavelength transmission line resonator with series capacitors for input and output coupling. The characteristic impedance of the line is Z_l. Adapted from [63].

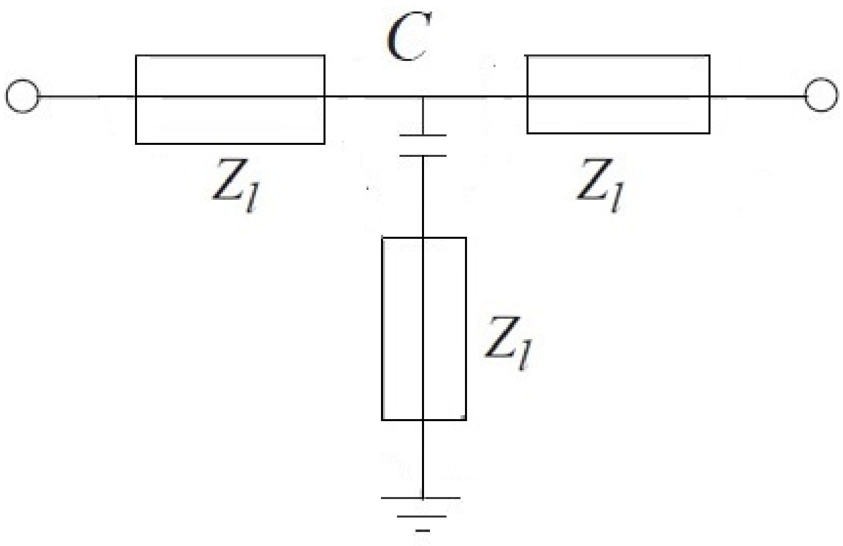

Figure 1.13: A ring resonator with series capacitors for input and output coupling. The characteristic impedance of the line is Z_l.

Similarly to microstrip transmission line resonators, CPW resonators can also be designed to be either half-wavelength or quarter wavelength resonators. The impedance of CPW resonators can be controlled by different lateral size scales from millimeters down to micrometers. CPW quarter wavelength resonators are the common method in cryogenic applications. Most of the superconductor resonators recently reported are coplanar waveguide (CPW) resonators. This is due to the ease of incorporating into an interface circuitry and typically only require one metallization layer. Another reason this type of resonator is popular is due to the rapid development of quantum qubit devices, where the resonator works as an information transfer bus. These types of resonators have also been used in sensitive detectors known as microwave kinetic inductance detectors (MKID).

1.6.1 Principles of characterizing dielectrics using resonators

If we choose to use a resonator to characterize the dielectric, we need to design the resonator to be under coupled to the feed lines. The under coupled design produces negligible shifting of the resonant frequency and provides a high sensitivity to the properties of the dielectric material. In order to meet this requirement, the geometry of the coupling gap has to be optimized. If the coupling gap is too large, the attenuation of the coupling gap may be too high. This will lead to insufficient signal for exciting some of the higher order resonances of the ring resonator. In our work, we used an EM simulation tool (i.e. HFSS) to sweep the size of the gap to verify the resonant frequency does not show an obvious shift.

Loss tangent characterization can be carried out more accurately with lower coupling levels since one would like to minimize coupling losses. In addition, if the coupling level is too weak the resonant mode may be buried below the noise level on a network analyzer. Therefore we designed our resonators to have the 1st resonant mode above -30 dB, which is ∼20 dB higher than the noise floor and found that this is a good level to observe the resonance peaks. The quality factor of a resonant peak is 2π times the ratio of the total energy stored divided by the energy lost in a single cycle, or equivalently the ratio of the stored energy to the energy dissipated over one radian of oscillation. In general, we obtained the quality factor by using the -3 dB technique, where the quality factor is defined as the resonant frequency divided by the 3 dB bandwidth, where the output power has dropped to half of its value, as shown in equation 1.4:

$$Q_{load} = \frac{f_0}{BW_{-3dB}} \tag{1.4}$$

where Q_{load} is the loaded Q. Usually we can obtain Q value directly from our measurement system or data. In this dissertation, the Q factor in all the plots is the loaded Q, unless noted differently. In order to extract the loss tangent (tanδ) of the dielectric, we need to extract the unloaded quality factor. A relationship between the loaded and unloaded quality factor (Q_{unload}) can be given as in equation 1.5:

$$\frac{1}{Q_{load}} = \frac{1}{Q_{unload}} + \frac{1}{Q_{extra}} + \cdots \tag{1.5}$$

where Q_{unload} is the unloaded quality factor and Q_{extra} is an “all-inclusive” extra quality factor, which mainly includes the loss related to coupling. In this work, we extract the coupling quality value by using Agilent Advance Design System (ADS) simulator. There are also other factors that cause losses in the loaded quality factor, such as the measurement system losses. In these measurements, the sources of the external loading are the feed lines, connector interfaces, measurement cables, and the network analyzer. For negligible coupling levels, the measured quality factor of the resonator Q_{load} is approximately equal to the unloaded quality factor Q_{unload}.

There are different ways allowed us calculate unloaded quality factors. One of the common way to calculate Q_{unload} of symmetrical resonators is based on equation 1.6:

$$Q_{unload} = \frac{f_0}{1 - 10^{-L/20}} \tag{1.6}$$

where L is the insertion loss at the peak of the resonant frequency. By using this equation, we can calculate the unloaded quality factor accurately. This calculation requires an accurate insertion loss measurement, which requires that an accurate calibration process be performed before the resonator measurement. This can be a challenging situation and requiring significant effort. For normal conductor metallization, especially for room temperature measurement, the measured quality factor (Q_{load} or Q) is not sufficiently high, compared to the other quality factors, it is preferred to use this method to calculate the unloaded quality factor. Moreover, with a good calibration, obtaining accurate insertion loss measurements, one can accurately determine of the unloaded Q.

For superconducting resonators, high quality factors (Q_{load} or Q) will be observed because the conductor loss has been minimized, compared to normal metallization. We can use a different method to extract the unloaded Q factor of these superconducting resonators. For microstrip resonators, the Q_{unload} relationship is provided in equation 1.7:

$$\frac{1}{Q_{unload}} = \frac{1}{Q_c} + \frac{1}{Q_d} + \frac{1}{Q_r} + \cdots \tag{1.7}$$

where Q_c is associated with conductor loss, Q_d is associated with dielectric loss and Q_r is associated with radiation loss [64]. For superconducting resonators, specifically when T $\ll T_c$, the conductor loss is negligible. So the corresponding Q_c is large and this term in equation 1.7 can be neglected. For a straight (non-ring) microstrip resonator, we have more radiation loss than the closed loop microstrip ring resonator, since it has open ends. In general, though, this loss is smaller than that from the dielectric itself, and therefore it can be safely ignored. With these modifications, $Q_{unload} \sim Q_d$. We can then extract the dielectric loss tangent value according to [64]:

$$Q_d = \frac{1}{tan\delta}(1 + \frac{1-q}{q\epsilon_r}) \tag{1.8}$$

where, Q_d is associated with dielectric loss, tanδ is the dielectric loss tangent, q is the dielectric filling factor and ϵ_r is the dielectric constant of the dielectric. This filling factor is related to the dielectric constant and also the design geometry. Equation 1.8 allows us to extract the dielectric loss information (loss tangent, tanδ) of the substrate material. At low temperatures and frequencies below a few 100 GHz, intrinsic dissipation in superconducting devices is dominated by losses from dielectric materials, therefore to characterize the loss tangent of the dielectric is a very important first step in the process of making superconducting microwave cables with low microwave losses.

1.6.2 Superconducting resonator design and measurements Considerations

Unlike normal metal resonators that typically have low quality factors below 100, superconductor resonators have such high quality factors that one needs to make sure to take sufficient number of data points at the resonant frequency range to obtain an accurate quality factor. If we only do a broad band frequency sweep, the resonant peaks can easily be missed. Though, as shown in Figure 1.14, with sufficient points, the peaks can be found. An ADS simulation result of a perfect conductor microstrip resonator is shown in Figure 1.14. The broad band sweep results are shown in Figure 1.14 (a), we can see the insertion loss value (S_{21}) of the fundamental harmonic is ~-30 dB. When we narrow the frequency range and take finer simulation steps (100 Hz), the S_{21} value of the fundamental harmonic shows approximately 0 dB. This is critical for determining the -3 dB points for calculating the Q. In our measurements, we have to reduce the frequency span to an acceptable range and increase the number of points to capture the true S_{21} values. Therefore, we decrease our frequency range to capture the peak S_{21} of the resonance and increase the number of data points to 1001, in order to have a sufficiently rapid response from the network analyzer and avoid any unwanted transients due to temperature fluctuations in the cryogenic system.

A suitable cryogenic microwave measurement package is very important for obtaining reliable and consistent measurement results. Unlike room temperature measurement setups where probes can be used or fixtures can be adjusted as necessary without too many complications, at cryogenic temperatures, where it may take hours (or days) to cool-down, a reliable packaging setup is very important. At cryogenic temperatures, we require a reliable connection between our device and connectors, this implies reliable materials that can be repeatedly thermal cycled with a reasonable life-time. One of the most common ways to make reliable electrical connections includes wire bonding or flip chip attachment to a microwave device. A significant number of microwave cryogenic research groups have developed their own sample measurement packaging (holder). One of the sample holders is shown in Figure 1.15. Wire bonding is usually the best choice for connecting to the small microwave traces from the microwave launch structures. For most of the quantum groups, they choose Al wire bonds to connect their launch structure to compact Al or Nb resonators, as shown in Figure 1.16. In our project, there were several packaging challenges, which are inherently different from the traditional resonator measurement setups. For example, there are cryogenic probe stations that some groups use, but for our measurement temperatures of interest (4.2 K and below), cryogenic probe stations are not necessarily the most efficient system to use. Therefore using a cryogenic probe station using microwave probes (i.e. GSG probes) was not a good choice for measuring our devices. Furthermore, we were limited by the film thickness of

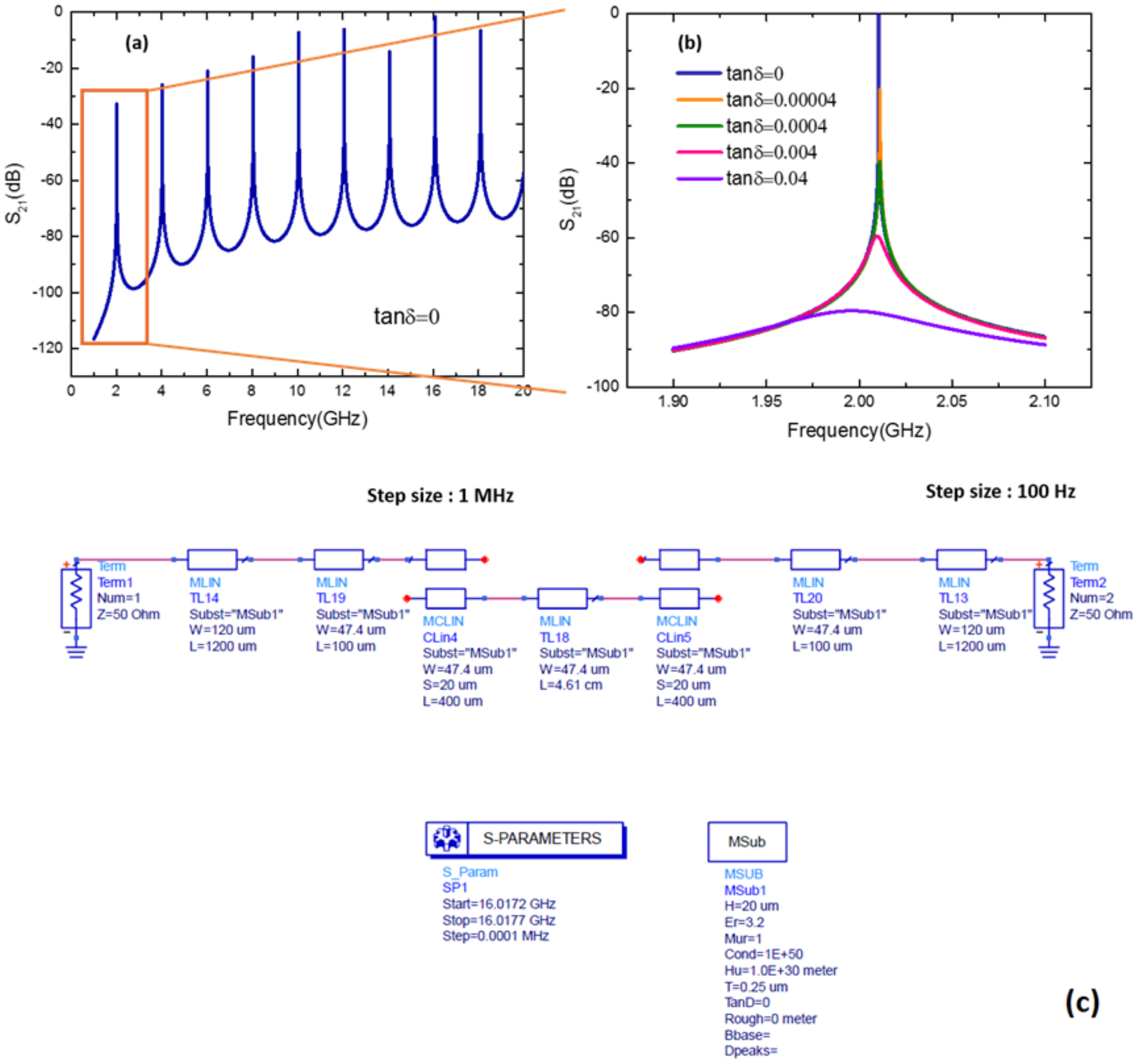

Figure 1.14: Simulation results of perfect conductor microstrip resonator. (a) A broad frequency view of a resonator with a simulation step size of 1 MHz. (b) A small frequency range simulation with various tanδ values and a step size of 100 Hz. (c) ADS simulation setup.

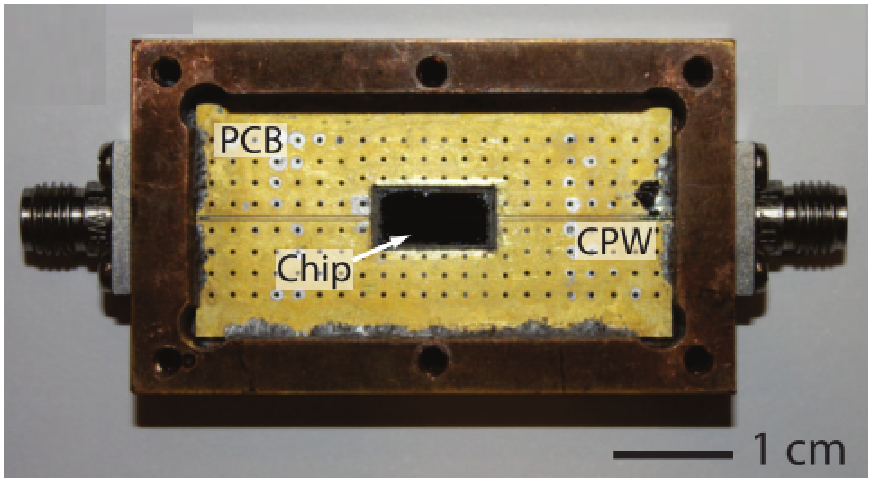

Figure 1.15: A CPW resonator assembled in a sample holder. Adapted from [65].

our devices and the trace width (for 50 Ω characteristic impedance) for structures with ~50 μm dimensions. Therefore, we interfaced to our thin-film resonators as free-standing films with edge launch connectors that had the smallest pin size that is currently commercially available (~0.005”). The details of our measurement package will be discussed in Chapters 2 and 3.

1.6.3 Other applications of superconducting microwave resonators

Superconducting microwave resonators can be used to carry microwave photons and for superconducting qubits (quantum bits), which is termed “circuit QED”. A. Wallraff, et al., [67] experimentally coupled a cavity QED with a single artificial atom and a single photon in a solid-state system using a Nb resonator as shown in Figure 1.17.

These types of resonators have also been widely used as read out systems in MKIDs [68, 69], where the detectors are sensitive enough to detect single photons. Superconductor films exhibit kinetic inductance, which increases as the film thickness is decreased. MKIDs detect photons by detecting the changes in surface impedance. Photons incident on the surface have enough energy to break Cooper pairs and generate quasi-particle excitations that change the characteristic impedance of the detector. The phase and magnitude of the signal change is read with assistance from a CPW superconductor resonator.

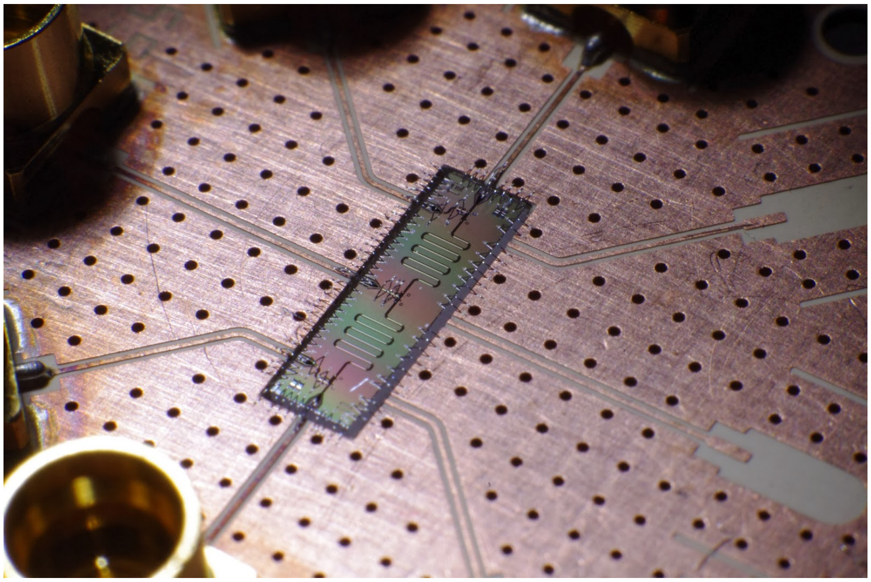

Figure 1.16: A CPW resonator connected to a CPW launch structure by Al wire bonds. Adapted from [66].

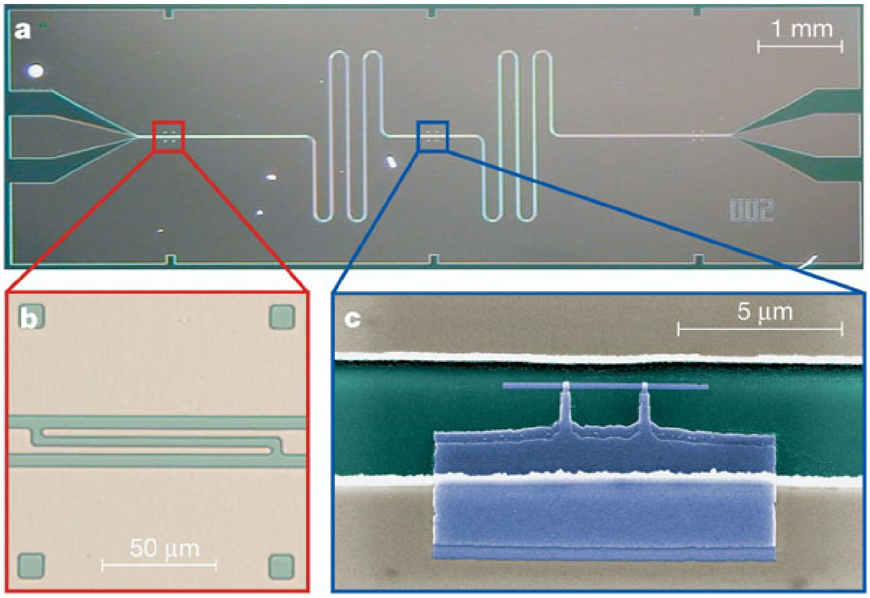

Figure 1.17: (a) Integrated circuit for cavity QED. (b) Coupled capacitor at each end of the resonator. (c) The cooper pair box. Adapted from [67].

1.7 Outline of this dissertation

The outline of this dissertation is shown below:

- In Chapter 2, we start with a discussion of the Kapton selection process. Superconducting metals such as Nb and NbN can realize superconductivity only on certain types of Kapton surface. Initially, we built test structures on different types of Kapton to determine the most suitable Kapton surface. We then go into detail about the Kapton microstrip resonator design, measurement setup, and characterization results. Lastly, we discuss our design and fabrication for a one meter long microstrip on Kapton.

- In Chapter 3, we present characterization results of spin-on dielectrics that were fabricated at the wafer-level and made into free-standing films. We investigated two different types of spin-on polyimide: PI-2611 (low stress, non-photo definable polyimide) and HD-4100 (photo-definable polyimide). We built flexible resonators directly on these dielectric films. We discuss the design, measurement setup and characterization result. Lastly, we report the loss tangent of both types of thin film polyimide at various cryogenic temperatures as well as over a the broad frequency range. Moreover, we explore the quality factor changes at different output power level of PNA. Superconducting structure usually shows sensitivity to current (power) since high current (power) can break Cooper pairs, which shows a high RF loss. We present our flexible superconducting resonators also shows sensitivity to power changes. Eventually, we studied the changes in microwave properties during various humidity exposure times.

- In Chapter 4, we present results from a study of the effects of a Ti adhesion layer beneath the Nb. We also discuss the effect of cladding Nb with Cu, which can help improve mechanical reliability and potentially improve thermalization. We report the changes in quality factor for the different metal combinations and at various temperatures. From these measurements, we quantify the surface resistance changes for different Nb/Cu structures. In the second part of this chapter, we explore embedded superconducting microstrip resonators on both types of polyimide. Our measurement results show Nb quality can degrade during the polyimide curing process, while a Al/Nb/Al stack can effectively prevent the Nb from degradation.

- In Chapter 5, we summarize the conclusions of this work. Several ideas about possible future work are also discussed in Chapter 6.

In this work, we successfully built superconducting resonators and characterized different dielectric films through the use of superconducting Nb resonators at various cryogenic temperatures and over a wide range of RF and microwave frequencies. The microwave properties of the dielectric materials provided in this work are useful for those interested in the design of flexible transmission line cables or other types of interconnects for use at cryogenic temperatures. Lastly, we successfully built embedded resonators, which shows potential to build polyimide-based, fully enclosed multi-layer microwave superconducting structures.

Chapter 2

Microwave characterization of Kapton at cryogenic temperatures

In order to reduce the thermal loading in cryogenic systems, our work seeks to replace conventional RF connections with thin film transmission line flex cables. This change introduces significant challenges, not only from the fabrication process stand point, but also from the physical connections that need to be made to these substrates. In addition to reduce the microwave loss, we require superconducting films for both the signal and ground to exhibit properties close to bulk, when deposited on non-crystalline substrates. There are several reasons we chose to start with this type of dielectric. First, Kapton is a commonly used flexible substrate, retains its isolation properties at cryogenic temperatures [33, 34]. The resistivity of Kapton itself is as low as 1E+19 m/S and becomes more isolating when the temperature is decreased further[1]. Secondly, it can be purchased in various thicknesses. The thickness of the Kapton we used in this project was $\sim$50 μm.

In this chapter, we introduce the processes that we undertaken to determine a suitable free-standing Kapton substrate for the fabrication of superconducting microstrip transmission lines. In order to obtain an impedance match to a 50 Ω microwave system, we characterized the dielectric properties (broad frequency band ϵ_r and $tan\delta$) at cryogenic temperatures in the frequency range from 1 to 10 GHz [70]. The superconductor metal we chose was Nb and NbN due to their high T_c.

2.1 Free-standing Kapton selection

We initially purchased Kapton film from the online vendor, McMaster-Carr, we referred to this Kapton film as McMaster-Carr A Kapton. On this Kapton, we patterned 5 cm long

---

[1] `http://www.dupont.com/content/dam/dupont/products-and-services/membranes-and-films/polyimde-films/documents/DEC-Kapton-summary-of-properties.pdf`

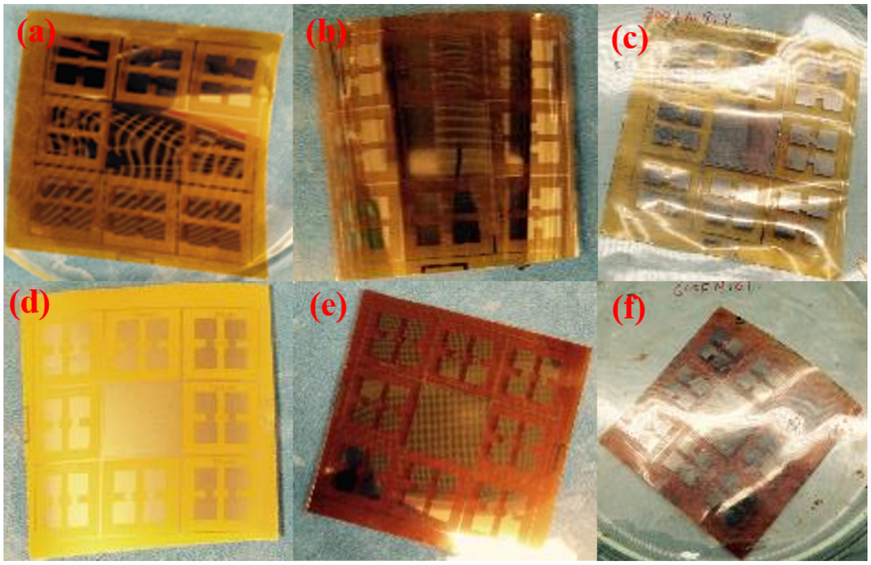

Figure 2.1: Patterned NbN lines with different line widths on various Kapton substrates. (a) DuPont 200EN, (b) DuPont 200HN, (c) DuPont 200FN919, (d) McMaster-Carr A Kapton, (e) DuPont 500HN, and (f) DuPont 500FN131.

lines with widths of 120 μm onto which we deposited NbN with a $\sim$0.25 μm thick metallizaton. Measurements that were undertaken to determine the T$_c$ of these lines indicated a partial transition ($R_{DC} \neq 0$ when T $\leq T_c$). After closer inspection, we noticed the Kapton and the metallization visually appeared rough. We therefore searched for different types of Kapton from Dupont[2] with various surface finishes. We obtained three different types of Kapton: EN, HN, and FN series, as shown in Figure 2.1. For this study, the Kapton film thickness varied from 50 μm to 125 μm.

In order to quantify the surface roughness, we performed AFM scans of the bare surface of the different Kapton films with and without $\sim$0.25 μm thick NbN metallization. The AFM results are shown in Figure 2.2 and Figure 2.3. We determined that the surface of McMaster-Carr A was approximately 10 times rougher than the 200EN Kapton with and without the metallization. For example, the average roughness of 200EN Kapton was $\sim$49 nm and after metallization the average roughness decreased to $\sim$29 nm. We therefore consider that the NbN had a good step coverage and was helped smooth out the surface.

---

[2] `http://www.dupont.com/`

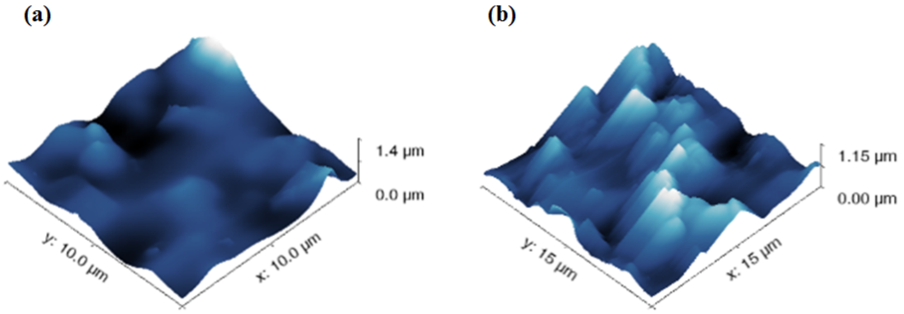

Figure 2.2: AFM image on McMaster-Carr A Kapton. (a) Bare McMaster-Carr A Kapton. (b) ∼0.25 μm NbN film on the McMaster-Carr A Kapton.

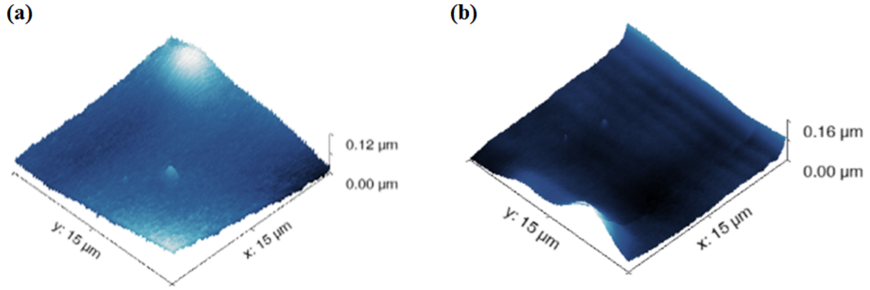

Figure 2.3: AFM image on DuPont 200EN Kapton. (a) Bare DuPont 200EN Kapton. (b) ∼0.25 μm NbN film on the Dupont 200EN Kapton.

2.1.1 NbN transition temperature comparison for different line widths and lengths on various Kapton films

This work stemmed from an interest in knowing what the T_c of our sputter deposited NbN film on different types Kapton would be. To simplify the measurement process, we used a four point pogo pin measurement set up, which is shown in Figure 2.4. The layout of the test structures is shown in Figure 2.5. This design included various line widths (50, 100, 120, and 150 μm) with a fixed length of 3.9 mm and a solid square. The purpose of the solid square was to measure the NbN film thickness and sheet resistance at room temperature.

The T_c measurement results of a 50 μm wide NbN line on McMaster-Carr A Kapton and DuPont 200EN Kapton are shown in Figures 2.6 and 2.7, which show a full transition on both McMaster-Carr A and on DuPont 200EN. Measurement results of the T_c on the McMaster-Carr A substrate were consequently inconsistent (e.g. sometimes a full-transiton was observed and other times it did not). Meanwhile, the NbN on EN Kapton always fully transitioned. We suspected that their were surface imperfections in the film that led to variable NbN properties on the McMaster-Carr A. More precisely, we suspected that the defects on these $\sim$4 mm long lines did not capture enough of an area to consistently measure the NbN film not transitioning. Consequently, there were sufficient superconducting paths in this area to short the dc measurement. We therefore, instead employed a new design that used a line with a width of 119 μm and a length of 5 cm. The T_c measurement setup for this new test structures is shown in Figure 2.8. We attached the Kapton line onto a Rogers Board[3] and soldered four wire onto four Au-coated pads on a Rogers Board, which was eventually connected to our 4 wires measurement setup in pulse tube .

The T_c measurement results of the 5 cm long lines on McMaster-Carr A and 200EN Kapton are shown in Figures 2.9 and 2.10, respectively. For McMaster-Carr A Kapton, which has a rougher surface, the line did not show a full transition. After the transition

---

[3] `http://www.rogerscorp.com/index.aspx`

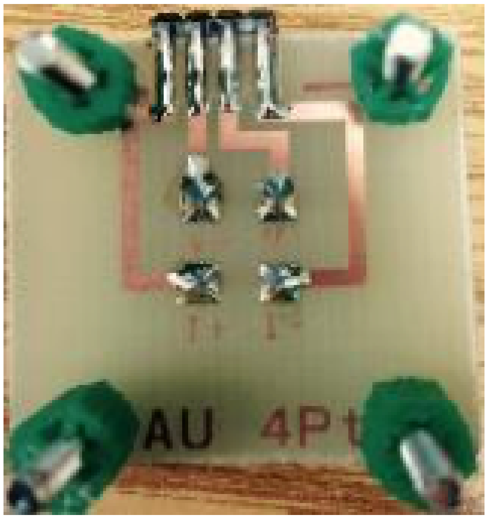

Figure 2.4: Four point pogo pin measurement setup.

temperature, the resistance stabilized at 132 Ω. We repeated the same test on 200 EN Kapton with a 5 cm long line, which consistently fully transitioned.

We also studied two other types of Kapton, HN and FN series and measured the T_c of NbN on these substrates. The NbN lines on HN series measured a residual resistance on the NbN line, which indicated a partial transition. Meanwhile, the FN Kapton fully transitioned, but had a very high sheet resistance at room temperature. Moreover, the NbN on FN Kapton had poor adhesion. Therefore, we chose DuPont EN series as the substrate material for the fabrication microwave superconducting flexible cables [71].

2.1.2 Different types of superconductors

The kinetic inductance of superconducting metallization is an important material parameter that can be calculated from room temperature measurements. For example, Nb with a bulk T_c of 9.3 K, has a lower sheet resistance (R_{sq}) than a bulk NbN film [72], which results in a lower kinetic inductance (L_k) at cryogenic temperatures. The kinetic inductance can be calculated from the room temperature sheet resistance, by using the relationship shown in equation 2.1. The kinetic inductance of a narrow line structure was calculated based on the room temperature measurement of the R_{sq} and the T_c value of the Nb and

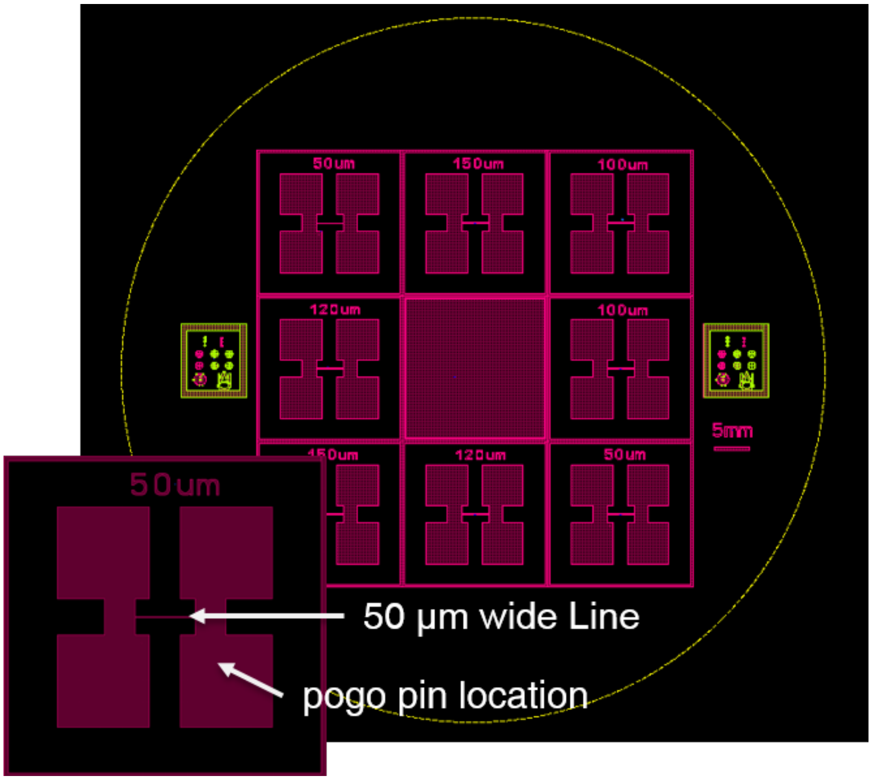

Figure 2.5: Mask layout for measuring T_c information of narrow lines on various types of free-standing Kapton.

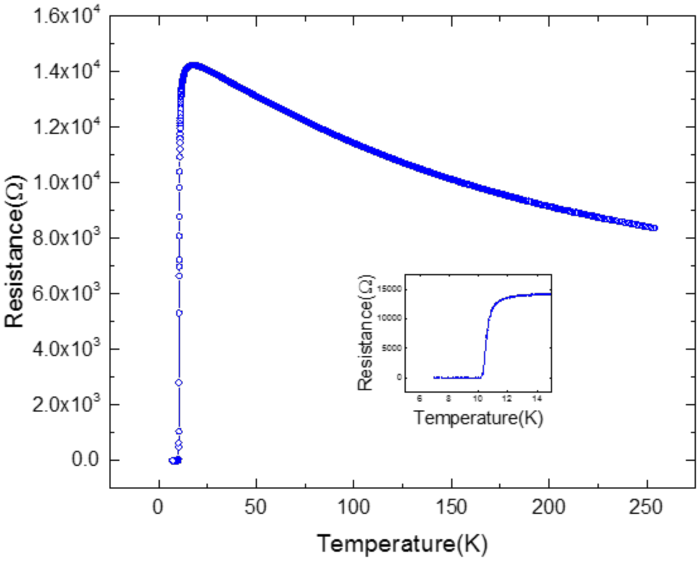

Figure 2.6: T_c measurement of NbN film on McMaster-Carr A Kapton. The width of the test line is 50 μm and the length of the line is 3.9 mm.

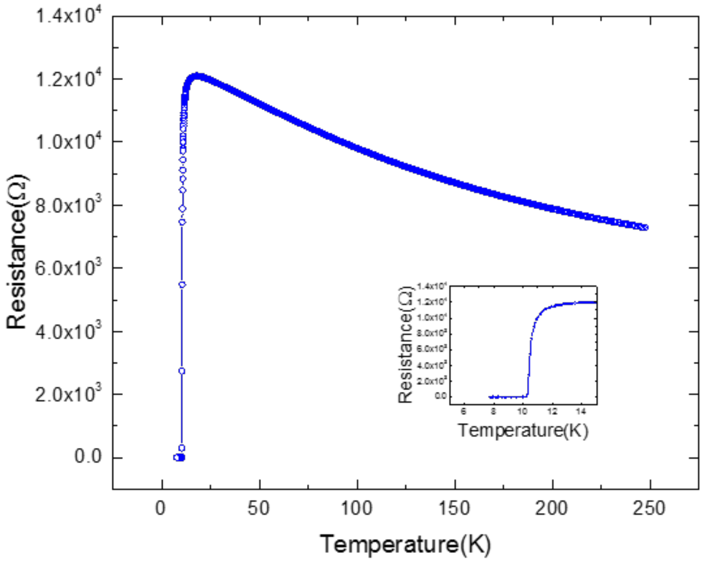

Figure 2.7: T_c measurement of NbN film on DuPont 200EN Kapton. The width of the test line is 50 μm and the length of the line is 3.9 mm.

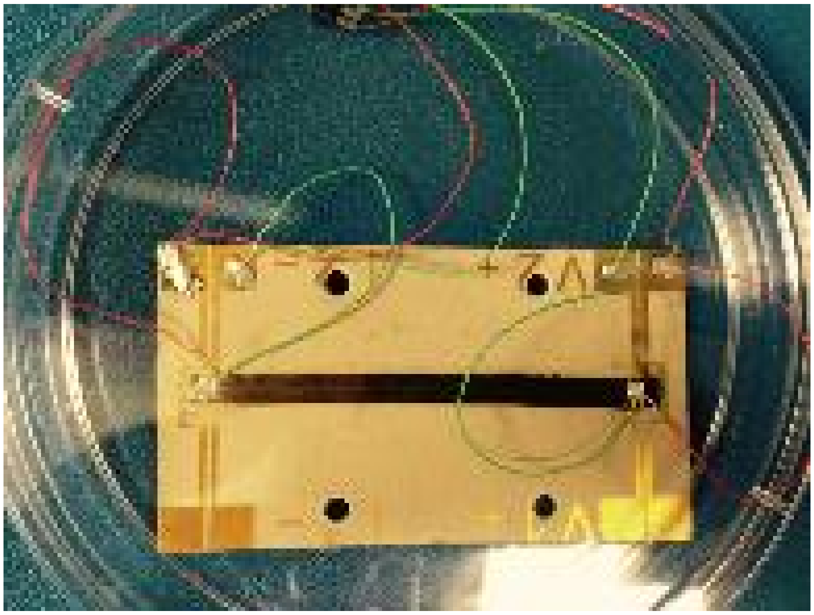

Figure 2.8: Four point T_c measurement setup of a 5 cm long line with a 119 μm wide on McMaster-carr A Kapton.

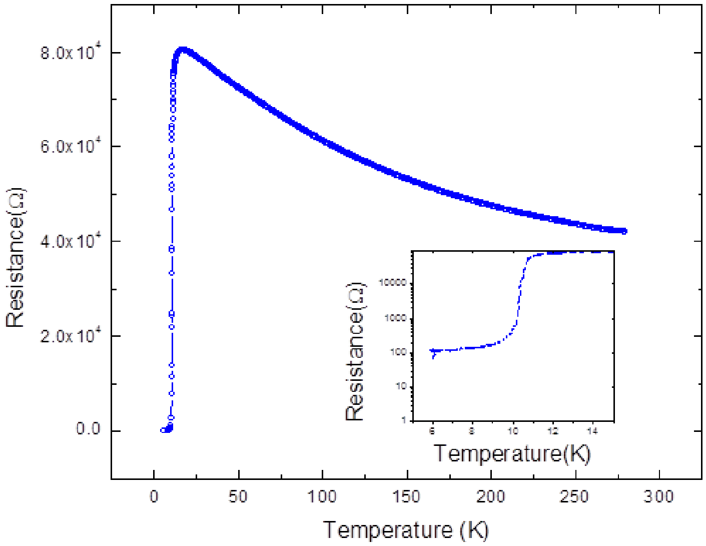

Figure 2.9: T_c measurement of NbN film on McMaster-Carr A Kapton. The width of the line is 119 μm and the length of the line is 5 cm.

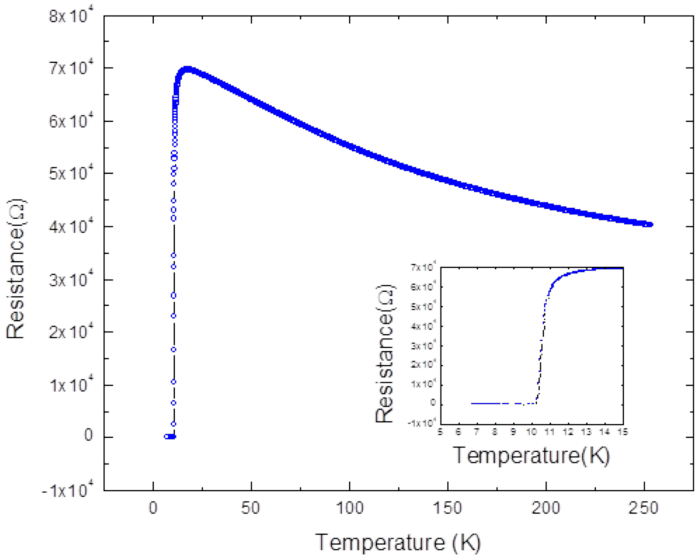

Figure 2.10: T_c measurement of NbN film on DuPont 200EN Kapton.The width of the line is 119 μm and the length of the line is 5 cm.

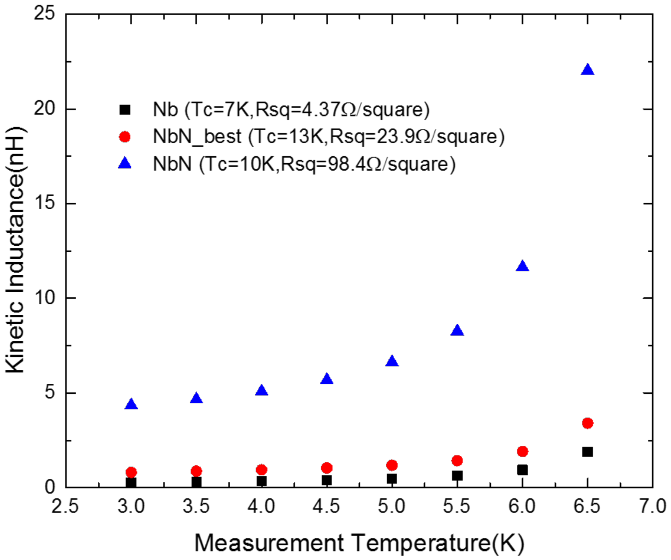

Figure 2.11: Estimated L_k of Nb and NbN films. Parameters used in this calculation are based on the Nb or NbN film deposited in our lab.

NbN film deposited in our laboratory. The calculation results are presented in Figure 2.11. The NbN film quality was sensitive to the deposition conditions, we included two types of NbN films produced in our lab, NbN_{best} was the best NbN film we have obtained and NbN represented the more general case. From the Figure 2.11, the general NbN case has the highest kinetic inductance even at temperatures as low as 3 K. For the best NbN quality deposited in our lab, the kinetic inductance is still higher than Nb. Therefore, we conclude that Nb on Kapton was a better choice for resonators than NbN.

$$L_k = (\frac{l}{w})(\frac{R_{sq}}{2\pi^2})(\frac{h}{\Delta(T)})(\frac{1}{tanh(\frac{\Delta(T)}{2k_BT})}) \tag{2.1}$$

Here l and w are the length and the width of the structure, R_{sq} is the sheet resistance at room temperature, h is the thickness of the superconducting film and the $\Delta(T) = \Delta(0)1.74\sqrt{(1-\frac{T}{T_c})}$ is the energy gap value at a given temperature. For an ideal Nb film the energy gap at 0 K is $\Delta(0) = 1.76k_BT_c$, where k_B is Boltzmann constant .

2.2 Characterization of Kapton at cryogenic temperatures using resonators

In order to obtain the microwave properties of the Kapton film at cryogenic temperatures (below 10 K). We designed a set of resonators on E-series Kapton substrates. Based on the various dielectric constant information found online, we initially based our designs on a dielectric constant of 3.6. The variation in dielectric constant is due to the different types of Kapton films available. Some of the Kapton films are sensitive to moisture and others are sensitive to temperature. These different properties of Kapton can lead to different dielectric constant values. Therefore determining the dielectric constant of E-series Kapton at liquid He temperatures and in the GHz frequency range was necessary. The microwave loss tangent was another important parameter that was necessary to extract, especially at cryogenic temperatures, where superconductor metallization can be used in which the primary losses come from the dielectric [73]. Therefore we built superconducting microstrip resonators on this dielectric film to extract the loss tangent.

2.2.1 Resonator design on Kapton

The mask layout of the transmission line resonators on $\sim$50 μm thick Kapton is shown in Figure 2.12. The design included microstrip line resonators and conductor back coplanar waveguide (CBCPW) resonators. All of the designs were symmetric half-wavelength resonators with a series capacitor at each end. The resonant frequencies were designed to be at 2 GHz, 4 GHz and so on. We chose the resonant frequencies of the half-wavelength resonator to coincide with a resonator length of $\sim$5 cm. As was introduced in the first chapter, we required weakly coupled resonators to extract accurate loss tangent information. If our coupling level was too weak, we would not be able to observe the resonant peaks because they would have been buried in the noise floor of the network analyzer, which was $\sim$-50 dB. Therefore, these resonators exhibit resonant peaks at approximately -30 dB for different loss tangent values.

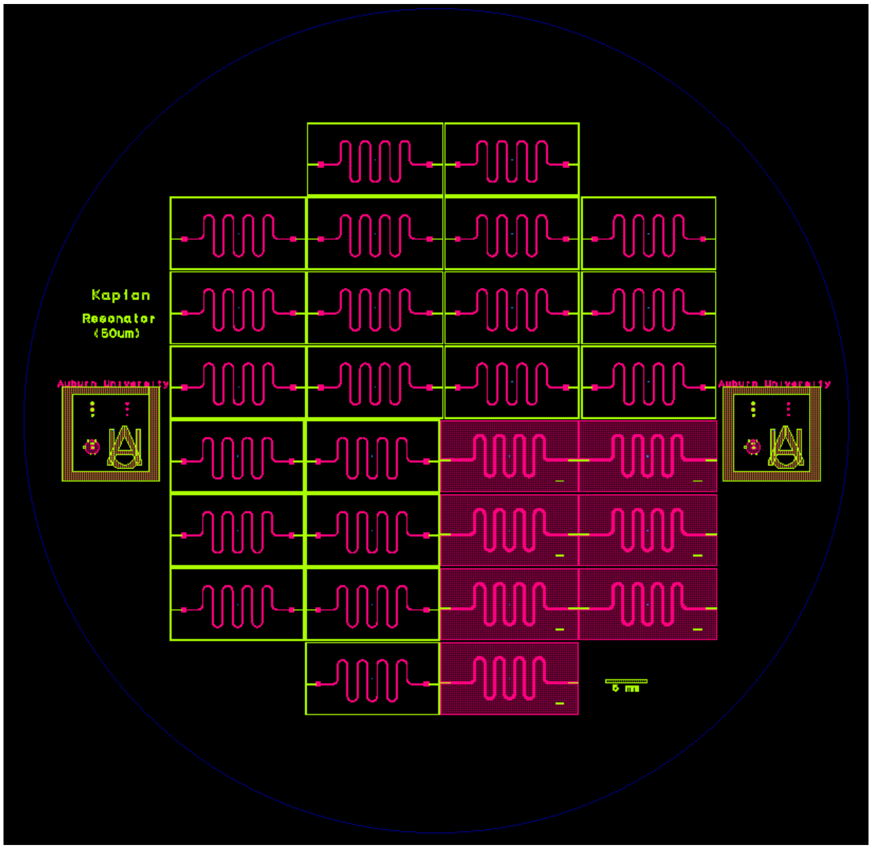

Figure 2.12: ADS layout of a resonator mask for 50 μm thick Kapton substrate. Mask design includes MTLR and CPW resonator designs.

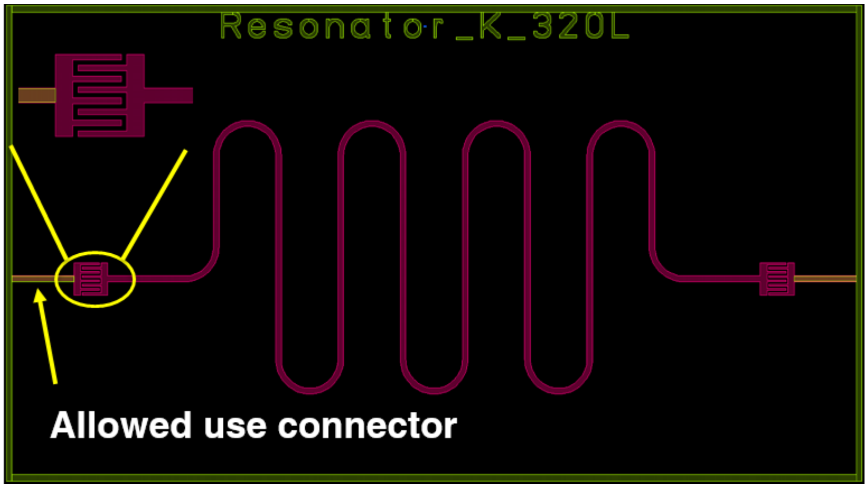

Figure 2.13: ADS layout of a MTLR for 50 μm thick Kapton substrate.

Figure 2.13 shows the layout for one of the microstrip line resonators layout. We used an interdigitated capacitor structure as the coupling gap, which was in series at each end of the resonator. In order to make connections to these resonators, we included a UBM contact pad at each end of the feed line. The ADS circuit simulation schematic is shown in Figure 2.14. Since we did not know the value of loss tangent of the Kapton before hand, this design covered a wide range of loss tangent values from 0.001 to 0.01. We adjusted the resonator sensitivity to the loss tangent by adjusting the interdigitated capacitor parameter, which included the length, the number of fingers and the gap between the interdigitated fingers.

Figure 2.15 shows the layout of a CBCPW resonator. Limited by the width of the signal line, a coupling gap was created by using an interdigitated capacitor structure. The inset picture in Figure 2.15 shows the interdigitated capacitor structure design and also the fabricated sample. To determine the capacitance value of the gap, Q3D was used. The simulation setup and result is shown in Figure 2.16. We then used this capacitance value in our ADS circuit simulation tool to obtain the RF response. The circuit simulation setup is shown in Figure 2.17.

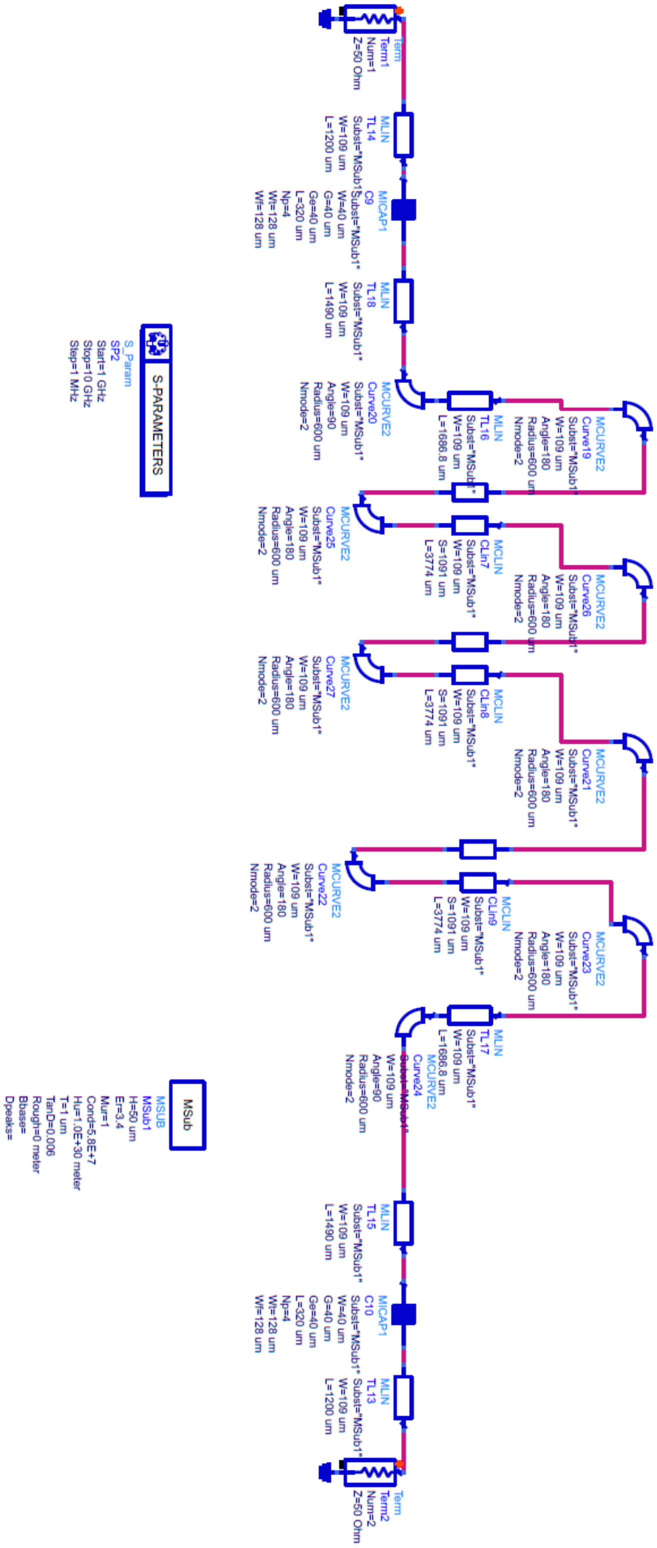

Figure 2.14: ADS circuit simulation schematic model of meander shape MTLR on Kapton.

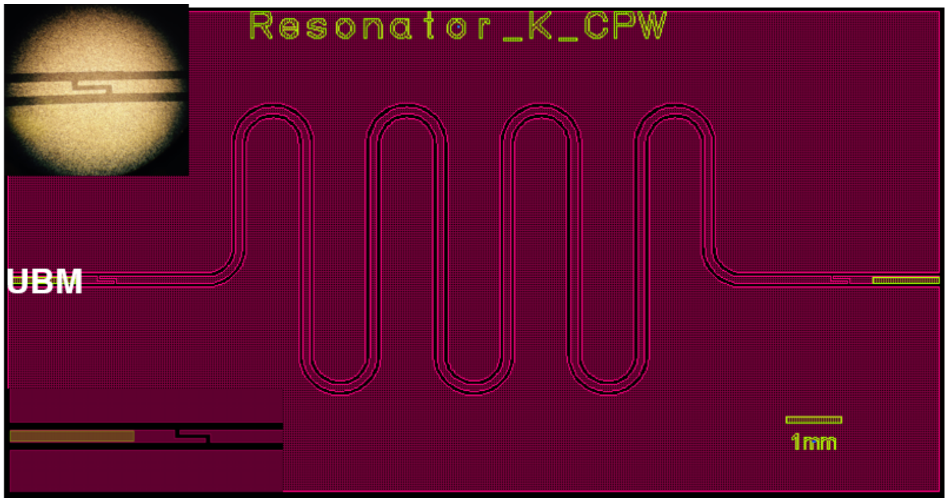

Figure 2.15: ADS layout of a CPW resonator on 50 μm thick Kapton.

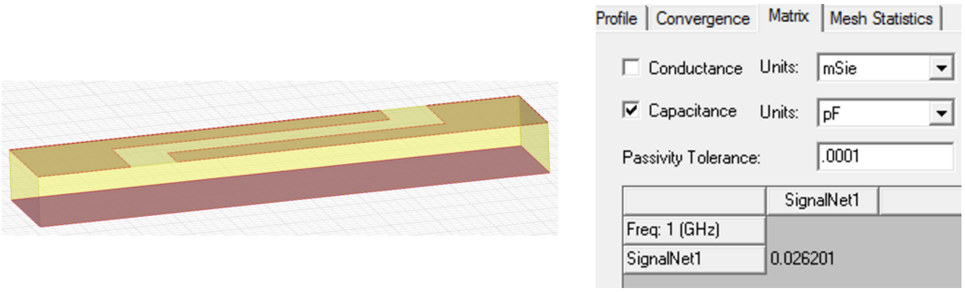

☐ Conductance Units: mSie

☑ Capacitance Units: pF

Passivity Tolerance: .0001

	SignalNet1
Freq: 1 (GHz)	
SignalNet1	0.026201

Figure 2.16: Interdigitated capacitor simulation setup and results in Q3D.

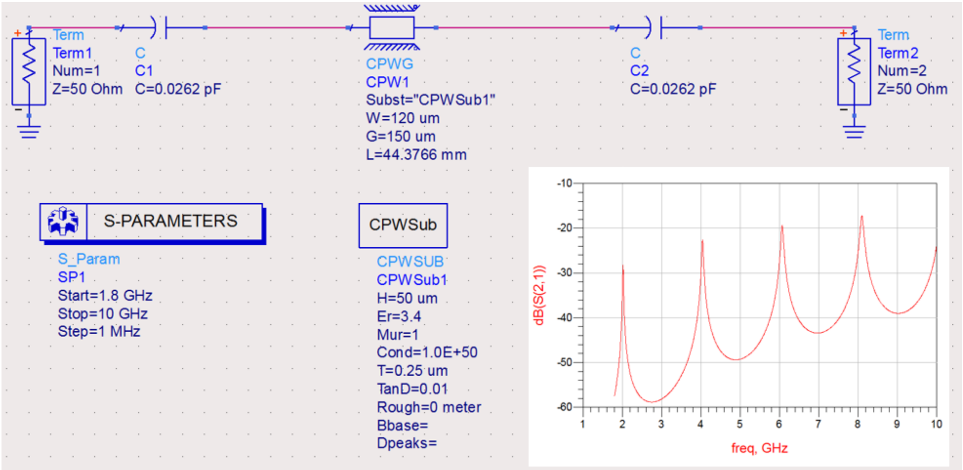

Term
Term1
Num=1
Z=50 Ohm

C
C1
C=0.0262 pF

CPWG
CPW1
Subst="CPWSub1"
W=120 um
G=150 um
L=44.3766 mm

C
C2
C=0.0262 pF

Term
Term2
Num=2
Z=50 Ohm

S_Param
SP1
Start=1.8 GHz
Stop=10 GHz
Step=1 MHz

CPWSUB
CPWSub1
H=50 um
Er=3.4
Mur=1
Cond=1.0E+50
T=0.25 um
TanD=0.01
Rough=0 meter
Bbase=
Dpeaks=

Figure 2.17: ADS CPW resonator simulation setup, inset plot is the simulation result.

2.2.2 Resonator fabrication on Kapton

The process to fabricate a NbN or Nb resonator on Kapton will be described here briefly. The fabrication details are provided in a traveler, that can be found in the appendices. First, we cut the Kapton as 4" by 4" square. We then cleaned the Kapton with acetone, methanol, DI water and dried with nitrogen air. We attached the film onto a 6" Si handle wafer for support. After a dehydration bake, we primed the surface with HMDS. We used traditional photo-lithographic methods to pattern the Kapton. For the superconducting material (Nb or NbN) deposition included a front side signal line and backside ground plane. We loaded the samples into a dc sputtering chamber and evacuated the chamber, until it reached a base pressure of $\sim 10^{-7}$ Torr. During the pump down process, we also had an oxygen filter that was used to reduce the oxygen content of the Ar gas during the sputtering process. The standard deposition process consistent of a two-minute ion mill followed by 30 mins of sputtering. For the NbN film sputtering process, we flowed N_2 with Ar during the sputtering process. Both of these sputtering processes produced a $\sim$0.25 μm thick superconducting NbN or Nb film. The metal deposition for the UBM pads consisted of an electron-beam evaporation system (E-beam) consisting of Ti($500\AA$)/Cu($5000\AA$)/Au($100\AA$). It is worth to emphasize the Cu layer thickness was critical in this UBM metallization combination. Too thin of a Cu layer led to a weak solder base and a failed solder joint. A completed resonator on Kapton is shown in Figure 2.18.

2.2.3 Measurement results of the resonator on Kapton

As described in a previous section, Cu resonators were fabricated and characterized in order to extract the real portion of the dielectric permittivity information at cryogenic temperature (6 K) for use in subsequent designs. The main reason we choose Cu instead of Nb was because superconductors exhibit kinetic inductance, especially when the measurement temperature is close to the critical temperature, and this can provide undesired shifts in the resonant frequencies leading to errors in the extracted dielectric permittivity. Furthermore,

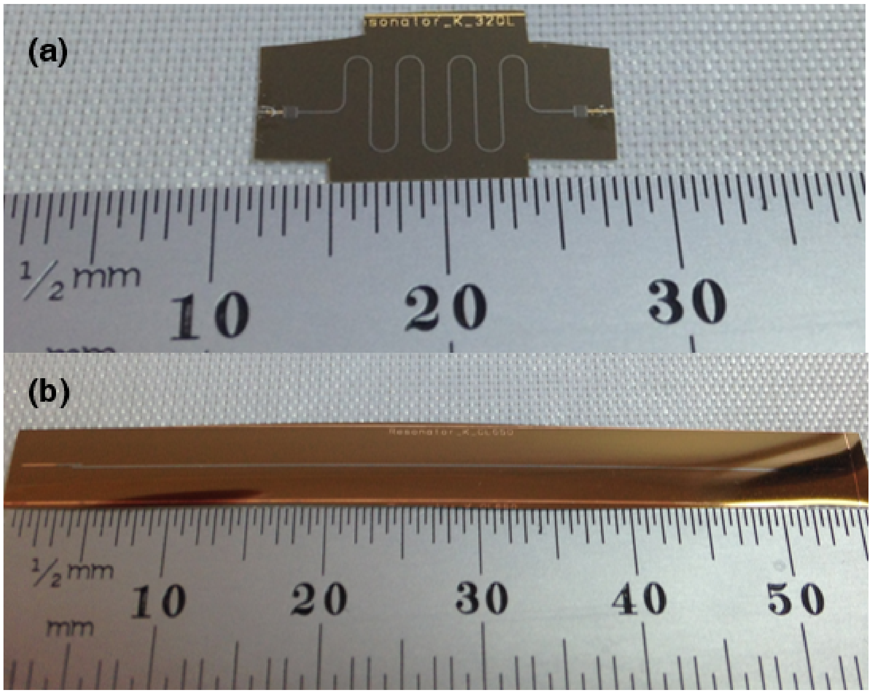

Figure 2.18: Examples of fabricated resonators on Kapton; (a) meandered MTLR and (b) straight line MTLR.

the Cu shows a stabilized conductivity over a wide temperature range at cryogenic temperatures below 15 K. We designed the Cu resonator using the data sheet value of ϵ_r of 3.4 [4] and a half-wavelength of 4.5 cm at 2 GHz. S-parameter measurement results are shown as markers in Figure 2.19. An iterative process to match ADS simulation results to the measured results was performed and the matching simulation results are shown as a red line in Figure 2.19. The conductivity value in this simulation was 169 MS/m, which is based on the sheet resistance of the Cu at room temperature of 0.0834 Ω/square and a residual resistivity ratio (RRR = R@280 K / R@15 K) of 4.22. A relative dielectric constant of $\epsilon_r = 3.2$ in the simulation provided the best agreement with the low-temperature measurements; this is slightly lower than the room-temperature data sheet value of $\epsilon_r = 3.4$. This step provided useful information for the design of the superconducting version of these resonators. In order to get the dielectric information for different temperatures, we varied only the conductivity value of Cu in our simulation and plotted these results together with the measurement at

---

[4] `http://www.dupont.com/content/dam/dupont/products-and-services/membranes-and-films/polyimde-films/documents/DEC-Kapton-summary-of-properties.pdf`

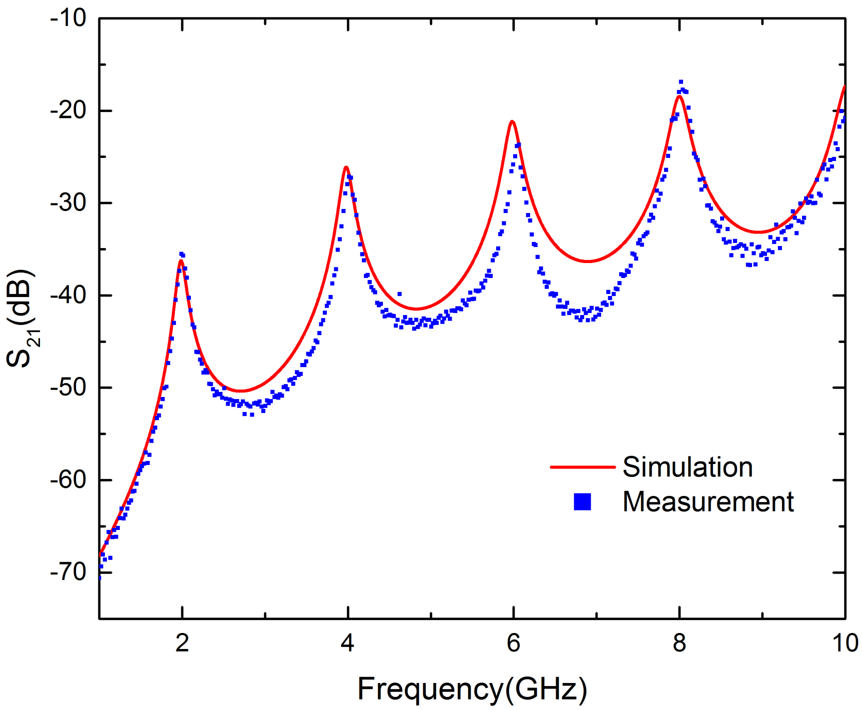

Figure 2.19: Cu microstrip resonator on 50 μm thick Kapton measurement and simulation results at 6.5 K.

various temperatures. These results are shown in Figure 2.20. From these results, we can observe the dielectric constant value is fairly stable across a wide frequency and temperature range. The conductivity values were measured on a witness SiO_2 die at different temperatures, these results are summarized in Table 2.1. The ADS schematic simulation setup of this resonator is shown in Figure 2.21.

Table 2.1: Conductivity values used in the simulation of a Cu resonator on Kapton film at various temperatures.

Temperature (K)	Conductivity (S/m)
15	1.69E+8
30	1.63E+8
77	1.09E+8
150	6.35E+7
220	4.62E+7

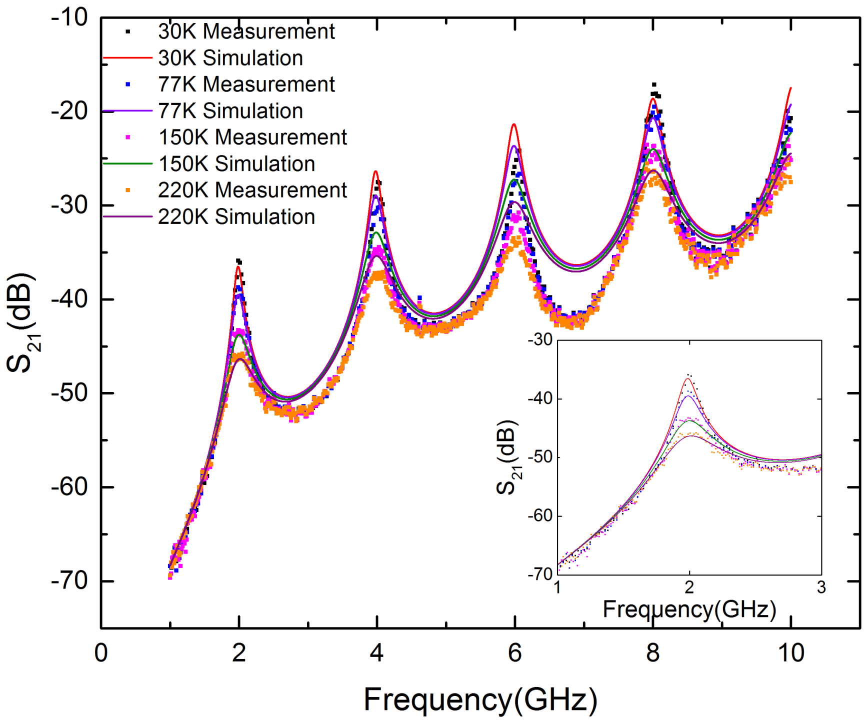

Figure 2.20: Cu microstrip resonator on 50 μm thick Kapton measurement and simulation results at various temperatures.

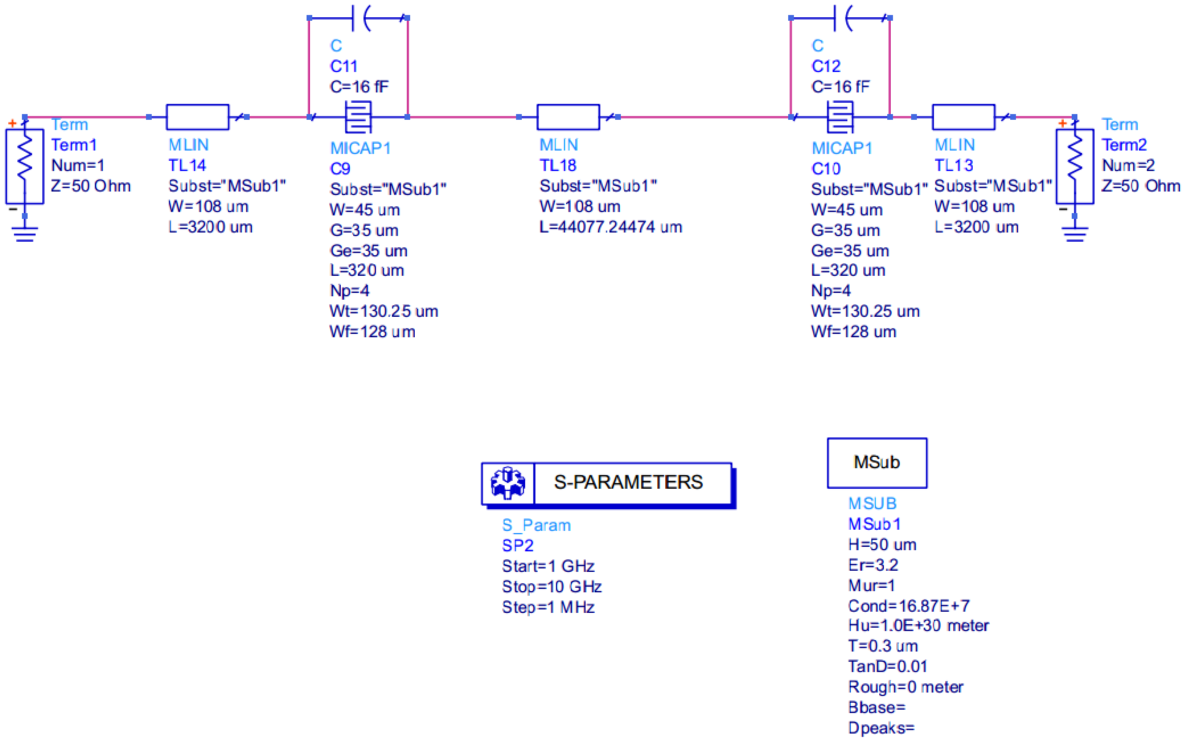

Term
Term1
Num=1
Z=50 Ohm

MLIN
TL14
Subst="MSub1"
W=108 um
L=3200 um

C
C11
C=16 fF

MICAP1
C9
Subst="MSub1"
W=45 um
G=35 um
Ge=35 um
L=320 um
Np=4
Wt=130.25 um
Wf=128 um

MLIN
TL18
Subst="MSub1"
W=108 um
L=44077.24474 um

C
C12
C=16 fF

MICAP1
C10
Subst="MSub1"
W=45 um
G=35 um
Ge=35 um
L=320 um
Np=4
Wt=130.25 um
Wf=128 um

MLIN
TL13
Subst="MSub1"
W=108 um
L=3200 um

Term
Term2
Num=2
Z=50 Ohm

S_Param
SP2
Start=1 GHz
Stop=10 GHz
Step=1 MHz

MSUB
MSub1
H=50 um
Er=3.2
Mur=1
Cond=16.87E+7
Hu=1.0E+30 meter
T=0.3 um
TanD=0.01
Rough=0 meter
Bbase=
Dpeaks=

Figure 2.21: ADS simulation setup of Cu resonator on Kapton.

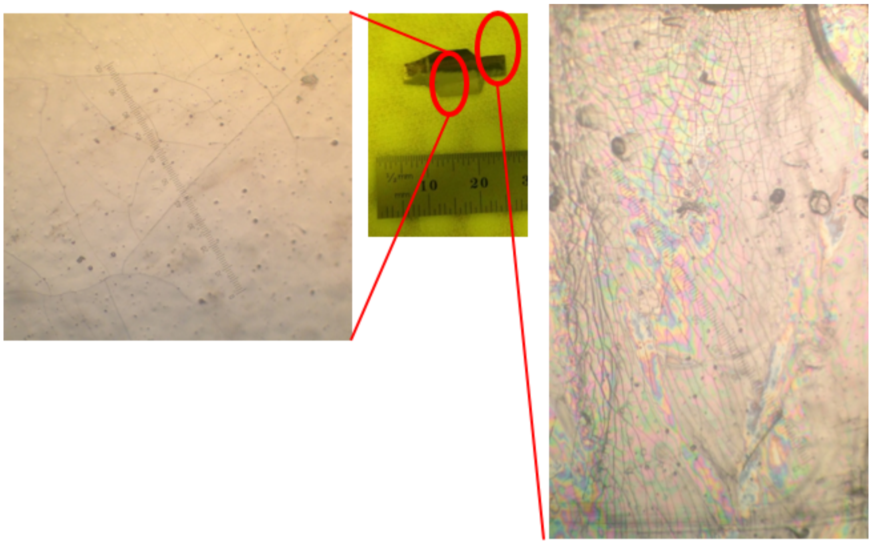

Figure 2.22: Micrograph of a Nb ground plane exhibiting cracking on the backside of the Kapton for a meandered resonator.

In order to characterize the dielectric loss tangent for the low loss Kapton at cryogenic temperatures, we required high quality factor (Q) resonators. Weakly coupled superconducting resonators provided this capability. We changed our original design from a meandered resonator to a straight resonator, because the meandered compact resonator were too short compared to the dimensions of our SMA connectors. These connectors almost contacted each other when assembled onto the sample. Since our edge launch connector was also very heavy compared to the flexible sample, routine handling began to cause cracks on the Nb film. In Figure 2.22, we show the back side of a Nb resonator (ground plane) with the meander design on the front side. We clearly observe cracks, especially at the ends of each connector region, dc measurement of this region indicated an open. The most important take away was that the Nb never exhibited superconductivity because this design caused significant fatigue on the Nb metallization. The assembled straight resonator occupied more space but minimized the handling damage compared to the shorter meandered resonator. Moreover, this design improved yield and the resonators began to exhibit superconductivity. A wide range frequency view of S_{21} measured at 4.2 K for a straight superconducting microstrip resonator on Kapton is shown in Figure 2.23.

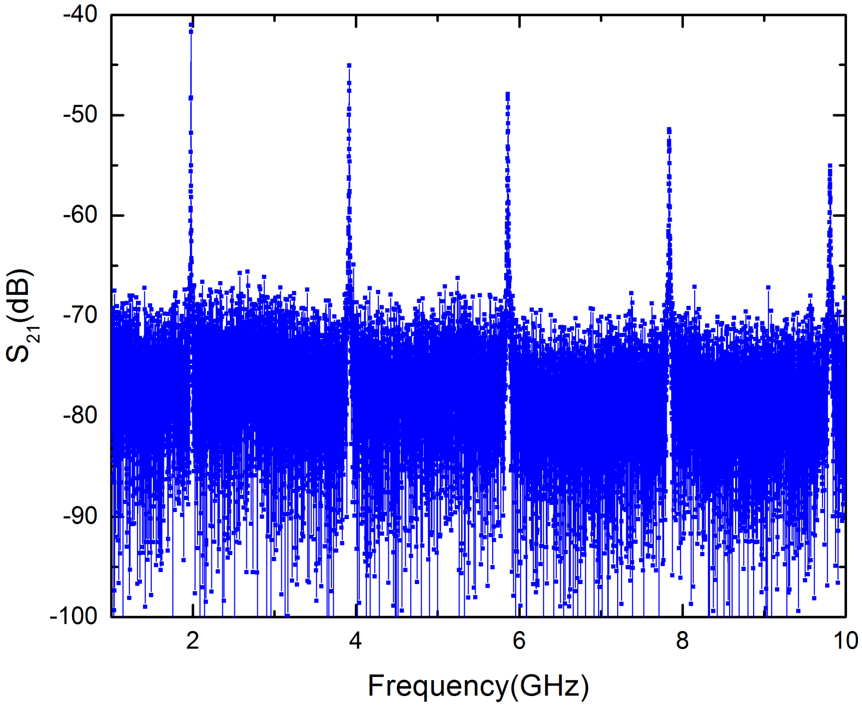

Figure 2.23: Nb microstrip resonator on 50 μm thick Kapton: S_{21} response vs. frequency at 4.2 K from 1 to 10 GHz.

The fundamental resonance shows higher Q than the other harmonics. The fundamental resonance with a corresponding Lorentz fit is shown in Figure 2.24 for a Nb resonator at 1.2 K. From this measurement, we determined the center frequency (f_0) to be 1.98 GHz with a 3 dB bandwidth (Δf) of 481 kHz, providing a loaded Q (Q_l) of 4110. We then determined the loss tangent of this Kapton film according to [64]:

$$Q = Q_d = \frac{1}{tan\delta}(1 + \frac{1-q}{q\epsilon_r}) \tag{2.2}$$

Here Q_d is the dielectric loss quality factor, tanδ is the dielectric loss tangent, and q is the dielectric filling factor. This relationship assumes the resonator losses due to external coupling, radiation, and superconductor surface impedance are all negligible. With an assumption of $\epsilon_r = 3.2$ and for the current microstrip design geometry, ADS was used to calculate a corresponding dielectric filling factor of $q = 0.706$. From these results and assumptions, we can bound the loss tangent of the Kapton film at 1.2 K and 2 GHz to be less than 0.000275.

Resultant Q factors for other harmonics at 4.2 K and 1.2 K ranged from 1300 to nearly 3300 as shown in Table 2.2. Each of the values shown in the Table 2.2 are the average value of ten measurements, in order to account for temperature drift in the measurement environment. If the dielectric and superconductor were both entirely lossless, simulations predict that the Q values in Table 2.2 would have ranged from a high of 124 000 (at the fundamental resonance) to a low of 24 800 (at the 5th harmonic), owing to the weak capacitive coupling to 50 Ω equivalent loads at each end of the resonator. Since these coupling Q values are always $>10\times$ larger than the measured Q values, our measurements accurately reflect the internal resonator Q, to better than 10% accuracy.

Table 2.2: Measured Q-factors for the first five harmonic resonances of superconducting (Ti/Nb) resonator on Kapton film at 4.2 K and 1.2 K.

center frequency f_0 (GHz)	Q @ 4.2 K	Q @ 1.2 K
1.98	2960	4050
3.92	1870	3280
5.86	1670	2740
7.84	1648	2680
9.81	1310	2220

Temperature sweeps were also performed from 6 K to 1.2 K to observe the center frequency shift and Q-factor change due to temperature-dependent changes in surface impedance. This trend can be clearly observed in Figure 2.25. The insertion loss is reduced and the extracted Q-factors become larger as the temperature is reduced further below the superconducting transition temperature. This can be understood as a reduction of both the kinetic inductance and BCS-related loss as the temperature is reduced, which leads to a corresponding frequency shift and enhanced Q, respectively. It is worth pointing out that in the present case, we used a Ti underlayer for adhesion purposes, which may potentially cause additional losses that do not result from the dielectric itself. Therefore the loss tangent values inferred from equation 2.2 are worst-case values (upper bounds). We also built Nb only resonator on this type of Kapton. The measurement results are shown in Figure 2.26, which show a higher

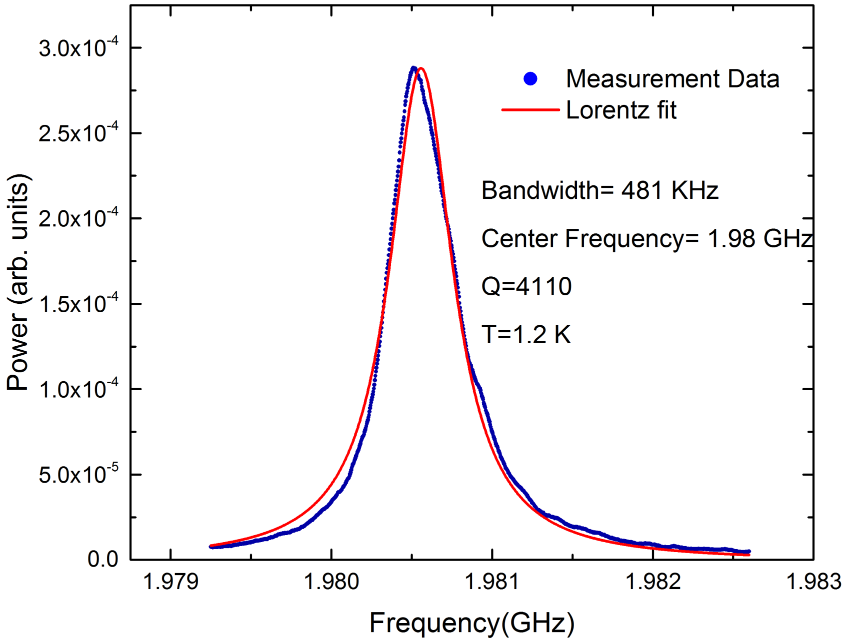

Figure 2.24: Fundamental resonance S_{21} linear response at 1.2 K and Lorentz fit for Ti(50 nm)/Nb resonator on Kapton.

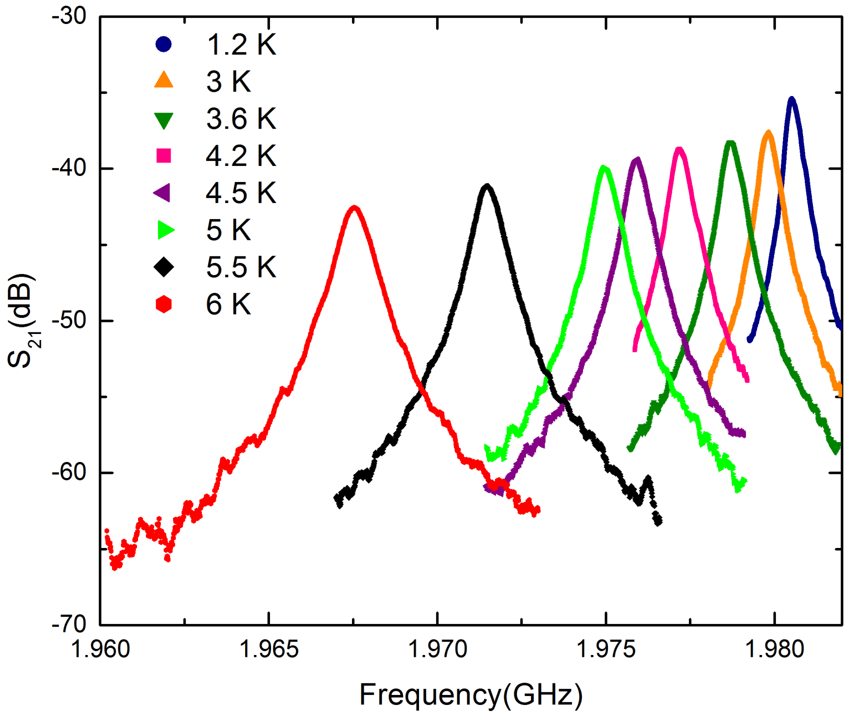

Figure 2.25: Fundamental resonance S_{21} response vs. frequency at multiple temperatures for a superconducting microstrip resonator on Kapton.

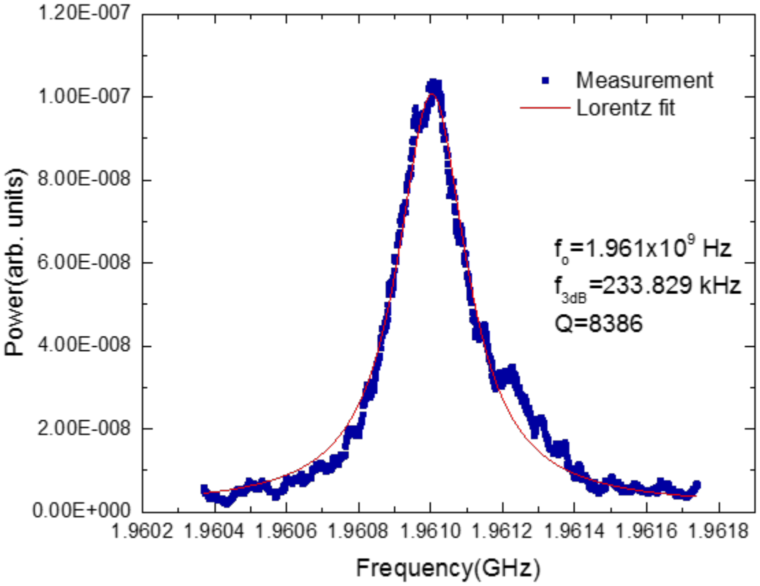

Figure 2.26: Fundamental resonance S_{21} linear response at 1.2 K and Lorentz fit for Nb resonator on Kapton.

Q-factor. These results support the assumption that the adhesion layer induces additional microwave loss.

2.3 One meter long microstrip on Kapton

Our work with Kapton also involved fabricating a meter long microstrip line. We designed a spiral microstrip pattern with two parallel signal traces, which required four edge launch connectors. The microstrip was designed to be separated into an individual flex cable. In order to separate the microstrip spiral easily, we also designed the ground plane to follow the same spiral signal lines with a width of 1 mm. The ADS layout of this design is shown in Figure 2.27. The metal stack up of this design is shown in Figure 2.28. The fabrication process was the same as the 5 cm long microstrip resonator. The completed sample before separation is shown in Figure 2.29. The final separated microstrip lines had lengths of one meter. The completed sample is shown in Figure 2.30. There were several challenges

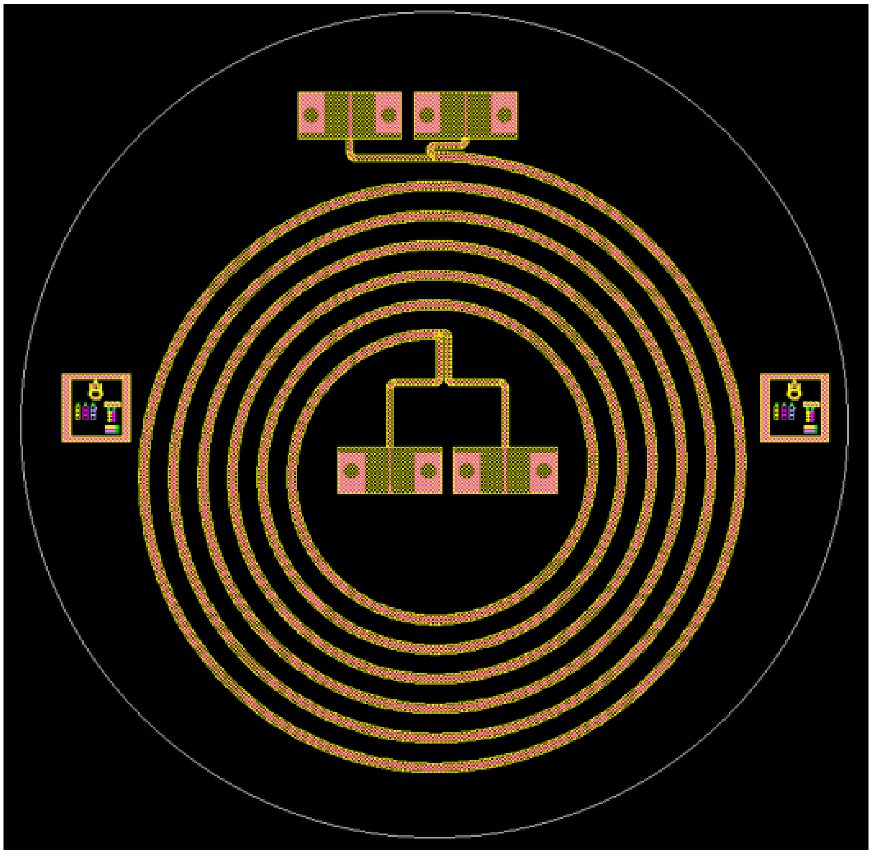

Figure 2.27: ADS layout of two parallel one meter long microstrip transmission lines for fabrication on 50 μm thick Kapton.

involved in fabricating these test samples. Low yield was a problem for this design, one Kapton film could only produce one flex cable. Therefore, during the fabrication process, we had to carefully handle and process these samples to avoid introducing additional fatigue on the metalliztion.

The measurement setup of this structure was also very challenging due to the length of the sample. We needed to ensure the signal line did not short to the wall of the measurement chamber or the ground plane. In order to measure this microstrip line in liquid helium would require additional fixtures to be made in order to streamline the measurement process.

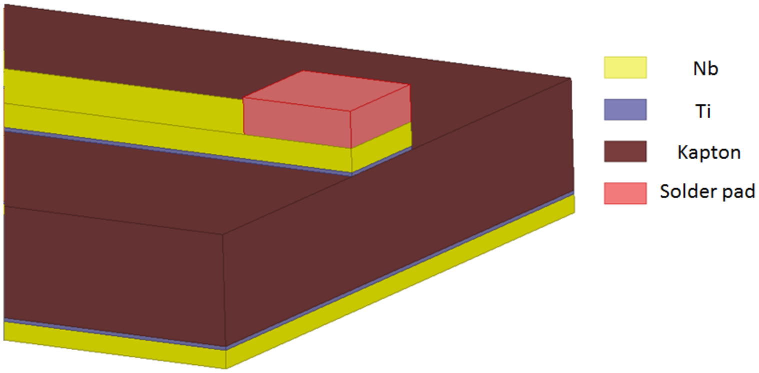

Figure 2.28: Cross section of a one meter long microstrip on 50 μm thick Kapton.

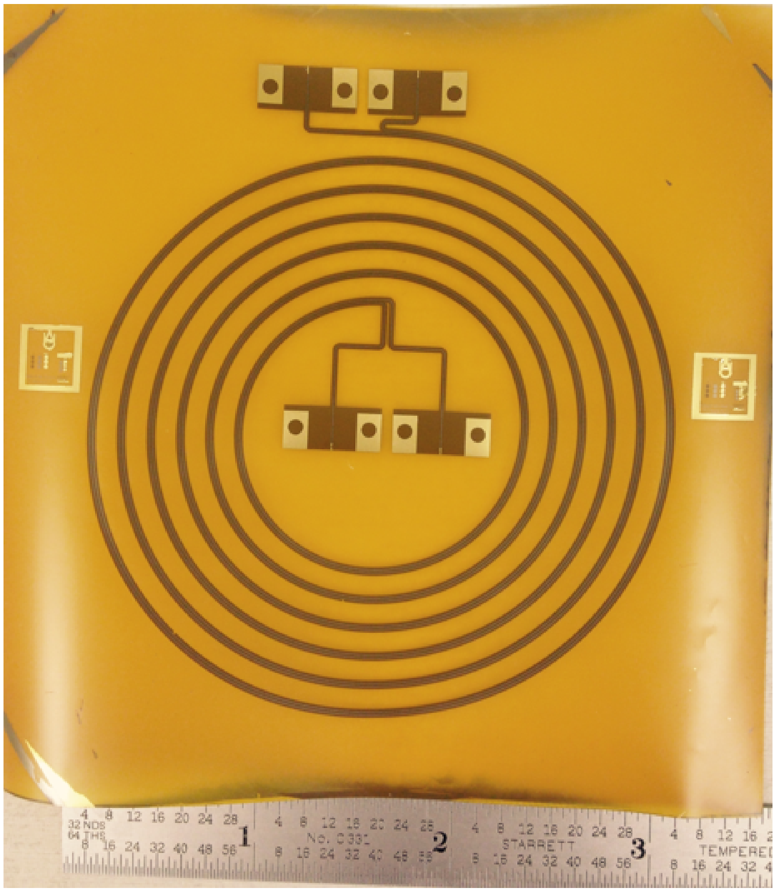

Figure 2.29: One meter long microstrip transmission line prior to being separated.

Figure 2.30: One meter long microstrip transmission line on Kapton in its final form.

Chapter 3

Microwave characterization of thin film polyimide

In order to reduce the thickness of our flexible cables that were built on 50 μm thick Kapton film, we also investigated spin-on polyimide, which yields thinner dielectric films after a spin-on and curing process. In this chapter, we explore the microwave properties of two different types of spin-on polyimide, including low stress, non photo-definable PI-2611 and photo-definable HD-4100, both of them from HD MicroSystems.

First, we attempted to extract the microwave properties by spin-on these dielectrics on top of superconducting ring resonators on AlN substrate. However, the loss tangent measurement result shows the AlN substrate dominate the loss instead of the dielectric on top of it. The second attempt was building a resonator directly on top of the dielectric films with a Si die as support. This method was also abandoned since we don't have suitable package case for measuring these type of samples. Eventually, we decided to release our resonators from the Si support wafer and measure them as a flexible device. A series of edge coupled microstrip line resonators were designed, fabricated and characterized. We extracted a broad frequency range dielectric constant using a Cu resonator to avoid superconductor kinetic inductance effects, which caused a shift in resonant frequency. We used superconducting resonators to extract the loss tangent information of both types of polyimide films at various temperatures [74]. Lastly, we report the microwave properties changes when they are exposed to a saturated humidity environment. The quality factor decreased when the sample was exposed to humidity, but it can recovered after an appropriate low temperature baking process.

3.1 Superconducting ring resonator on AlN

We initially built superconducting ring resonators on aluminum nitride (AlN) substrate. These ring resonators were fabricated on thick (500 or 635 μm) AlN substrates. The idea was to put dielectric materials on top of the ring resonator to extract the loss tangent information of these dielectric materials.

3.1.1 Design of the microstrip ring resonator on AlN

A two-port microstrip ring resonator includes microstrip feed lines, coupling gaps and a ring as shown in Figure 3.1. The gaps between the feed line and ring are a coupling capacitor. By controlling the capacitance, we can control the coupling strength. Based on the weak coupling principle, the gap dimension here has been optimized as introduced in Chapter 1. The resonance frequency can be calculated from equation 3.1.

$$2\pi r = n\lambda_g \tag{3.1}$$

where r is the mean radius of the ring and λ_g is the guided wavelength at the resonant frequencies and n is integer number of the resonance (i.e. harmonic number).

Two different iterations of designs were created based on different connector geometry and sample holder constraints. Design version one (V1), shown in Figure 3.2, was designed for GPPO connectors and the ring resonator has a conductor backed coplanar waveguide (CBCPW) transition to the microstrip ring resonator. The first iteration of this design was based on a sample holder that could only fit a ~20 mm long sample. Design V1 was eventually abandoned because the GPPO connectors were difficult to calibrate out. A ring resonator design without a transition structure proved to be a practical choice. The mask layout of this design is shown in Figure 3.3. Thus, a second design version (V2) was made that includes ring resonators with only a microstrip feed line. The yellow boxes on the ring

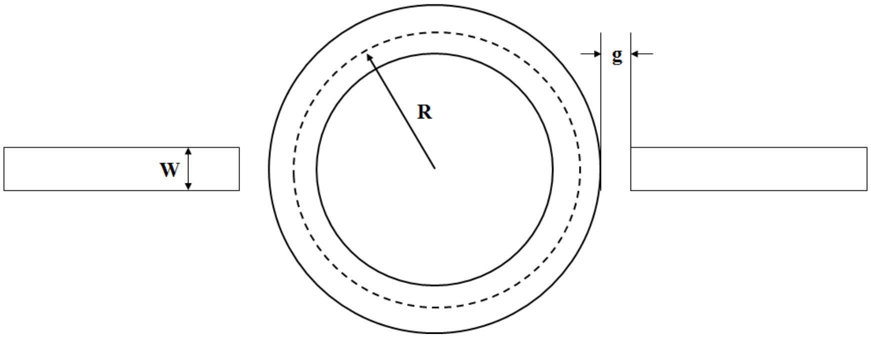

Figure 3.1: Layout of a two-port microstrip ring resonator.

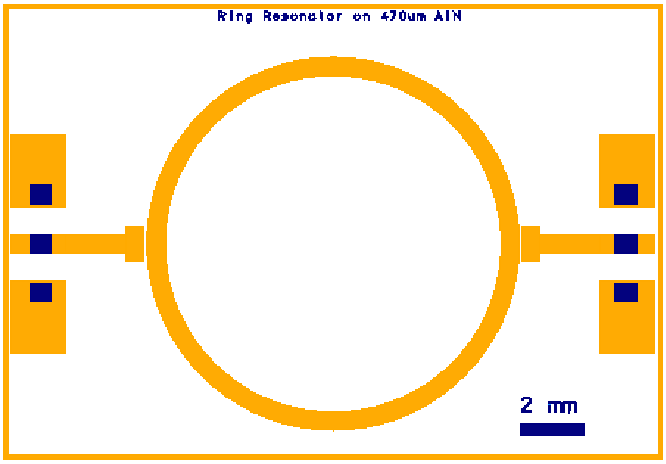

Figure 3.2: ADS layout of a ring resonator on AlN substrate.

resonator as shown in Figure 3.4 is to define discrete regions of the dielectric. A detailed discussion of the design and fabrication process is provided in next section.

3.1.2 Fabrication of the ring resonator on AlN

Ring resonators were fabricated on AlN substrates that had a nominal thickness of 470 μm. The substrates were oxidized in a furnace at 800°C for 30 minutes in dry O_2 environment. Following the thin oxide growth, substrates were transferred to a metal deposition system to sputter deposit the backside ground plane. The chamber was pumped down to reach a base pressure of 2.3 - 2.5 $\times$ 10^{-7} torr to ensure a high quality Nb film. Prior to metal deposition, a 2-minute ion mill surface clean at 1 kV is performed. Following the surface clean, Nb was then sputter deposited for 1 hour using a rotating sample holder to yield a

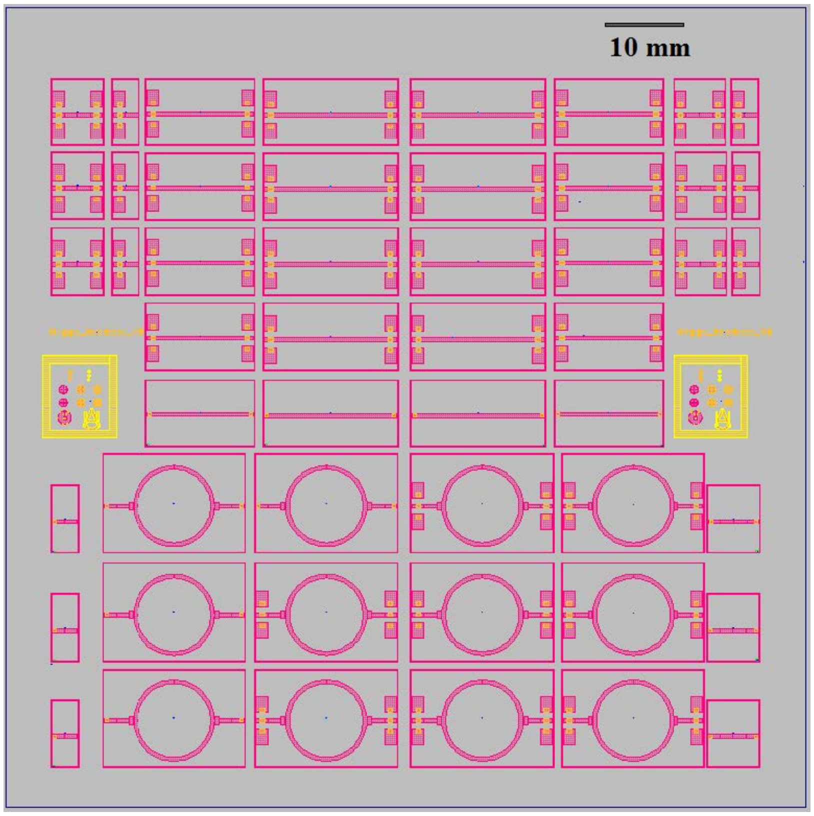

Figure 3.3: ADS layout of microstrip ring resonator designs with CPW feed lines for fabrication on an AlN substrate.

thickness of 490 nm (6 mTorr, 1 kW). After the backside sputtering was complete, wafers were transferred to a dehydration bake oven and then patterned with AZ-9245 with the ring resonator design. After the photolithographic definition of the ring resonator was completed, Nb was sputtered again using the same conditions as the ground plane. A lift-off process was then performed to complete the definition of the signal layer. An under bump metal (UBM) layer was patterned uses the same photoresist recipe. The UBM consisted of Ti/Cu/Au with thicknesses of 50/200/10 nm, respectively. The processing steps for designs V1 and V2 followed the same process flow, the only difference was the mask design. Figure 3.5 shows a schematic cross section of a ring resonator on AlN.

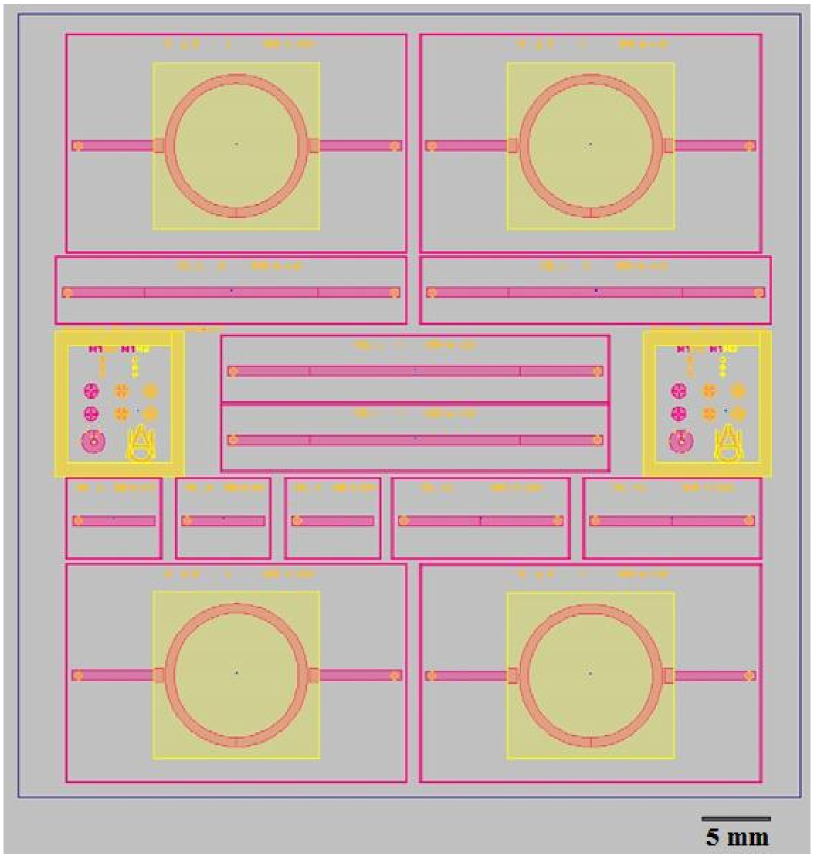

Figure 3.4: ADS layout of microstrip ring resonator designs with microstrip feed lines for fabrication on an AlN substrate.

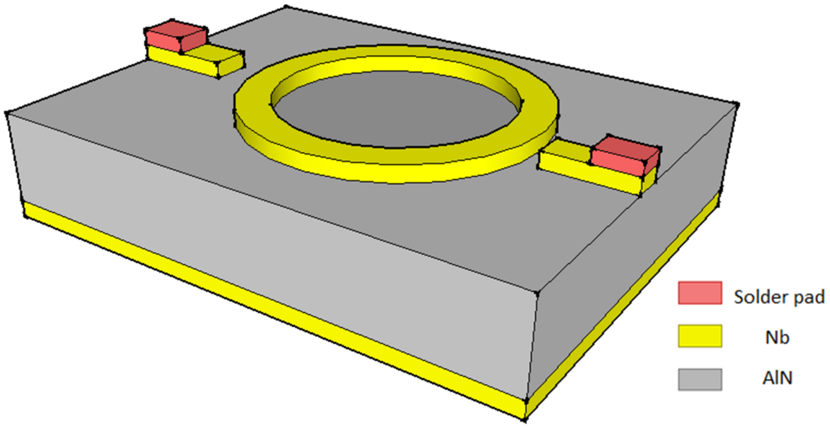

Figure 3.5: Cross section of a microstrip ring resonator on an AlN substrate.

3.1.3 Measurement results of microstrip ring resonator on AlN

The assembled ring resonator is shown in Figure 3.6. The Nb ground plane on the back side of the AlN was electrically and physically attached to a copper plate using silver epoxy. Edge launch connectors were directly soldered onto the copper plate and the signal pin of the connector was soldered onto the feed line.

The measured S_{21} response of this ring resonator is shown in Figure 3.7 and 3.8. We experimentally found that when the temperature was lower than the transition temperature, we can begin to observe the resonant peaks on the network analyzer. The S_{21} response in Figure 3.8 compares quite favorably to the included simulation result. We created an ADS RF circuit model to further analyze our measurement data from this ring resonator. This model is shown in Figure 3.9. Actual physical dimensions were incorporated into this model. From the measurement results, we find that our third resonance harmonic is not ideal, which shows higher insertion loss (S_{21}) than expected. So we added two inductors of 0.4 nH at each side of the circuit model. This extra inductance leads to a better fit to the data. The extra inductance may be caused by the way we mount our connector. This inductance is quite small, therefore it does not significantly affect the extraction of the quality factor Q or resonant frequencies.

Based on our fitting result, the AlN substrate shows a lower dielectric constant $\epsilon_r = 8.5$ at 6.1 K, compared to the room temperature value $\epsilon_r = 8.8$ reported by the manufacturer[1]. At cryogenic temperatures, dielectric material typically shows a lower dielectric constant [75]. We calculated the Q factor based on equation 1.4. From the Lorentz fitting result, we found a 3 dB bandwidth. The fitting result found using OriginLab[2], is shown in Figure 3.10. To our surprise, the manufacturer reports a loss tangent of 0.0005 at 1 GHz, but our measurements indicate a value of ~0.013 at 10 GHz, which is significantly higher than expected.

---

[1] `http://www.stellarind.com/products/ceramics/aluminum_nitride.html`

[2] `http://www.originlab.com/`

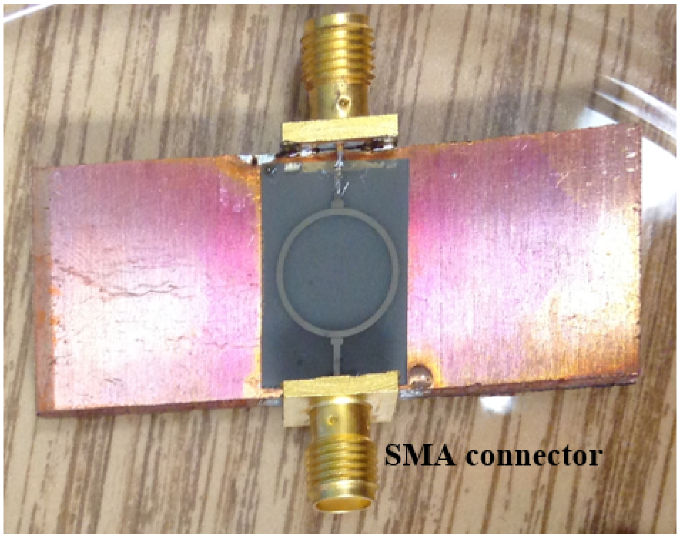

Figure 3.6: Assembled ring resonator on AlN with SMA edge launch connectors.

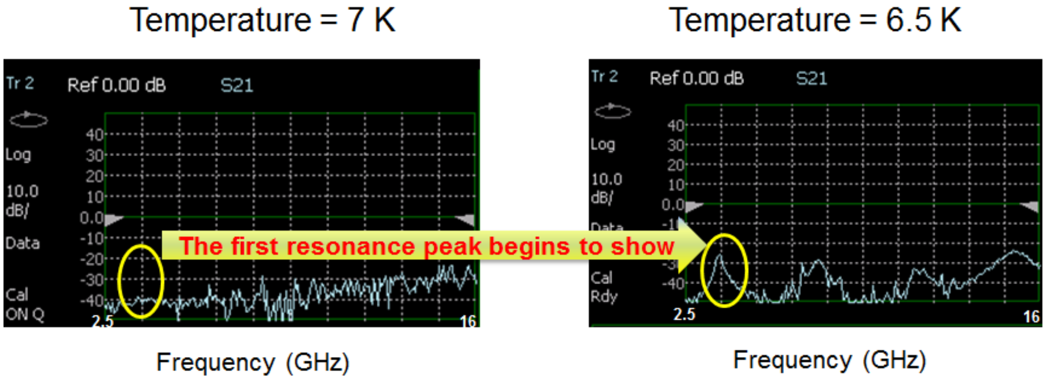

Figure 3.7: S_{21} response of superconducting resonator above and below the critical temperature of the superconductor.

Since the AlN substrate has a large loss tangent, this structure cannot provide accurate microwave loss information of the thin film dielectric. New designs based on spin-on polyimide substrates were made, which allowed us to characterize the dielectric. These structures are described in the next sections.

3.2 Microstrip transmission line resonator on thin film polyimide

In order to characterize thin polyimide films at cryogenic temperatures, we chose to design and build a series of half-wavelength, edge-coupled microstrip line resonators directly

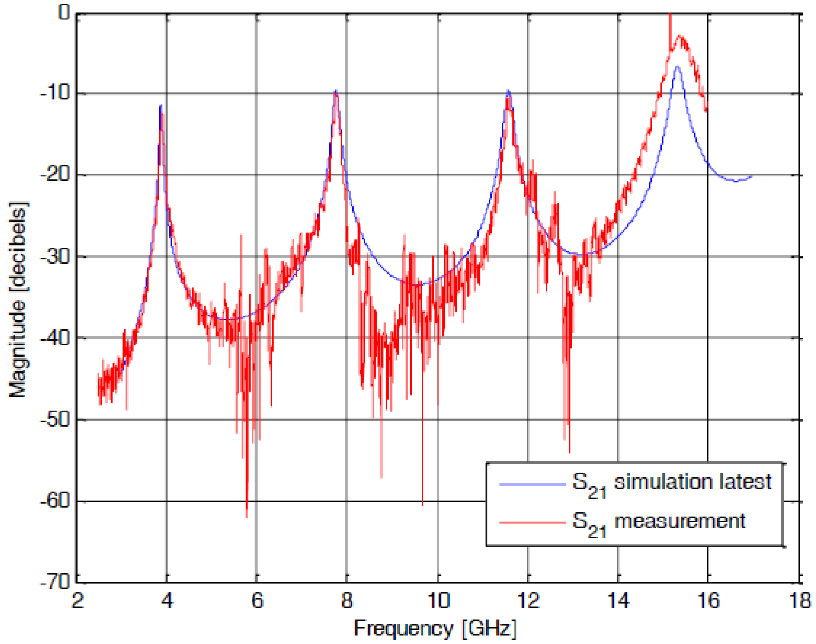

Figure 3.8: S_{21} measurement results and ADS circuit simulation for a superconducting ring resonator on AlN from 2 to 16 GHz.

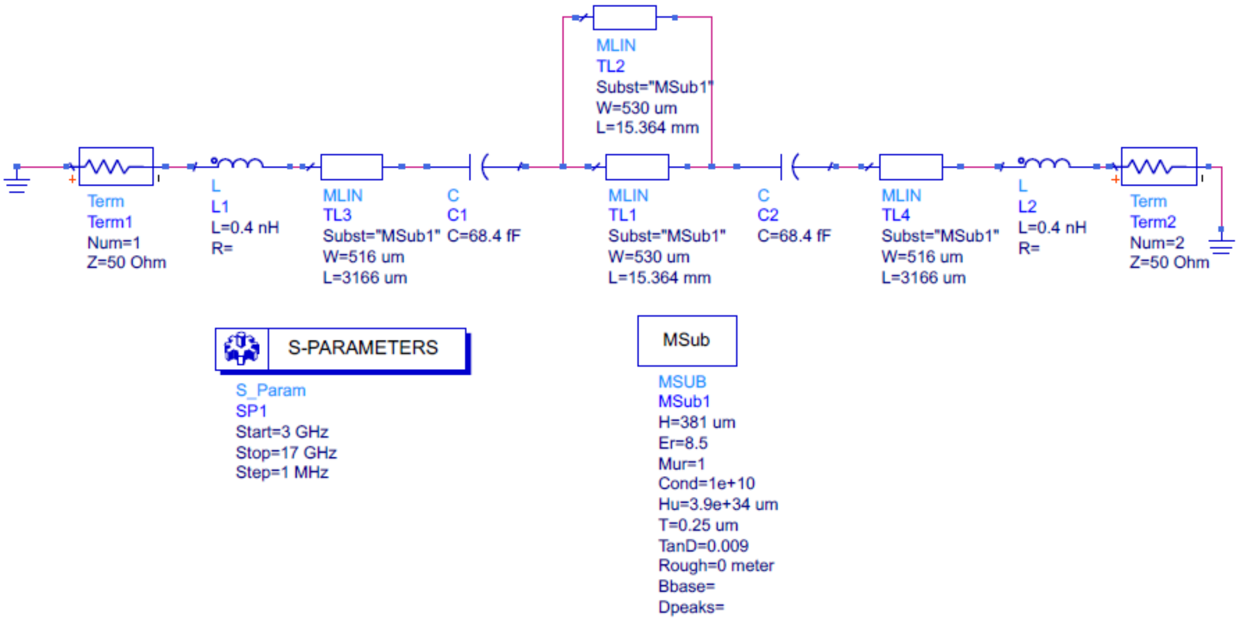

Figure 3.9: Microstrip ring resonator simulation model in ADS

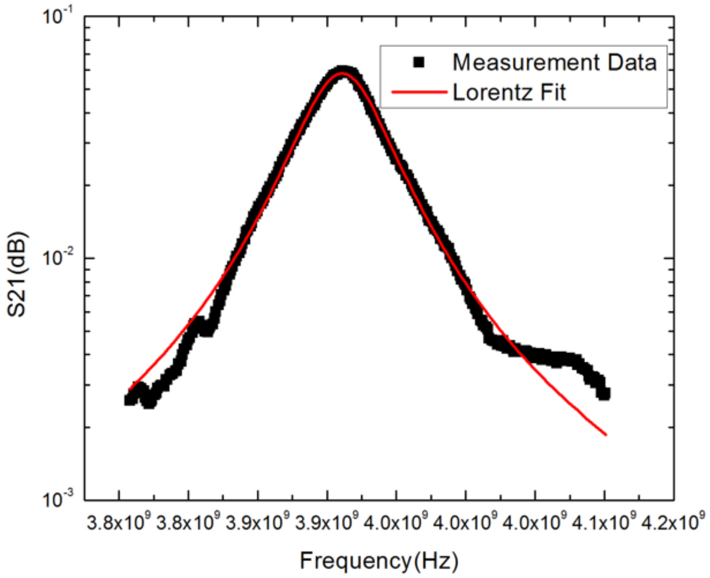

Figure 3.10: Fundamental resonance measurement result and Lorentz fit of a superconducting ring resonator on AlN.

on these films. These resonators are built on 20 μm thick spin-on polyimide films (PI-2611 and HD-4100) and were released and measured as flexible devices, which are representative of our flexible cables. First, we designed a set of resonators with ∼5 cm length corresponding to resonant frequencies of 2 GHz, 4 GHz etc. After we successfully characterized this set of resonators, a new set of longer resonators were designed, fabricated and measured in order to acquire resonance information with higher frequency resolution.

3.2.1 Design of microstrip transmission line resonator

The first idea was to build microstrip line/ring resonators on 10 μm thick PI-2611 film and the whole structure was fabricated on top of a Si support wafer. The cross section of this design is shown in Figure 3.11 and the mask layout is shown in Figure 3.12. In this mask design, we included three different coupling strengths of half-wavelength microstrip transmission line resonators, two different coupling strengths of quarter wavelength microstrip transmission line resonators and two different coupling strengths of microstrip

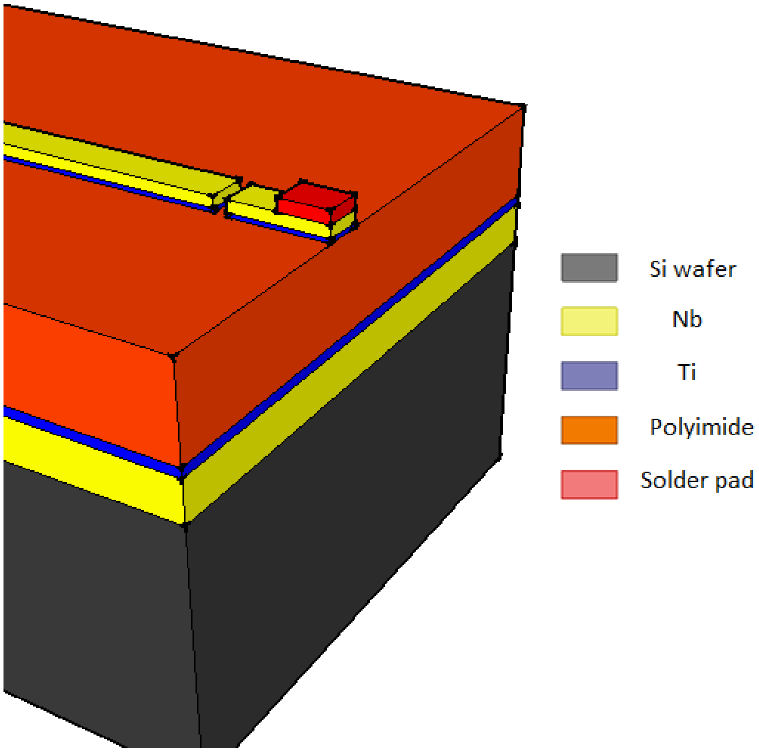

Figure 3.11: Cross section of microstrip transmission line/ring resonator on 10 μm thick spin on polyimide substrate, on top of Si handle substrate.

ring resonators. Figure 3.13 shows one type of our half-wavelength microstrip transmission line resonator with an interdigitated coupling capacitor and UBM pad at the end. Figure 3.14 shows another type of our microstrip ring resonator with an interdigitated capacitor, as well.

The design of this set of microstrip resonators on spin-on polyimide follows the same design principle as our microstrip resonators on Kapton. This design includes appropriate coupling gaps and includes different coupling structures for measuring a wide dielectric loss range. In order to show our resonators are sensitive for detecting the low dielectric loss tangent, simulation results of the resonator insertion loss (S_{21}) over a range of loss tangent values(from 0.002 to 0.004) is shown in Figure 3.15. For this type of resonator, its quality factor (Q) varies significantly with different loss tangent conditions. The simulation results

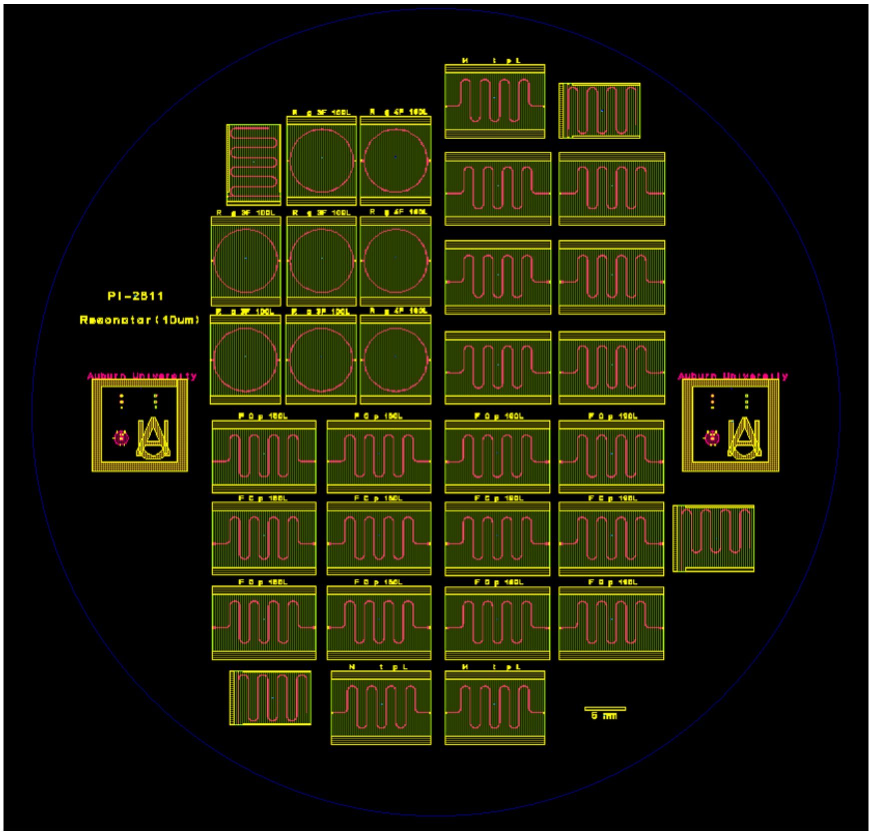

Figure 3.12: Microstrip transmission line and ring resonator mask layout for use on 10 μm thick spin on polyimide films.

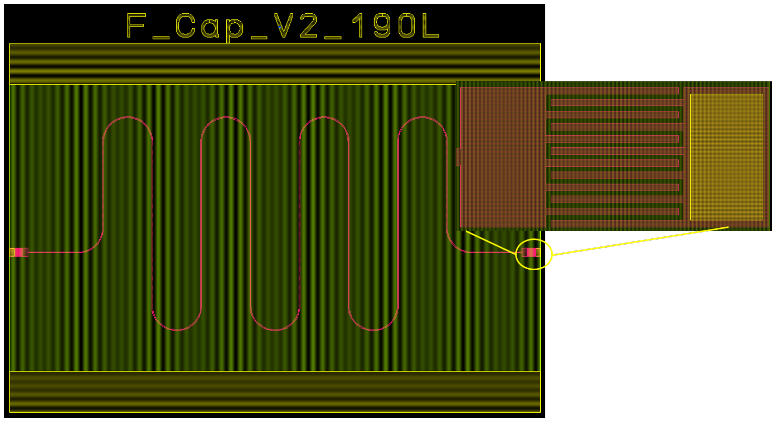

Figure 3.13: A half wavelength microstrip transmission line resonator layout for use on 10 μm thick polyimide substrates. Inset is an interdigitated coupling capacitor used in this design.

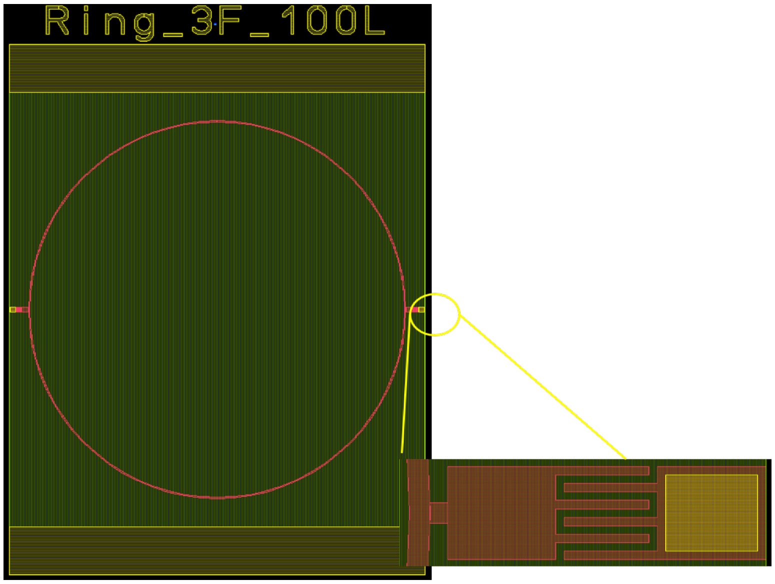

Figure 3.14: Microstrip ring resonator layout for use on 10 μm thick polyimide substrates.

are shown in Figure 3.16. This set of resonators can be used to detect dielectric loss tangent in a range from 0.001 to 0.01.

In order to make our simulation computationally efficient, we chose to use ADS circuit schematic simulator instead of ADS momentum or FEM. Although we cannot easily set up accurate superconductor surface impedance values in the ADS simulation environment, we can assume our metal as a perfect conductor, which is very close to the actual situation. Another advantage of ADS circuit simulation method is that it can generate a layout quite easily. This layout and can then be imported into Sonnet[3] simulation environment, which allows us to incorporate superconductor surface impedance information if desired. A circuit simulation model in ADS for a half-wavelength, edge-coupled microstrip resonator is shown in Figure 3.17. This allowed us to generate a meander microstrip resonator design. Interdigitated capacitors can also be found in the ADS circuit library. Figure 3.18 shows all the parameters of an ADS interdigitated capacitor. We note that, it was a sizable challenge to build a suitable measurement package for this resonator that was suitable for cryogenic measurements. As described previously, we tried to wire bond to this resonator to form a

---

[3] `http://www.sonnetsoftware.com/`

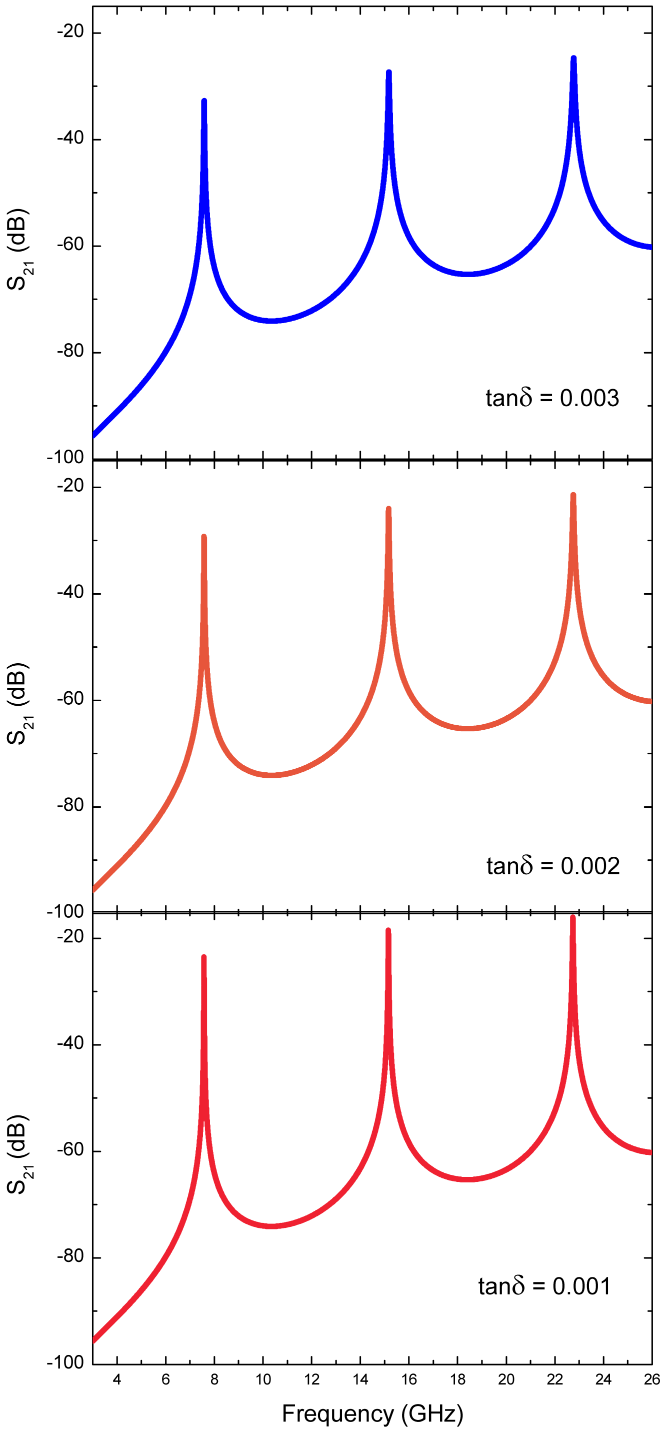

Figure 3.15: Simulation results of S_{21} response for different dielectric loss tangents of a loosely coupled microstrip resonator design on 10 μm thick PI-2611.

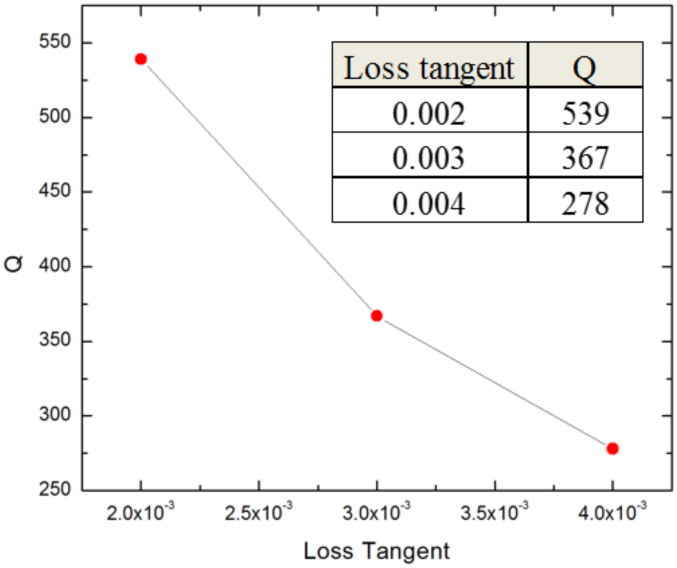

Loss tangent	Q
0.002	539
0.003	367
0.004	278

Figure 3.16: Simulation result of quality factor (Q) vs. substrate dielectric loss tangent of the resonator design on 10 μm thick PI-2611.

useful transition launch structure. We found that it was difficult to get a reliable wire bond connection since the dielectric material is soft and connection to the ground plane of the sample was not easily achieved.

Another proposed idea was to release our resonators from the Si support wafer and measured them as a free-standing, thin-film resonators at cryogenic temperatures. However, this particular meander resonator design, based on 10 μm thick PI-2611, was too easily destroyed during the releasing process, since it is very thin. Next, we designed a new set of microstrip resonators on 20 μm thick PI-2611. A 20 μm thick polyimide substrate provides a wider signal trace in a microstrip design and is less susceptible to handling damage. The width of the signal trace was 46.7 μm (for $Z_0 = 50\ \Omega$) and the length is $\sim$5 cm (for $f_0 =$ 2 GHz). The mask layout of this design is shown in Figure 3.19. Figure 3.20 shows the interdigitated capacitor structure and the solder pad area (1200 μm long and 120 μm wide). In order to make a reliable connection at cryogenic temperatures, a solder pad area was designed, which allowed connection to an edge launch SMA connector. This set of designs

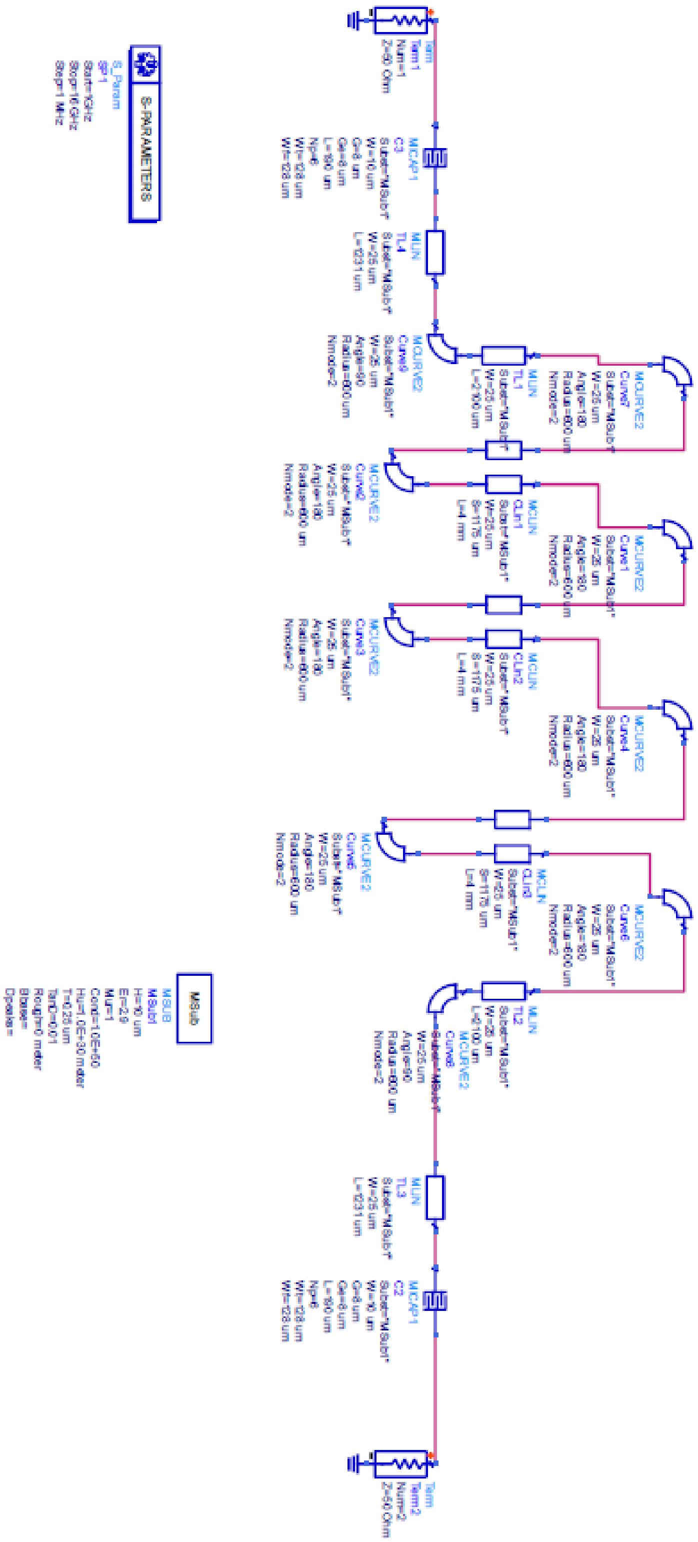

Figure 3.17: Half-wavelength edge coupled microstrip transmission line resonator simulation model in ADS.

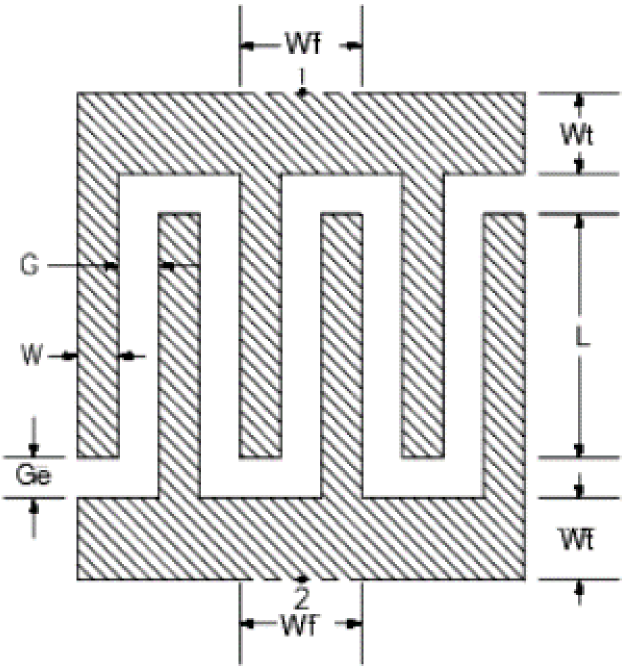

Figure 3.18: Interdigitated coupling capacitor structure shown as an ADS microstrip capacitor element.

was based on the manufacturer data sheet parameter of PI-2611 at room temperature, which indicates the dielectric constant is 2.9 and loss tangent is 0.002 at 1 kHz. Normal metal (Cu) and superconducting versions of this design were fabricated and measured at cryogenic temperatures. For the superconductor version, in order to enhance the adhesion of Nb metallization, we deposited 50 nm thick Ti as a underlayer. Figure 3.21 shows the cross section of the released microstrip line resonator.

Based on the resonator measurement results (the detail result will be shown in section 3.3), we obtained the dielectric constant is 3.2 at 4 K and the loss tangent value should be lower than the data sheet value. In order to build more sensitive resonators to extract the real loss information, we designed another set of resonators, which provided even weaker coupling strengths than the previous design. The weakest coupling strength layout of this new design set is shown in Figure 3.22. The coupling gap was 20 μm wide and the length

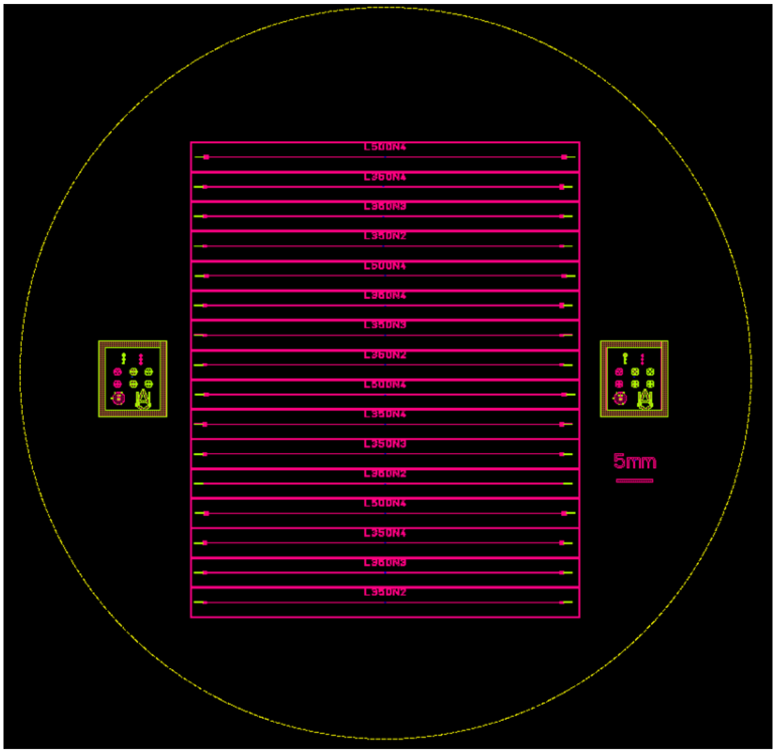

Figure 3.19: ADS layout of microstrip transmission line resonators on 20 μm thick polyimide.

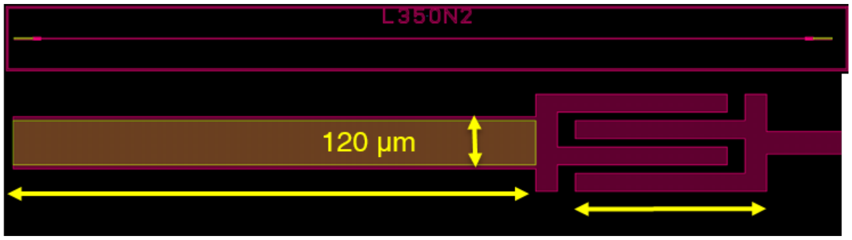

Figure 3.20: Launch and interdigitated coupling capacitor structure for a half wavelength microstrip transmission line resonator on 20 μm thick polyimide.

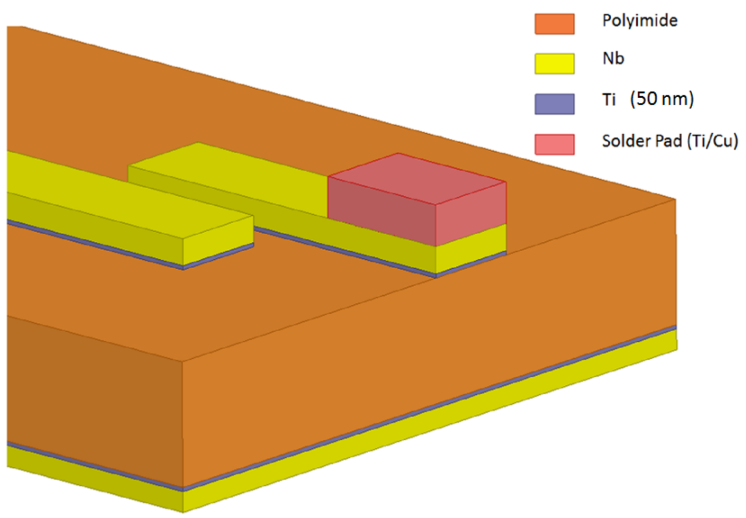

Figure 3.21: Cross section of released microstrip resonator on 20 μm thick PI-2611 substrate.

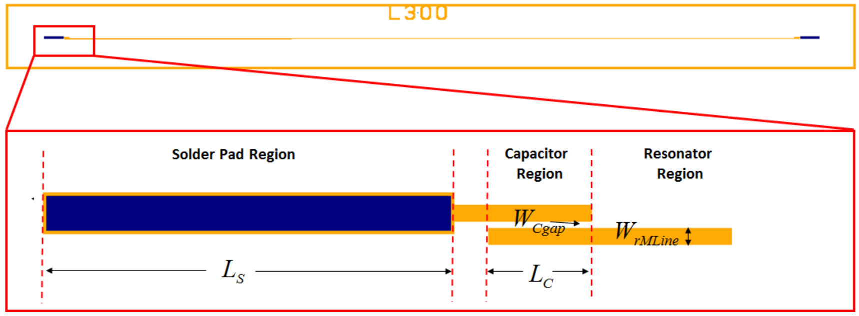

Figure 3.22: Weakest coupled microstrip resonator design on PI-2611. The length of the resonator region is 46.1 mm, L_s is 1200 μm, W_{Cgap} is 20 μm, W_{rMLine} is 47.4 μm, and L_C is 300 μm.

of the gap was 300 μm. These set of design helped us to successfully extract the low valued loss tangent information of both types of polyimide.

In order to obtain finer frequency steps in the measurement, we also designed a series of longer resonators. These designs include resonator lengths of 15 cm, 25 cm, and 55 cm, which correspond to fundamental resonant frequencies of ∼670 MHz, 350 MHz, and 270 MHz. In this design, we kept the coupling strength as the weakest one on the 5 cm long design mask. This mask layout is shown in Figure 3.23. The 25 cm long resonator design detail is shown in Figure 3.24.

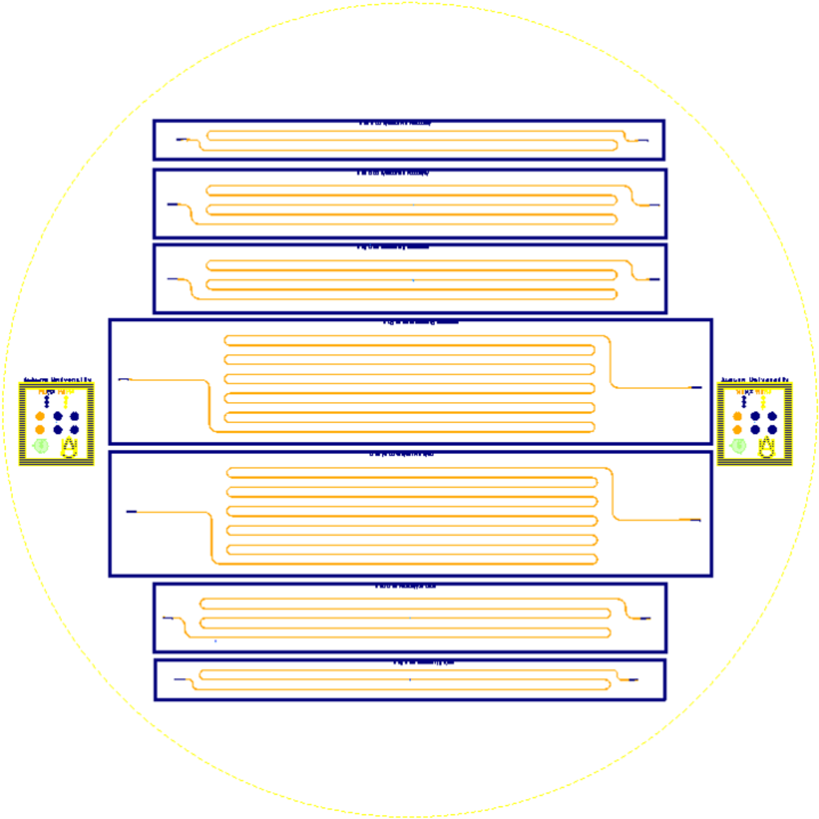

Figure 3.23: ADS layout of a series of meander microstrip transmission line resonators for use on 20 μm thick polyimide. This mask includes 15, 25 and 55 cm long resonators and corresponding length transmission lines.

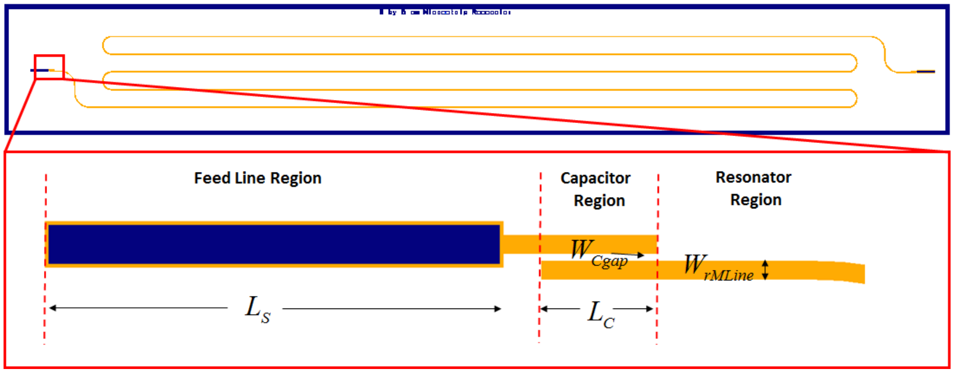

Figure 3.24: 25 cm long microstrip resonator design detail with the weakest coupling gap for use on 20 μm thick polyimide films. The length of the resonator region is 46.1 mm, L_s is 1200 μm, W_{CNb} is 20 μm, W_{rNb} is 47.4 μm, and L_{CNb} is 300 μm.

3.2.2 Fabrication of microstrip transmission line resonator on thin film polyimide

The fabrication process for free-standing PI films starts with depositing a Cr/Al (500 nm/ 2500 nm) release layer. Eventually, this layer will be etched in a NaCl solution. All the structures we build on top of the release layer will be removed from a support Si wafer [76]. On top of the release layer, a thin layer of polyimide (PI-2611[4] or HD-4100[5]) is spin-coated. After a nitrogen curing process carried at 350°C for 2 hours (program 2), this yields an approximately 10 μm thick polyimide film. We usually need to expose our film to oxygen plasma for 20 second to modify the surface before we spin on another layer of polyimide. The same curing process was repeated in a programmable nitrogen oven at 350°C. After the last curing step, we obtain a 20 μm thick polyimide film. We begin our signal pattern process after we obtain the ideal thick polyimide film by using standard photolithographic process. After depositing the signal layer and performing a lift-off process, we pattern our UBM layer. Since polyimide is sensitive to moisture, each time before we pattern our wafer, we performed a dehydration bake in 120°C oven for at least 30 mins. All the fabrication details and parameters provided in the appendix. After we finish all the fabrication process, we dice the samples and begin our release process. The releasing setup is shown in Figure 3.25 include a metal mesh served as a cathode and the sample with support Si wafer is applied a positive bias.

3.2.3 Measurement setup of the microstrip transmission line resonator on polyimide

In order to facilitate connections to the flexible resonator, we interfaced to the flex directly with edge launch SMA connectors. Limited by the dimension of the signal trace, we

---

[4] `http://hdmicrosystems.com/HDMicroSystems/en_US/pdf/PI-2600_ProcessGuide.pdf`

[5] `http://www.hdmicrosystems.com/ec/liquid-polyimides-and-pbo-precursors/products/sub-products/hd-4100-series.html`

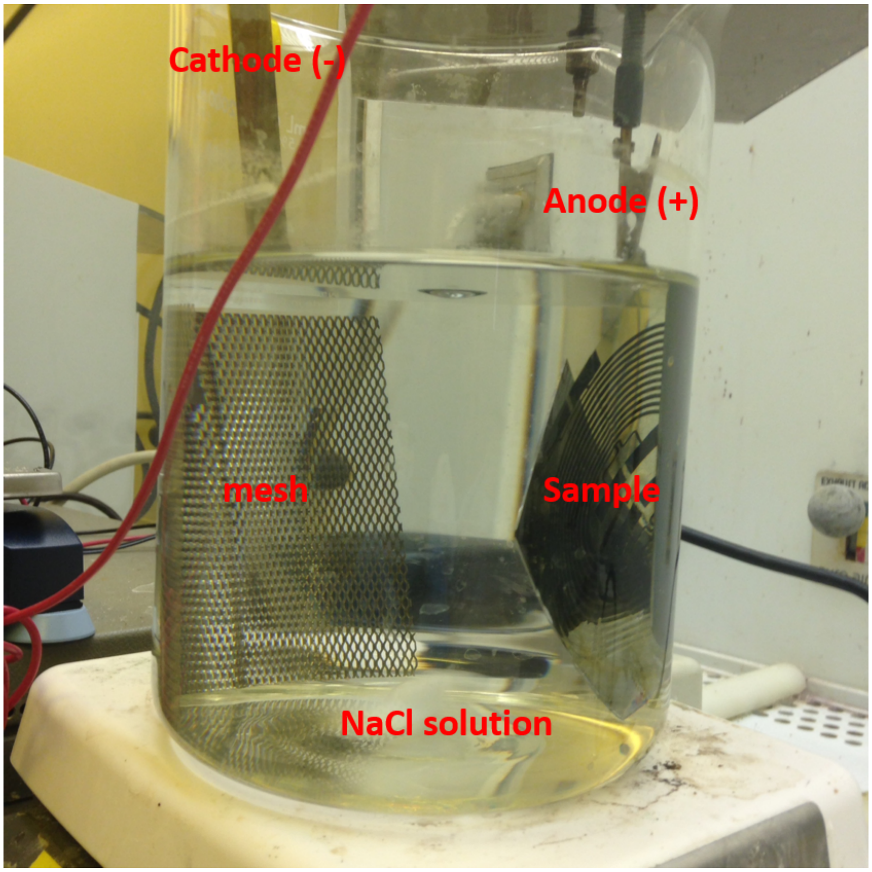

Figure 3.25: Release process setup.

chose the smallest pin size (0.005 inches) connector from Southwest Microwave[6]. In order to make reliable connections at cryogenic temperatures, we soldered the signal pin from the SMA connector to the solder pad on the flex by using high purity Indium solder. In addition, we prevented the hefty SMA connectors from straining the flexible cable by mounting the connectors and the flex onto a support board. A packaged sample is shown in Figure 3.26(b). Our test environment consisted of a pulse tube based cryostat with stainless steel cryogenic RF coaxial cables shown in Figure 3.27. The cryostat with the RF cables can stabilize at 3 K and can reach temperatures of ∼1 K. An Agilent N5227A PNA was used for measurement of the scattering parameters. The whole measurement setup shown in Figure 3.28, which include the pulse tube base cryostat, Agilent N5227A PNA, assembled sample loaded in the pulse tube for measurement and screen shot of the measurement result from PNA.

3.3 Microwave characterization results of polyimide at cryogenic temperature

Our goal is to determine the dielectric permittivity information of these polyimide dielectric films at cryogenic temperature. In order to avoid the superconductor kinetic inductance caused resonance frequency shifting, we chose Cu instead of Nb to extract the real portion of the dielectric permittivity information. The measurement result of Cu resonator on PI-2611 is shown in Figure 3.29. An iterative simulation process by using Agilent ADS was performed to match the measurement result. The matching result is shown as a red line in Figure 3.29. The inset shows the capacitor structure, the length of this interdigitated capacitor is 350 μm, the gap between the interdigitated lines and the gap at the end of the interdigitated lines are all 40 μm, the length of the resonator is 4.9 cm.

3.3.1 Characterization of dielectric loss of polyimide

Since superconducting resonator can provide higher quality factor, we build Nb resonator to extract the loss tangent value of both types of polyimide films. A wide range frequency

---

[6] `http://mpd.southwestmicrowave.com/products/family.php?family=71`

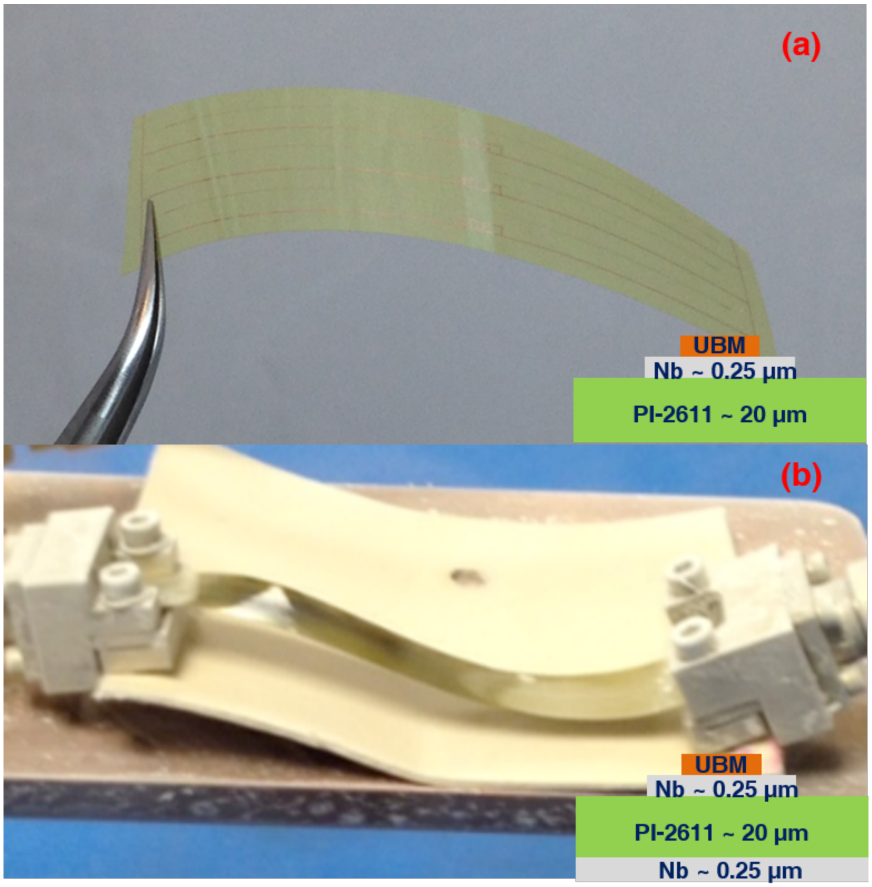

Figure 3.26: 5 cm microstrip resonator on 20 μm PI-2611: (a) released PI film with signal trace and UBM, (b) completed sample with edge lanuch SMA connectors. The inset is the corresponding cross-section.

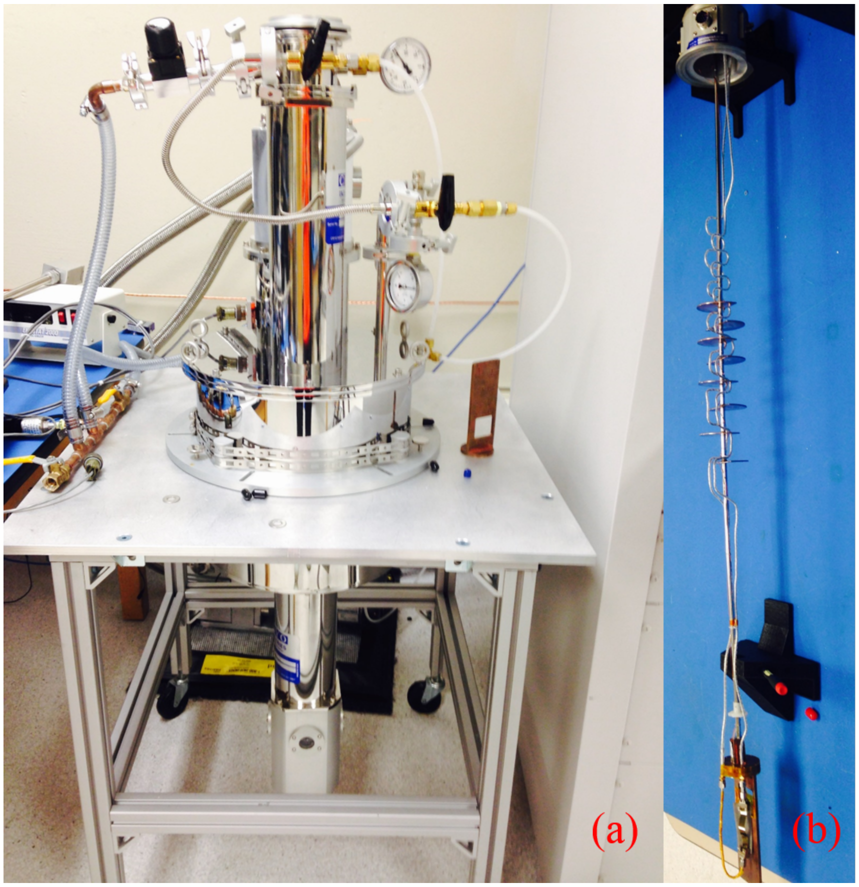

Figure 3.27: Pulse tube based cryostat: (a) measurement chamber, (b) sample holder with stainless steel cryogenic RF coaxial cables on.

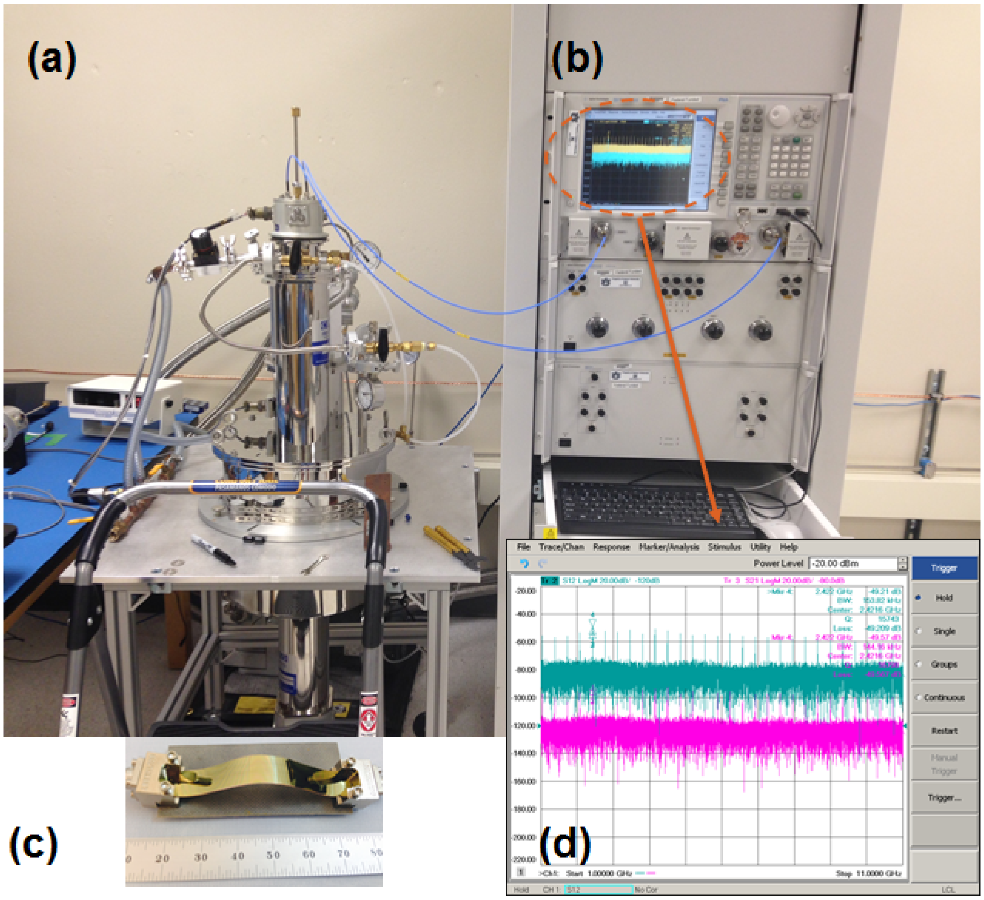

Figure 3.28: Resonator measurement setup: (a) pulse tube based cryostat, (b) Agilent N5227 PNA, (c) sample loaded in the pulse tube for measurement, (d) screen shot of a resonator measurement result from the PNA.

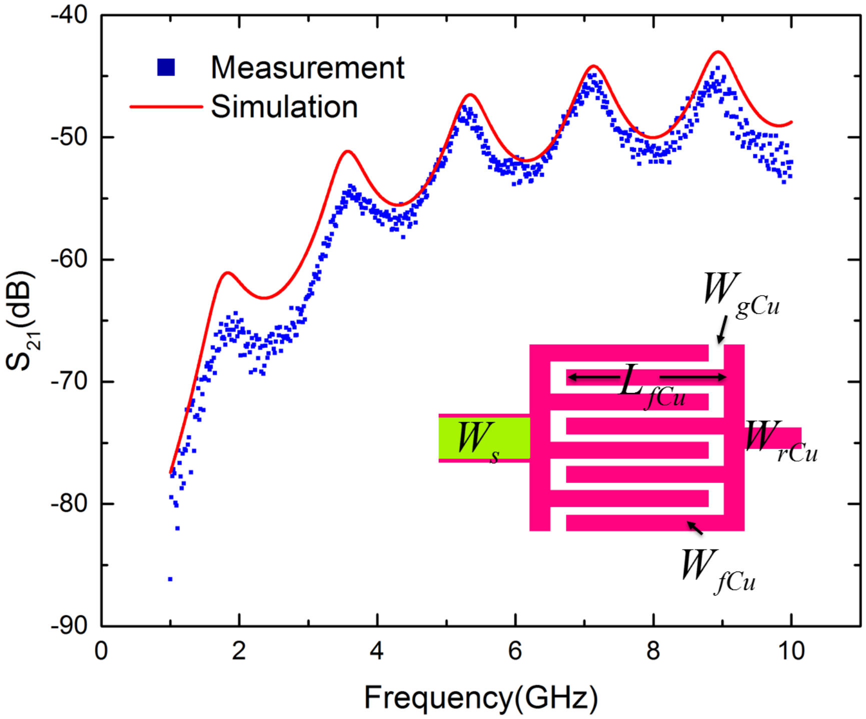

Figure 3.29: Measurement and simulation result of a Cu resonator on PI-2611 at 6.5 K. Inset is the coupling capacitor structure. The length of the resonator region is 4.9 cm, L_{fCu} is 350 μm, W_{gCu} is 40 μm, W_{rCu} is 47.4 μm, and L_{fCu} is 40 μm.

view of the fundamental resonance of resonator on PI-2611 at 1 K is shown in the inset plot of Figure 3.30. A reduced frequency range for the fundamental resonance with Lorentz fitting result is shown in Figure 3.30.

We show the impact of temperature on the fundamental resonance in Figure 3.31, which causes a shift in the center frequency towards a higher frequency and an increasing in the Q-factor as the temperature decreases. The center frequency shifts can be explained by the kinetic inductance decrease with the temperature decrease of the Nb film. The reduction of un-paired electrons leads to low BCS surface resistance is shown as increased Q-factor.

In order to determine the temperature where the BCS conductor loss is negligible, we generated $1/Q$ versus the resonance frequencies plot. For PI-2611, the $1/Q$ versus the resonance frequencies is shown in Figure 3.33 and Figure 3.34 is for HD-4100 film. In order to consider measurement error and system temperature drift, each of the measured Q factors is the average of ten individual measurement results with a three sigma error bar. Based on the

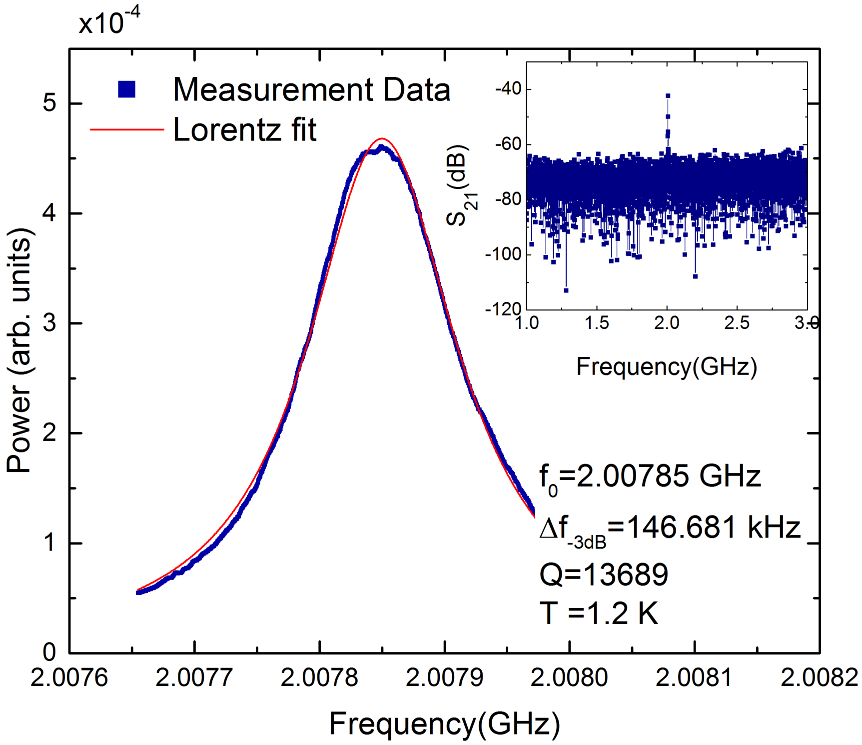

Figure 3.30: Fundamental resonance of a Nb resonator on PI-2611 at 1.2 K. The inset is a wider frequency view for the fundamental resonance.

basic LRC resonator theory $Q \times f_0 = Constant$, a $1/Q$ versus the resonance frequencies plot should yield a straight line. If the BCS resistance is significant, then at different temperatures the slope of the line should decrease with temperature decrease until the slope does not show a strong temperature dependence. We can clearly observe the BCS loss has a significant effect on the Q-factors in the temperature range from 4.2 K to 3 K. We deduce from the plot, the BCS loss decreases when the temperature decreases, which follows the theory as expected. In Figure 3.33 and Figure 3.34, the measurement data at ~1 K shows an almost parallel slope to the simulation ideal case ($\tan\delta = 0$). This indicates the Nb has minimal BCS loss at this temperature. Therefore, the Q-factor mainly represents the dielectric loss at ~1 K. At present, the 2nd harmonic does not fall in-line as the other harmonics, which exhibits a lower Q than expected. Numerous samples have been fabricated and measured and all have lower Qs than what would be expected by theory. This abnormality with the second harmonic can be caused by the measurement chamber and/or humidity, at present, these all seem to

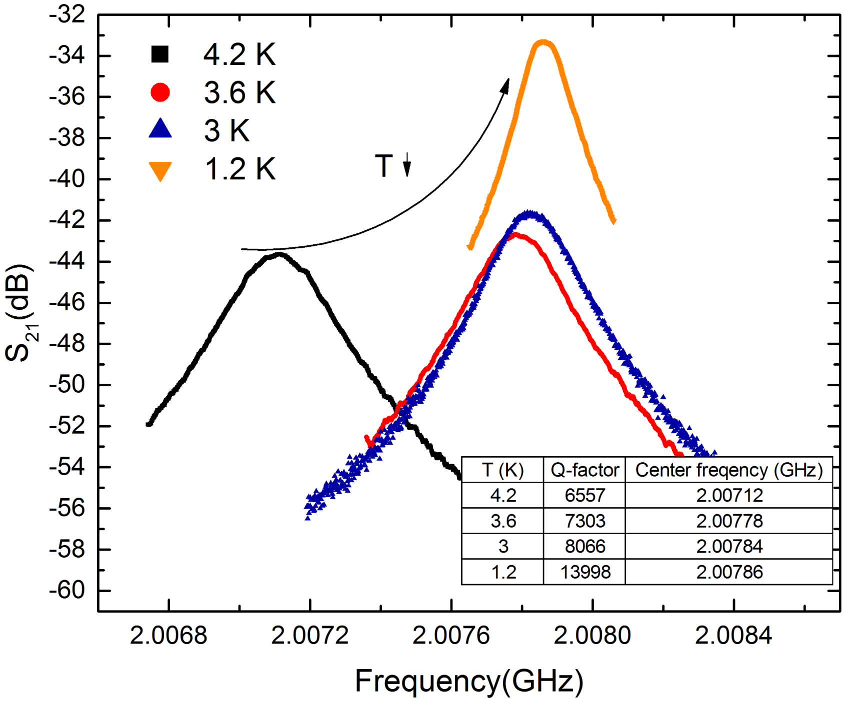

T (K)	Q-factor	Center freqency (GHz)
4.2	6557	2.00712
3.6	7303	2.00778
3	8066	2.00784
1.2	13998	2.00786

Figure 3.31: S_{21} of fundamental resonance response of a Nb resonator on PI-2611 at multiple temperatures. The inset table lists the center frequency and Q-factor as functions of temperature for the fundamental resonance.

be contributing factors and is therefore excluded from the plots for clarity. The summary of the quality factor and loss tangent (tanδ) information of both types of polyimide is present in table 3.1.

Q factors are strongly power dependent as shown in Figure 3.32. The driving power has a square relationship with the current transmitted through the resonator [77]. By increasing the driving power, the resonance frequency tends toward lower frequencies, the measured Q-factor drops and exhibits non-linearity in the rising part of the S_{21} as shown in Figure 3.32. This non-linearity can be explained by the current flow in the superconductor trace break the weak links that exist at the edge. This directly describes the surface impedance increase when the input power increases in the resonator due to extra metal loss [78]. For our resonator, Q factors show a significant decrease when the driving power is above -25 dBm as shown in Figure 3.32. We therefore carefully chose an appropriate drive power level to extract the Q-factors at each harmonic.

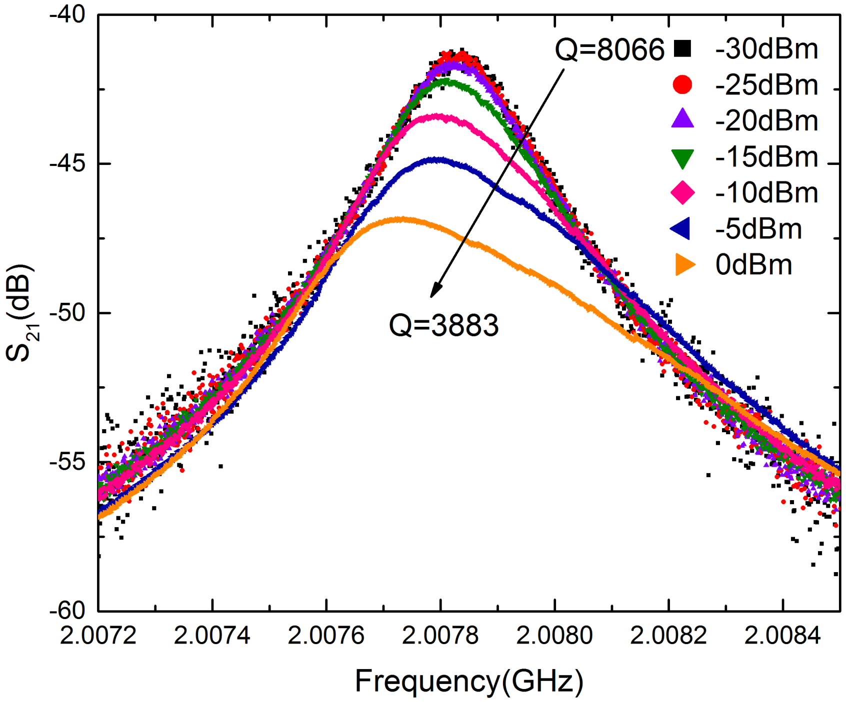

Figure 3.32: Fundamental harmonic response of a Nb on PI-2611 resonator at 3 K for different power levels incident at the sample. The range of loaded Q values is shown. Due to the obvious nonlinearity at higher powers, Q was calculated from the measured 3 dB bandwidths, rather than fitting to a Lorentzian function.

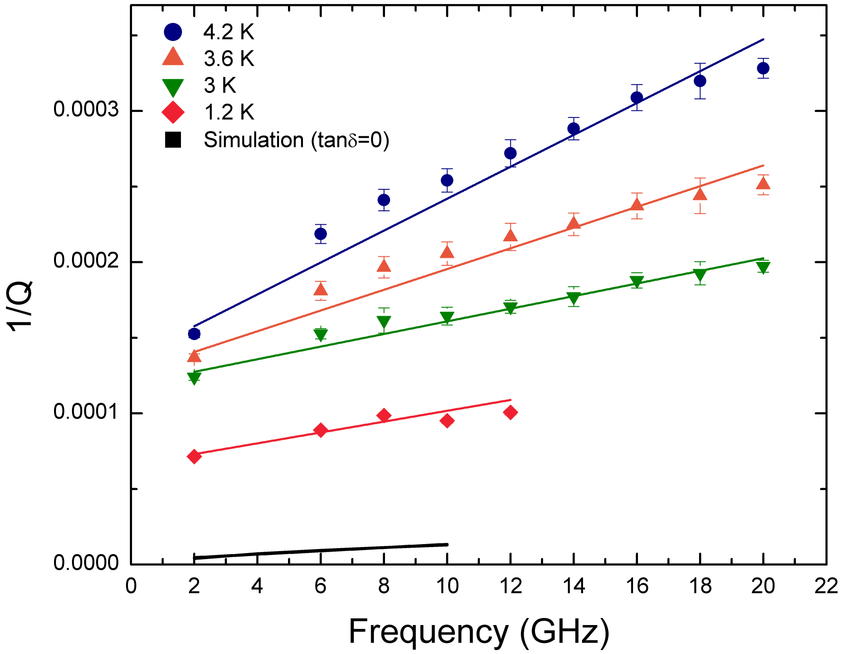

Figure 3.33: $1/Q$ vs. resonance frequencies for a Nb resonator on PI-2611 from 4.2 K to 1.2 K. Simulation results with $\tan\delta = 0$ are also shown at 1.2 K.

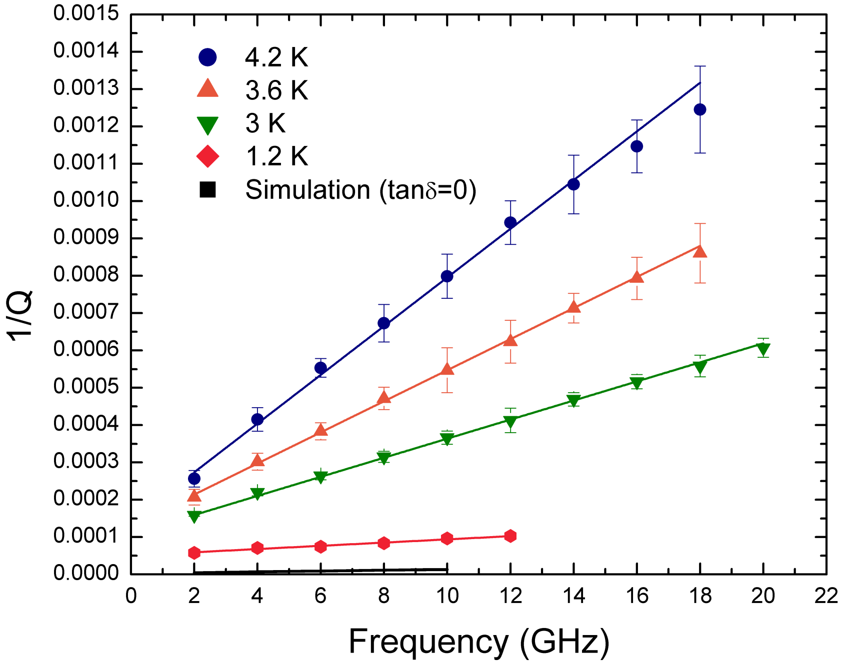

Figure 3.34: $1/Q$ vs. resonance frequencies for a Nb resonator on HD-4100 from 4.2 K to 1.2 K. Simulation results with $\tan\delta = 0$ are also shown at 1.2 K.

Table 3.1: Measured loaded Q-factor and calculated dielectric loss tangent ($\tan\delta$) at multiple frequencies at ~1.2 K for PI-2611, and at both 1.2 K for HD-4100. The $\tan\delta$ calculation corrected for the coupling Q and the non-unity dielectric filling factor of the microstrip. We assume no other loss mechanisms at these low temperatures, and so the actual loss tangents may be smaller than shown.

$\sim f_0$ (GHz)	Q_{coup}	PI-2611 @ 1.2 K	HD-4100 @ 1.2 K
2	251 000	13 200 (8.21E-5)	17 300 (6.07E-5)
4	139 000	7 880 (1.35E-4)	14 100 (7.19E-5)
6	106 000	10 500 (9.72E-5)	13 400 (7.34E-5)
8	88 400	9 170 (1.10E-4)	12 000 (8.17E-5)
10	77 300	9 660 (1.02E-4)	10 400 (9.42E-4)
12	75 400	8 870 (1.12E-4)	9 710 (1.01E-4)

3.3.2 Humidity effects on thin film polyimide dielectric constant

Polyimide films are known to be sensitive to humidity. We therefore studied the impact of humidity on the dielectric properties of PI-2611 and HD-4100 at cryogenic temperatures. Tests were carried out in a saturated humidity chamber (99% and above humidity) and at room temperature. Resonators were placed in the humidity chamber for varying amounts of time and then transferred to the pulse-tube refrigerator for measurement. The resonators were then baked at 90°C in vacuum oven and re-measured. Measurements of these resonators after humidity exposure exhibited a shift in the resonance frequencies and decrease in the quality factor. After a bake out, the quality factors recovered (within measurement error).

We quantify changes in the dielectric by calculating the effective dielectric constant(ϵ_{eff}) relative to the post-bake value. We use the effective dielectric constant because our resonator structure is in a microstrip configuration. We use the relationship shown in equation 3.2 to determine the effective dielectric constant.

$$nf_0 = \frac{c}{l\sqrt{\epsilon_{eff}}}, n = 1, 2, 3... \tag{3.2}$$

n is the harmonic number, f_0 is center frequency, l is the length of the resonator, c is the speed of light in free space and ϵ_{eff} is the effective dielectric constant.

Since we are using Nb as the conductor metallization and it exhibits kinetic inductance, we cannot directly obtain ϵ_{eff} because the kinetic inductance induces a shift in the resonant frequency. We therefore used the same resonator for each of the experiments to avoid variations in the kinetic inductance. Moreover, since the kinetic inductance shows a temperature dependence, we ensured the measurement temperature was consistent throughout the experiments. We therefore can calculate the $\Delta\epsilon_{eff}$, which is defined in equation 3.3.

$$\Delta\epsilon_{eff} = (\frac{c}{nl(f_{0,bake} - f_{0,humidity})})^2 \tag{3.3}$$

$f_{0,bake}$ is the center frequency of each resonant frequency after recovery bake. $f_{0,humidity}$ is the resonant frequency after humidity treatment. We used a 25 cm long Nb resonator with a fundamental resonance frequency of ∼350 MHz, but only measured the center frequencies at ∼1 GHz. We performed two types of humidity exposure tests, a long term humidity exposure and recovery bake and varying-humidity exposure and recovery bake to observe when humidity saturation may occur.

A long term humidity test and recovery bake cycle consists of two steps. First, the sample is placed in a saturated humidity environment (∼100%) for one hour and then transferred to a pulse-tube refrigerator for measurement. Measurements are undertaken at 4.2 K and 1.2 K and then the sample is removed from the pulse-tube refrigerator and brought back to room temperature in a drying tube. The second step consists of baking the sample in a 90°C vacuum oven for two hours (recovery bake). The sample is immediately transferred into the pulse-tube refrigerator and measured again at 4.2 K and 1.2 K. These two steps consist of one cycle. The humidity-recovery cycle is repeated three times for each sample.

The relative effective dielectric constant as a percentage change during the long-term treatment cycles is shown in Figure 3.35(a) for PI-2611 and in Figure 3.35(b) for HD-4100. These tests reveal the effective dielectric constant doesn't change significantly during the humidity and recovery-bake treatment. Moreover, the effective dielectric change percentage does not appear to have a frequency dependence, although the PI-2611 film exhibits more variation than the HD-4100 during these measurements.

In addition to the long term testing, we also performed shorter exposures to humidity to determine when the film would saturate. This process included exposing the sample in a saturated humidity chamber for 5, 15, 30, and 60 minutes, followed by a two-hour bake process in between each of the humidity treatments.

The characterization results for various humidity exposures times at 4.2 K and 1.2 K are shown in Figures 3.36 and 3.37 for both PI-2611 and HD-4100. We note that PI-2611 has greater sensitivity to humidity, as the time is increased and matches fairly well to the long

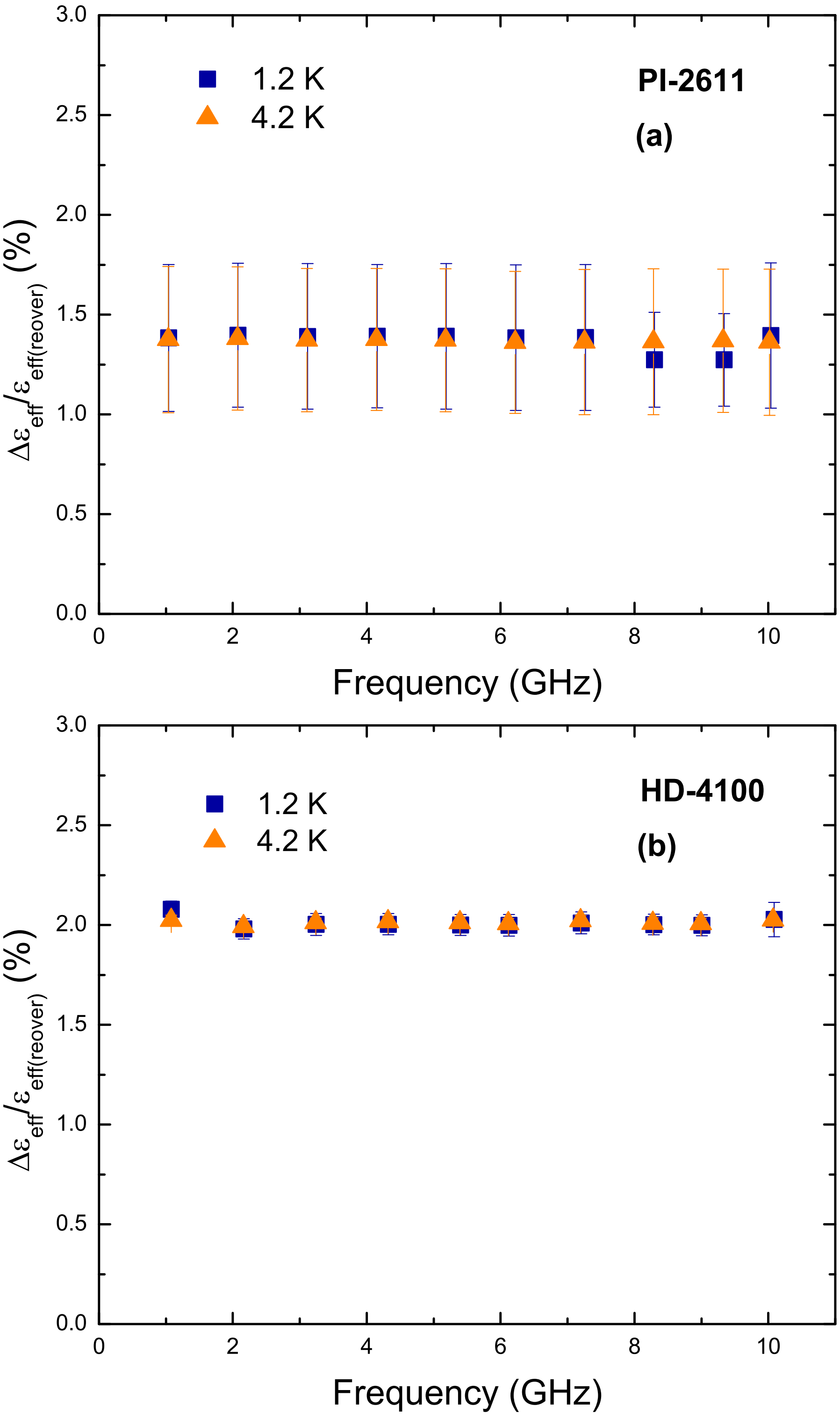

Figure 3.35: Effective dielectric constant change of two types of polyimide after humidity exposure and after recovery bake treatment at 4.2 K and 1.2 K. (a) PI-2611 and (b) HD-4100.

term humidity exposure. HD-4100 remains fairly consistent through the various humidity exposure times with a change of approximately 0.5 %.

3.3.3 Humidity effects on the loss tangent of thin polyimide

The change in loss tangent due to long term humidity-recovery bake treatment was extracted using the relationship shown in equations 3.4 and 3.5.

$$Q_d = \frac{1}{tan\delta}(1 + \frac{1-q}{q\epsilon_r}) \tag{3.4}$$

Q_d is the dielectric loss, $tan\delta$ is the dielectric loss tangent, q is the dielectric filling factor. This filling factor is related to the dielectric constant and also the design geometry. Equation 1.8 allows us to extract the dielectric loss information of the substrate material.

$$tan\delta = tan\delta_{humidity} - tan\delta_{recovery} \tag{3.5}$$

$tan\delta$ is the dielectric loss changes during the humidity and recovery treatment. $tan\delta_{humidity}$ is dielectric loss after the humidity exposure and $tan\delta_{recovery}$ is the dielectric loss after the recovery bake.

The changes in loss tangent (Δtanδ) vs. resonance frequencies at temperatures of 4.2 K and 1.2 K are shown in Figure 3.38 for both PI-2611 and HD-4100. Similarly to the changes in effective dielectric constant, we see greater sensitivity to moisture on the PI-2611 than the HD-4100. At 1.2 K, we do not see significant frequency dependence on the relative change for either film. At temperature of 4.2 K, we note that there is an apparent frequency dependence, we attribute this frequency dependence to conductor loss, therefore we cannot separate dielectric losses in the film due to humidity at 4.2 K.

In the second test we performed, in which we varied the time the samples were exposed to humidity, we extracted the changes in loss tangent as well. The purpose is to determine a saturation point of the dielectric loss. The measurement results at 4.2 K are shown in

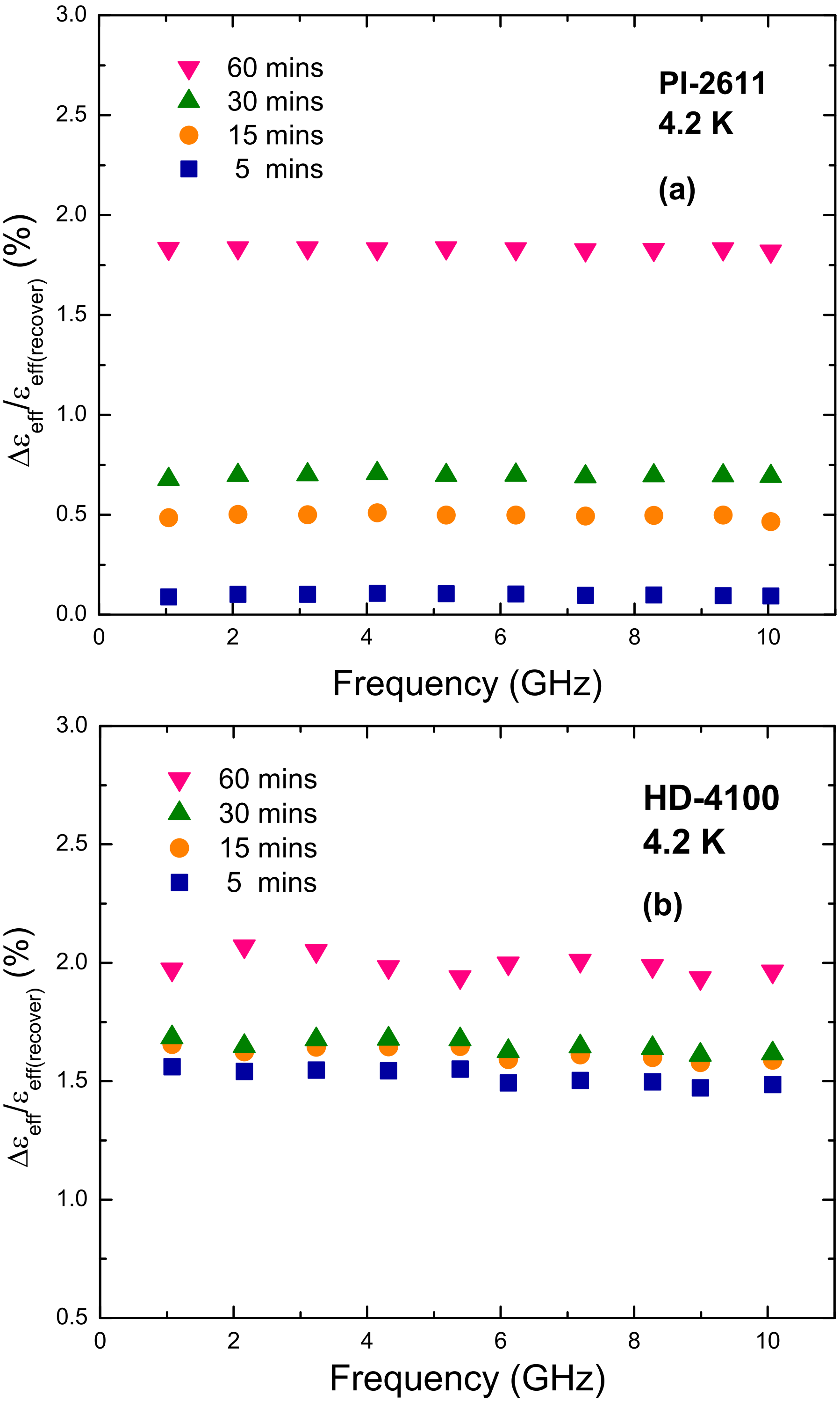

Figure 3.36: Effective dielectric constant change of two types of polyimide after various humidity exposure times, measured at 4.2 K. (a) PI-2611 and (b) HD-4100.

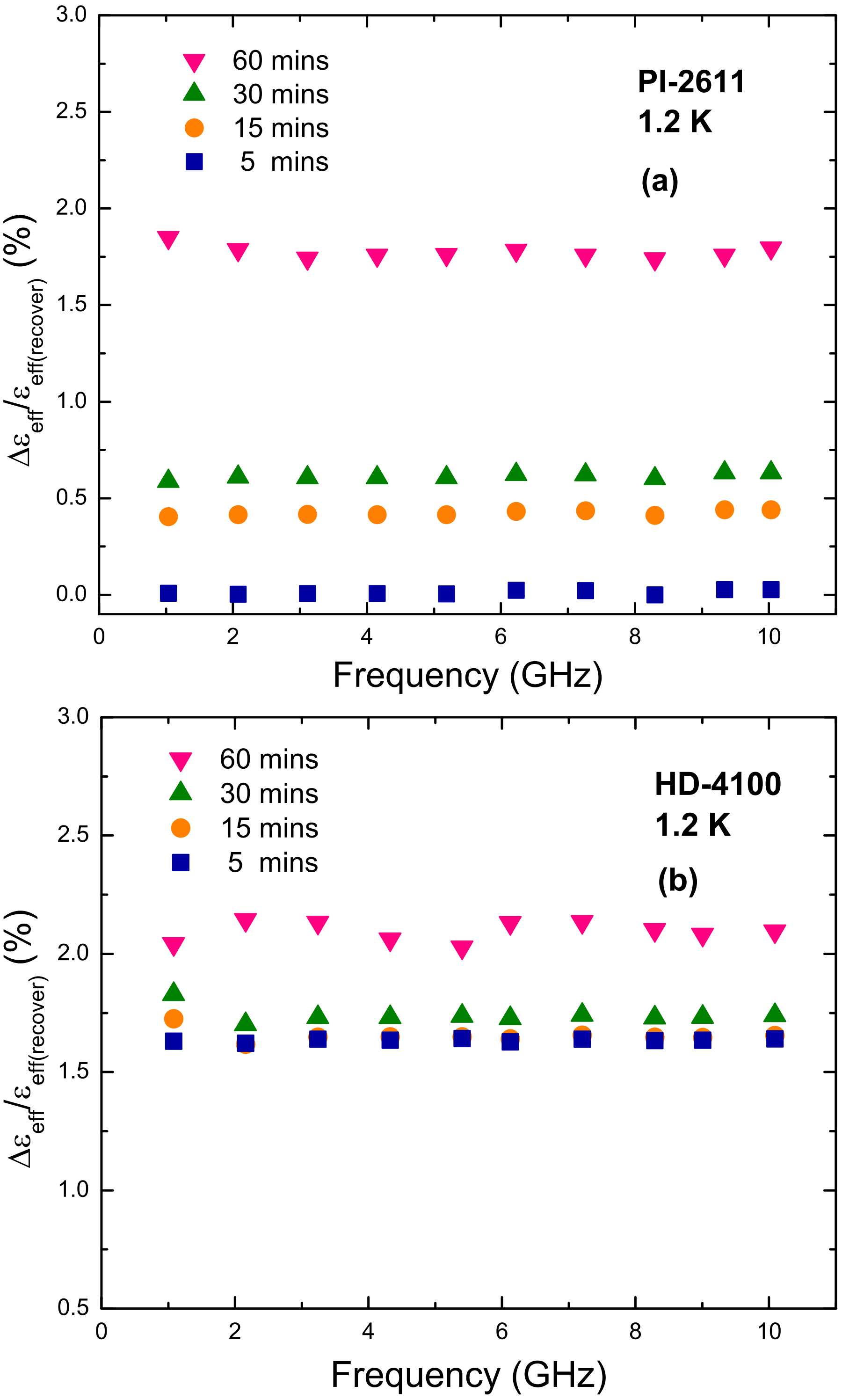

Figure 3.37: Effective dielectric constant change of two types of polyimide after various humidity exposure times, measured at 1.2 K. (a) PI-2611 and (b) HD-4100.

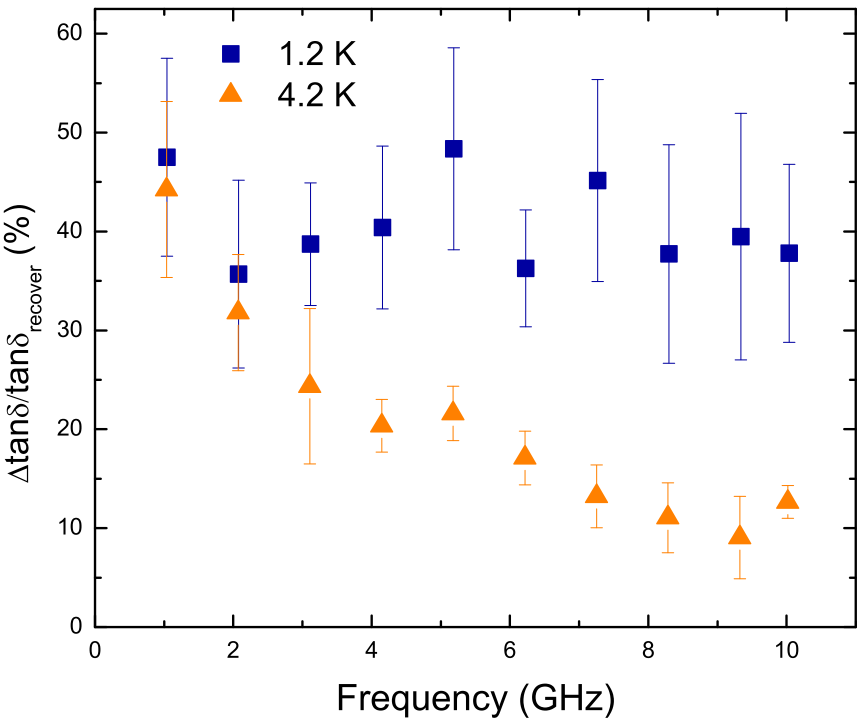

Figure 3.38: PI-2611 loss tangent ($tan\delta$) percentage changes after long term humidity exposure and after recovery bake treatment measured at 4.2 K and 1.2 K.

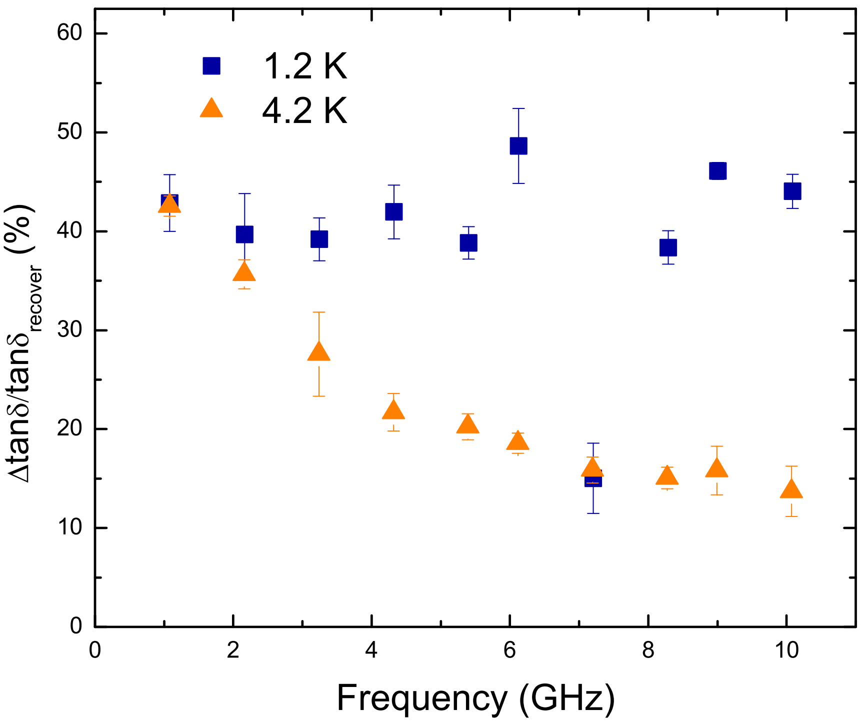

Figure 3.39: HD-4100 loss tangent ($tan\delta$) percentage changes after long term humidity exposure and after recovery bake treatment measured at 4.2 K and 1.2 K.

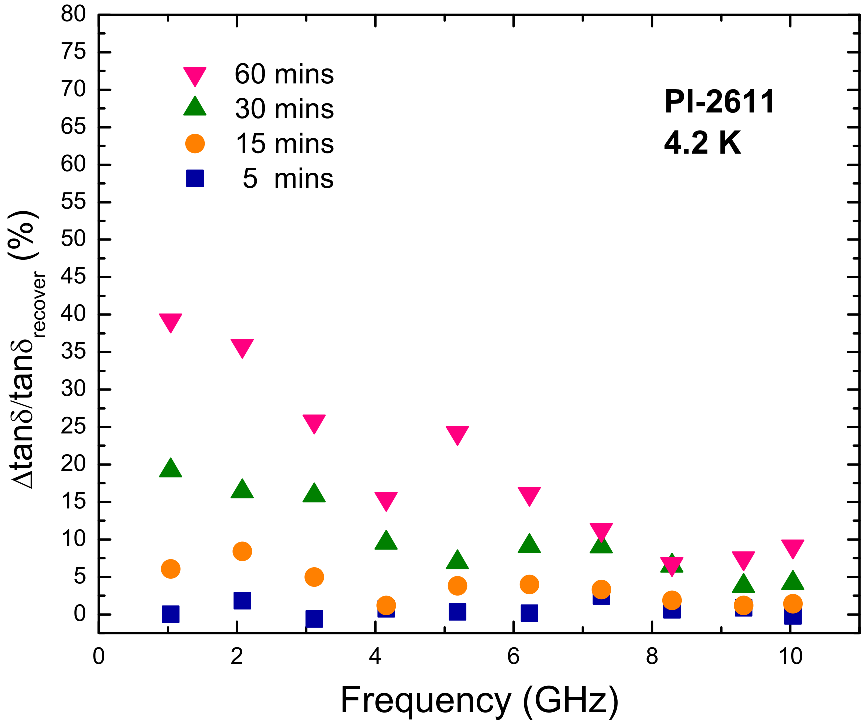

Figure 3.40: PI-2611 loss tangent ($tan\delta$) percentage changes after various humidity exposure times measured at 4.2 K.

Figure 3.40 for PI-2611 and Figure 3.41 for HD-4100. The time-dependent sensitivity to humidity exposure of PI-2611 films is also apparent in these measurements, especially at lower frequencies. Unlike PI-2611, HD-4100 does not show a clear trend. The characterization results at 1.2 K of this test is shown in Figure 3.42 for PI-2611 and Figure 3.42 for HD-4100. Similar to the measurement result at 4.2 K, PI-2611 exhibits more sensitivity to moisture than the HD-4100 film. At a temperature of 1.2 K, both films don't show frequency dependent loss tangent change to varying exposures to humidity. Thus we conclude that at 1.2 K, changes in the loss tangent are significant and a proper bake out of samples is necessary to ensure the optimal microwave performance.

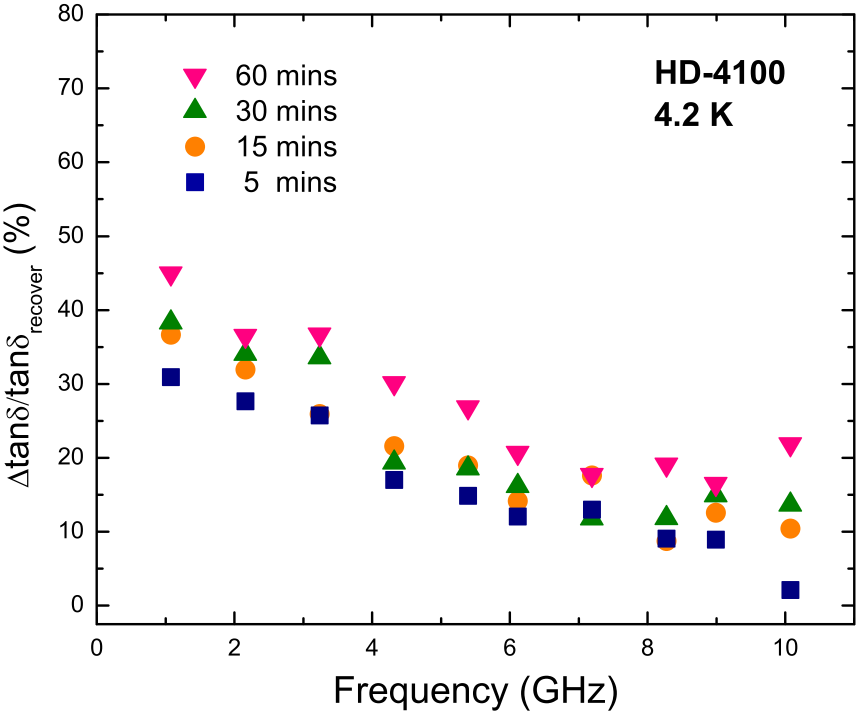

Figure 3.41: HD-4100 loss tangent ($tan\delta$) percentage changes after various humidity exposure times measured at 4.2 K.

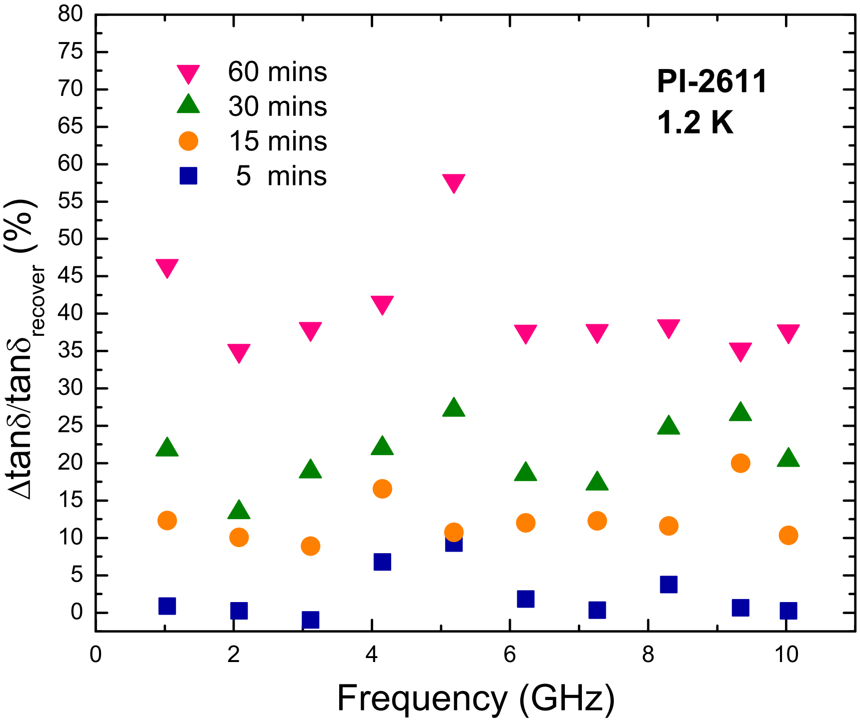

Figure 3.42: PI-2611 loss tangent ($tan\delta$) percentage changes after various humidity exposure times measured at 1.2 K.

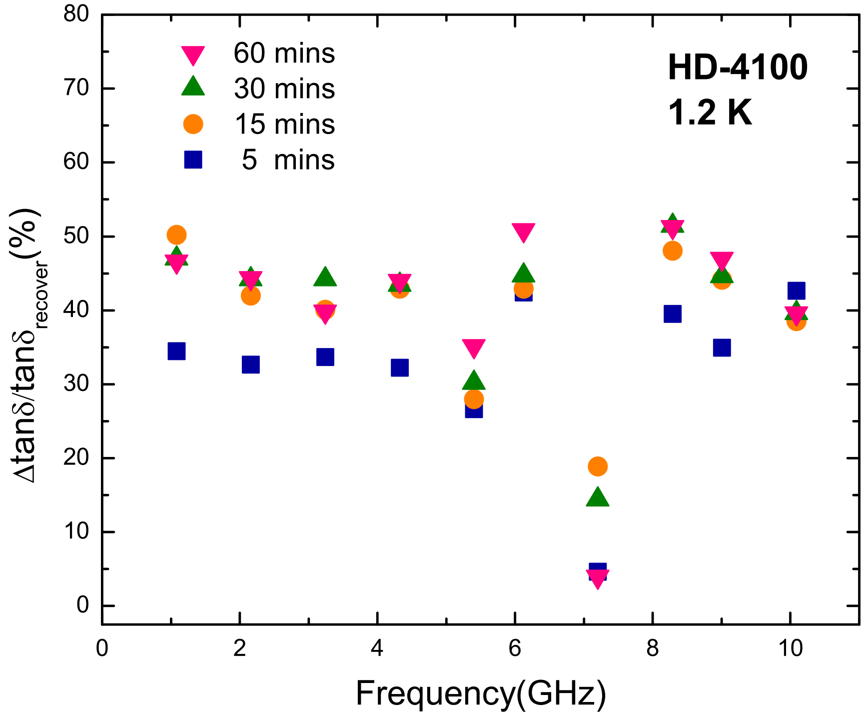

Figure 3.43: HD-4100 loss tangent ($tan\delta$) percentage changes after various humidity exposure times measured at 1.2 K.

Chapter 4

Bilayer and embedded microstrip resonators

In order to improve adhesion or enhance mechanical reliability, superconducting bilayer structure has been widely used [79–81]. When we combine normal and superconductor metal layers together, proximity effects begin to determine the behavior of this structure, such as realizing superconductivity and corresponding coherence length in the normal metal layer [82]. Several groups have reported a lot of information about the normal metal coherence length in these bilayer structures [7, 82–84].

We first describe our investigation of Ti/Nb structures. Ti is a commonly used material to improve the adhesion, therefore we explore its use between superconducting Nb and polyimide. Some research shows that the deposition process of Ti layer can effectively reduce the oxygen level in the deposition chamber by gettering and thereby improve the quality of the Nb layer [85]. This type of bi-layer (normal-superconductor) usually exhibits proximity effect leading to the whole structure exhibiting superconductivity, especially when the normal metal is thin and has good contact with the superconductor [7]. Even though this bilayer can realize superconductivity, the thin normal metal layer is still expected to introduce extra RF loss. In order to quantify the extra conductor loss caused by this thin Ti adhesion layer, we built a set of resonators with different thickness of Ti underlayers, such as 10 nm and 50 nm. The resonator characterization result provides the loss changes over a wide frequency range (2-20 GHz) at various cryogenic temperatures. From these results, we determined the conductor loss changes coming from different thicknesses of the Ti layer.

M. S. Pambianchi, et al., reported the characterization result of conductor (Cu/Nb) loss at 11.7 GHz [86]. Though, they only provided the conductor loss information at a fixed frequency, which was limited by their measurement setup. In this work, we characterized this type of bilayer structure using our superconducting flexible resonator. We also investigated Nb/Cu structure, since Cu can enhance the mechanical reliability [87]. We experimentally controlled our Nb and Nb/Cu interface to be the same; the only variable parameter in this series of sample is the thickness of Cu. The Cu thickness in this work includes 20 nm, 50 nm, 100 nm and 200 nm. The result provides the conductor loss of this superconducting-normal bilayer structure over a wide frequency range. We also provide the surface resistance value of this series of Nb/Cu resonators [88].

Furthermore, we investigated polyimide-based multi-layer structures, which is in the form of embedded microstrip resonators in this work. We successfully built fully transitioned superconducting embedded microstrip resonator. We found that an Al/Nb/Al sandwich structure efficiently protects the Nb from being degraded during the top layer polyimide curing process. The detail measurement results shown in later sections.

4.1 Conductor loss characterization of superconducting-normal metal resonator on polyimide at cryogenic temperatures

4.1.1 Characterization of the impact of Ti adhesion layer on conductor losses

The Nb layer in this study was $\sim 0.25\ \mu$m. A cross section of these resonators is shown in Figure 4.1. We measured the sheet resistance changes of the thin Ti film on SiO_2 die along with the temperature decrease to helping analyze the Ti layer effect on our superconducting resonators. This thin Ti layer was electron beam thermally evaporated on to a SiO_2 die, which is the same deposition process as was used for depositing our Ti layer beneath the Nb layer on polyimide films. The measurement results are shown in Figure 4.2. The reduction of resistance with temperature is easily observed. Also, the difference in shape is assumed to be due to enhanced film coverage for the 50 nm thick case. To keep the Nb quality as consistent as possible, we deposited the same Ti thickness on both signal and ground plane before the Nb deposition. In this study, we used a 5 cm long resonator design, which will show the first harmonic resonant frequency at approximately 2 GHz.

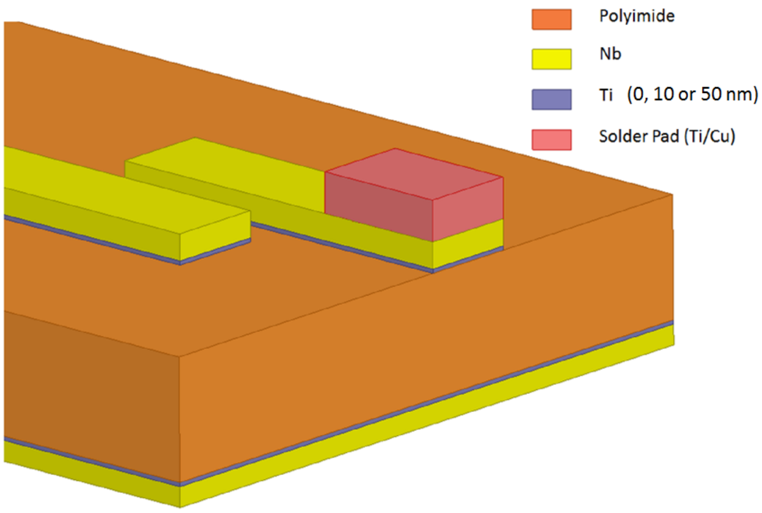

Figure 4.1: Cross section of thin film (PI-2611) superconducting resonator for different Ti underlayer thickness.

For the series of resonators with different Ti thickness as under-layer, we characterized each at temperature steps including 4.2 K, 3.6 K, 3 K and 1.2 K. Since $1/Q \propto$ R(loss), we plot the quality factor measurement results as $1/Q$ vs. resonance frequencies, as shown in Figure 4.3. Each of the Q-factor results is an average of 10 measurements, which takes into consideration the temperature drift in the cryostat.

From Figure 4.3, we can clearly see the sample with the thickest Ti (50 nm) underlayer shows the lowest Q value and the sample without Ti layer shows the highest Q value at all measurement temperatures. This indicates that the Ti underlayer does indeed cause extra conductor loss and this loss increases with increase of Ti layer thickness. This loss is not only dependent on the thickness of the normal metal, but also depends on the measurement temperature. This conductor loss decreases when the measurement temperature decreases. At 1.2 K, the Q value of all three samples shows a comparable result, which indicates the Ti layer doesn't contribute significant conductor loss at this temperature. This can be explained by, at this temperature, the number of unpaired electrons in the Nb layer is reduced and leads to a move proximitized and longer coherence length in the normal metal layer [89]. So, the overall number of unpaired electrons in this bilayer structure reaches the lowest level

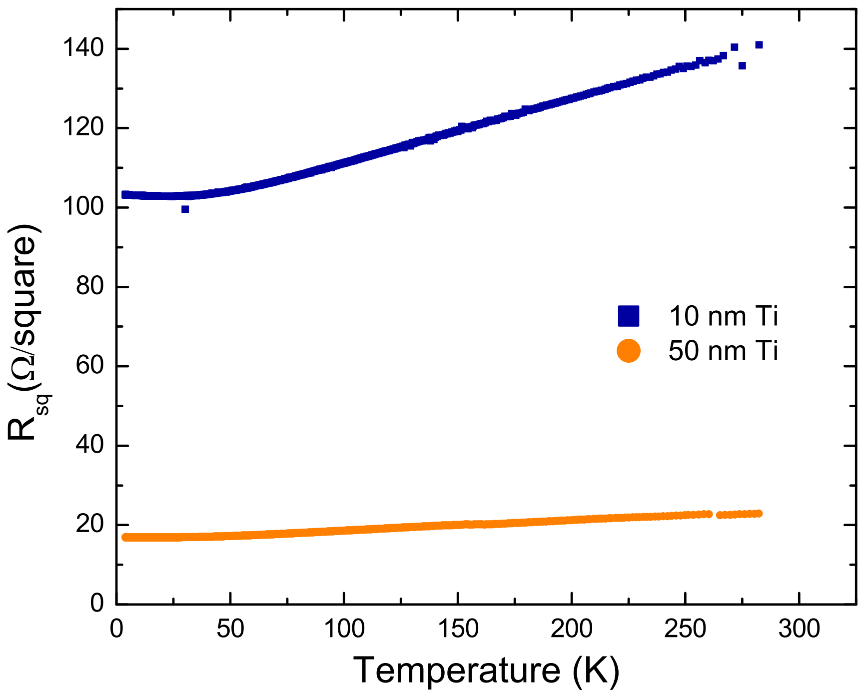

Figure 4.2: Sheet resistance vs. temperature of 10 nm and 50 nm Ti thin films on SiO_2.

compared to other temperatures, resulting in lower conductor loss and higher Q. Also shown in Figure 4.3 is a simulation result for $\tan\delta = 0$, therefore we conclude that for samples at 1.2 K, the remaing loss is related to the non-zero loss in the dielectric.

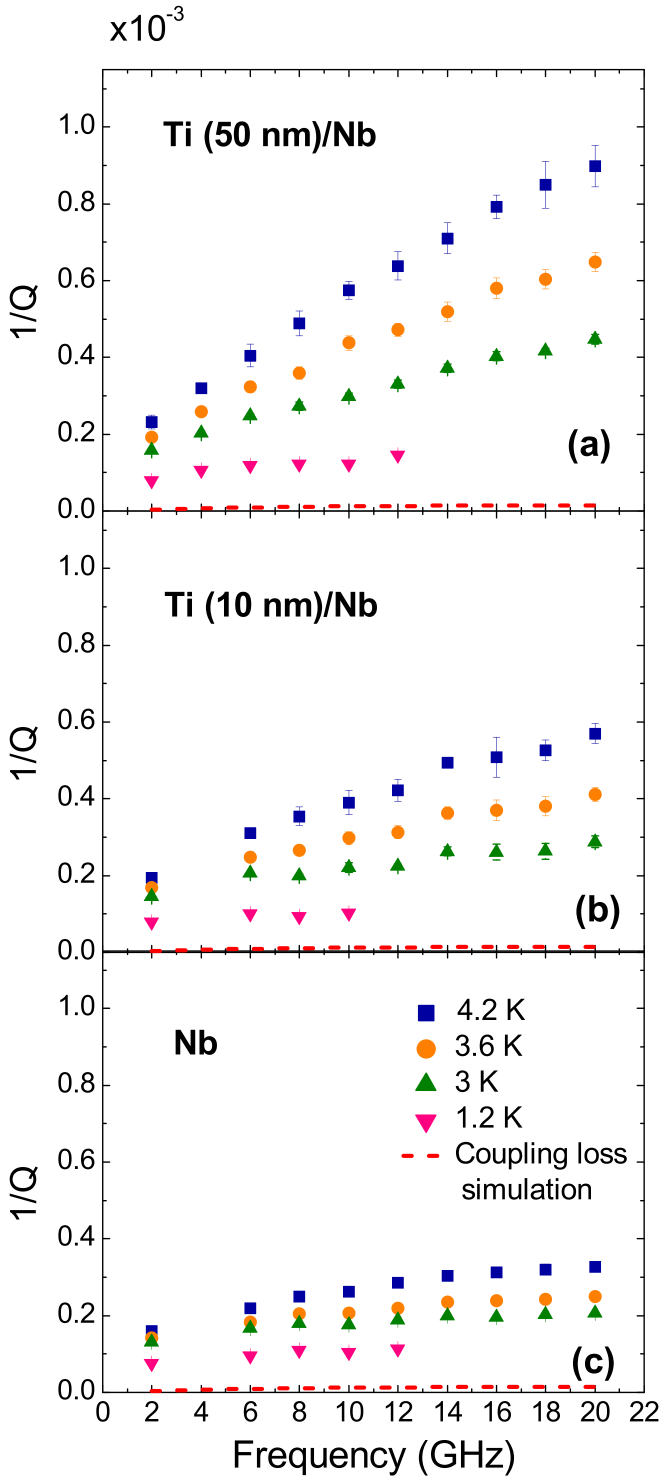

Figure 4.3: $1/Q$ vs. resonant frequencies at various temperatures. Results for conductor stacks of (a) Ti(50 nm)/Nb, (b) Ti(10 nm)/Nb, (c) Nb. Nb thickness is 250 nm in all cases.

We also calculated the surface resistance of this series of Ti/Nb resonators. To get Q_{unload}, we can use:

$$\frac{1}{Q_{unload}} = \frac{1}{Q} - \frac{1}{Q_{coupling}} \tag{4.1}$$

Here, Q_{unload} is unloaded quality factor, Q is the measured quality factor (loaded Q) and $Q_{coupling}$ is the coupling Q. We determined this coupling Q value by using ADS simulator.

In order to characterize the surface resistance of these resonators, we can calculate R_s using:

$$R_s = \frac{\Gamma}{Q_{unload}} \tag{4.2}$$

where Γ is a geometry-related parameter and Q_{unload} is the unloaded quality factor [90]. The calculation of the geometry parameter is from:

$$\begin{aligned} w' &= w + \frac{t}{\pi}[ln(\frac{2h}{t} + 1)] \\ B &= 1 - \frac{w'^2}{16h^2} \\ C &= \frac{1}{h}(1 - \frac{t}{w'\pi}) \\ D &= \frac{2}{w'}[1 + \frac{1}{\pi}ln(\frac{2h}{t})] \\ \Gamma &= \frac{4\pi^2 Z_0}{\lambda_g B(2C + D)} \end{aligned} \tag{4.3}$$

where w is the width of the microstrip resonator line, h is the thickness of the substrate, t is the thickness of the conductor, Z_0 is the characteristic impedance of the microstrip resonator and λ_g is the guided wavelength.

The results for different thicknesses of Ti layers beneath the Nb resonators at different temperatures are shown in Figure 4.4 We can clearly see that the surface resistance is reduced as the temperature is decreased from 4.2 K to 1.2 K. Since the un-paired electrons contribute to the surface resistance, this reduction in the conductor loss can be attributed to a decrease of the quasi-particles in the Nb and increased thickness of the proximitized Ti layer. Therefore, the additional surface resistance seen in the thicker Ti samples can be attributed to the non-proximitized electrons in the Ti layer.

4.1.2 Characterization of the impact of Cu cladding layer on conductor losses

In order to reduce degradation of the Nb quality due to handling, which can result in micro-cracks, we investigated normal metal (Cu) cladding layers on Nb. This bi-layer structure has been shown reduce the degradation and enhance the mechanical reliability. Here, our work is focused on investigating the extra conductor loss caused by the normal metal for our flexible polyimide resonators. The design we used in this study consisted of a ∼25 cm long resonator. The assembled sample is shown in Figure 4.5.

We fabricated a series of Nb resonator structures with different thickness of Cu cladding layers on thin (20 μm) polyimide (PI-2611) substrates. We used a single Nb deposition run for all samples in order to prevent Nb quality variation due to different sputtering runs. Our signal line metal deposition process flow in Figure 4.6 was followed. First, we sputtered a ∼0.25 μm thick Nb film followed by electron-beam physical vapor deposition to yield a 20 nm Cu layer. Then, this wafer was removed from the deposition chamber and stored in a N_2 environment. After the second pump down, we performed a one minute ion clean to remove any oxidized Cu followed by a second Cu deposition process in order to yield an additional 30 nm Cu layer (50 nm total). We removed the second wafer, which had a 50 nm Cu thickness on top of Nb film on this wafer. This deposition process was repeated to deposit another 50 nm and 100 nm Cu layer, in sequence. Eventually, we obtained four wafers with the same Nb but different Cu layer, thicknesses of: 20 nm, 50 nm, 100 nm and 200 nm. The benefit of depositing the metal this way is we can have an identical Nb layer in order to avoid the Nb quality variation from sample to sample, and have an identical Nb/Cu interface as well. The same Nb layer and Nb/Cu interface should exhibit an almost identical superconductivity proximity effect, which can help us evaluate the loss difference only coming from the Cu

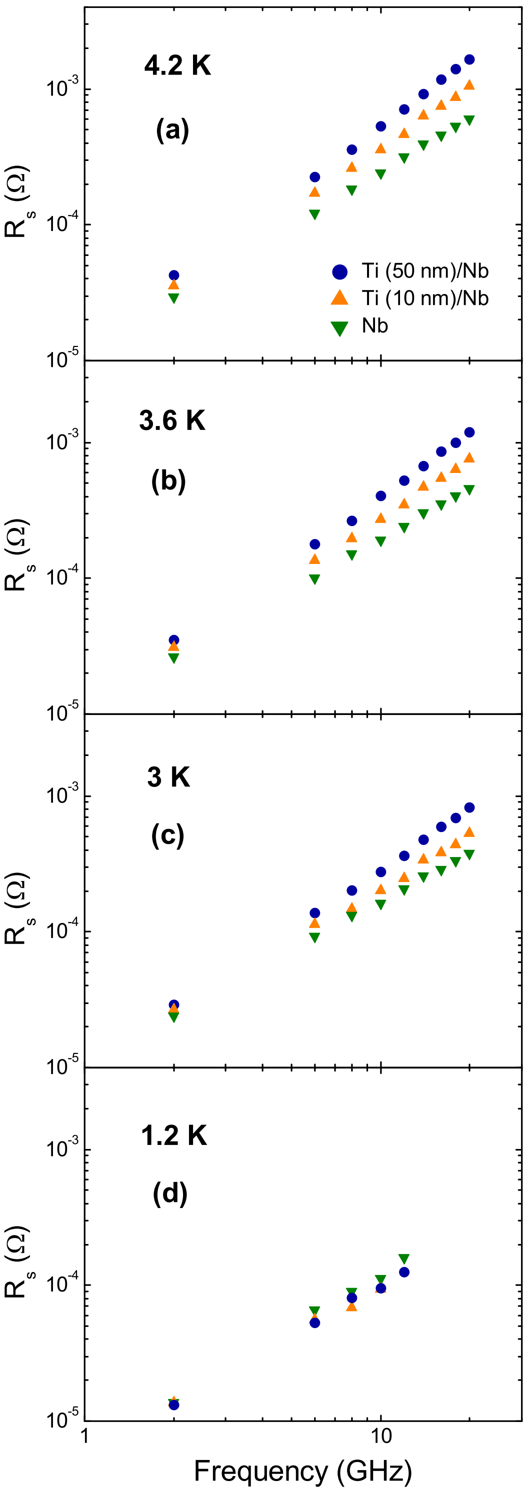

Figure 4.4: Surface resistance of Ti (0, 10 and 50 nm)/Nb resonators at (a) 4.2 K (b) 3.6 K (c) 3 K and (d) 1.2 K.

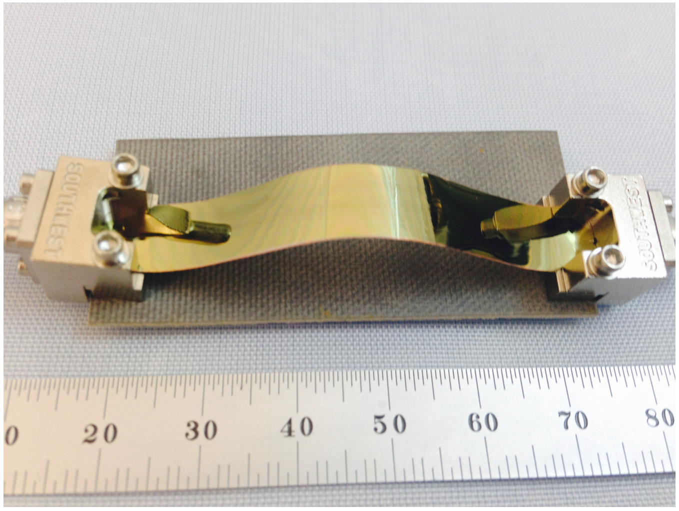

Figure 4.5: Assembled 5×11 cm long resonator on PI-2611 film.

layer with different thickness. In order to prevent Cu from oxidation during any further processing, we put all four wafers back into the deposition chamber and deposited a thin (10 nm) Au layer on all four wafers after a one minute ion clean process. Then, all of the wafers under went the same UBM layer deposition, film release process and ground plane Nb deposition process. We deposited the same Nb ground plane layer on the back side at the same time for all the samples to prevent differences caused by the ground plane. The information for films on witness SiO_2 of these Nb/Cu(20 nm, 50 nm, 100 nm and 200 nm) samples is shown in Table 4.1.

Based on the theory of proximity effect, thicker normal metal may cause suppression of superconductivity. The critical temperature results of Nb/Cu(20 nm, 50 nm, 100 nm and 200 nm) on SiO_2 die are shown in Figure 4.7. All of the samples have a similar critical temperature, which was approximately 9.1 K. This doesn't show obvious superconductivity suppression for these four Nb/Cu combination cases.

We characterized the microwave performance of these samples in a pulse tube based cryostat. In order to reduce the effect of humidity, we performed a dehydration bake in a vacuum oven at 90 °C for two hours before measurement. Our characterization temperature range is from 4.2 K to 1.2 K.

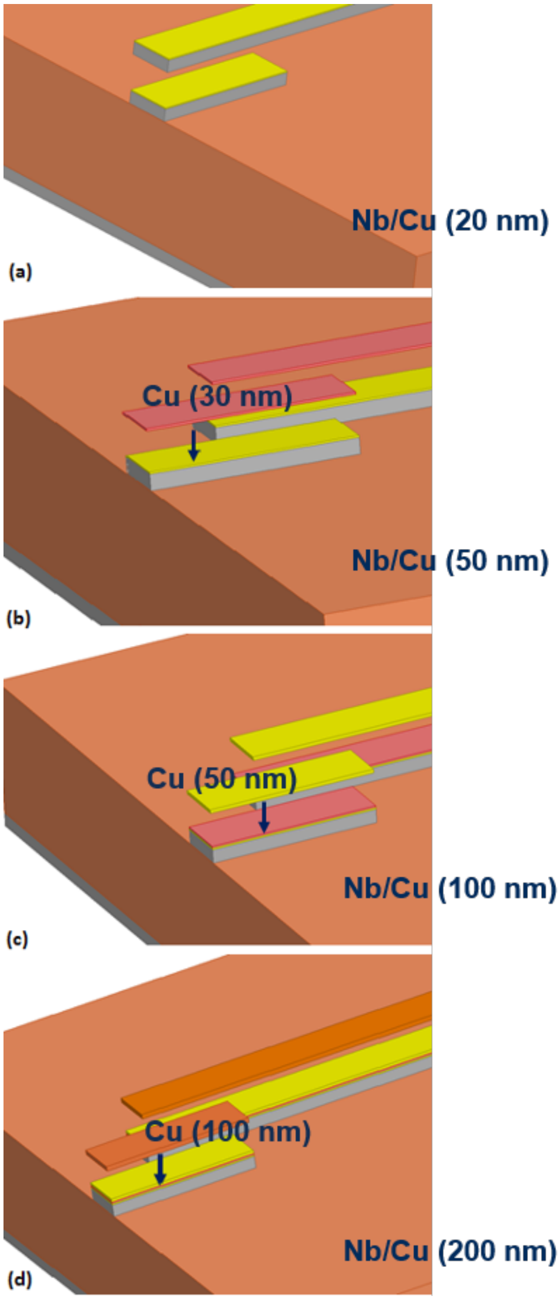

Figure 4.6: Metal deposition flow of Cu layer of Nb/Cu/Au series of resonators. (a) 20 nm Cu on top of the Nb layer, (b) additional 30 nm Cu on top of the Cu(20 nm)/Nb, (c) additional 50 nm Cu on top of the Cu(50 nm)/Nb, (c) additional 100 nm Cu on top of the Cu(100 nm)/Nb.

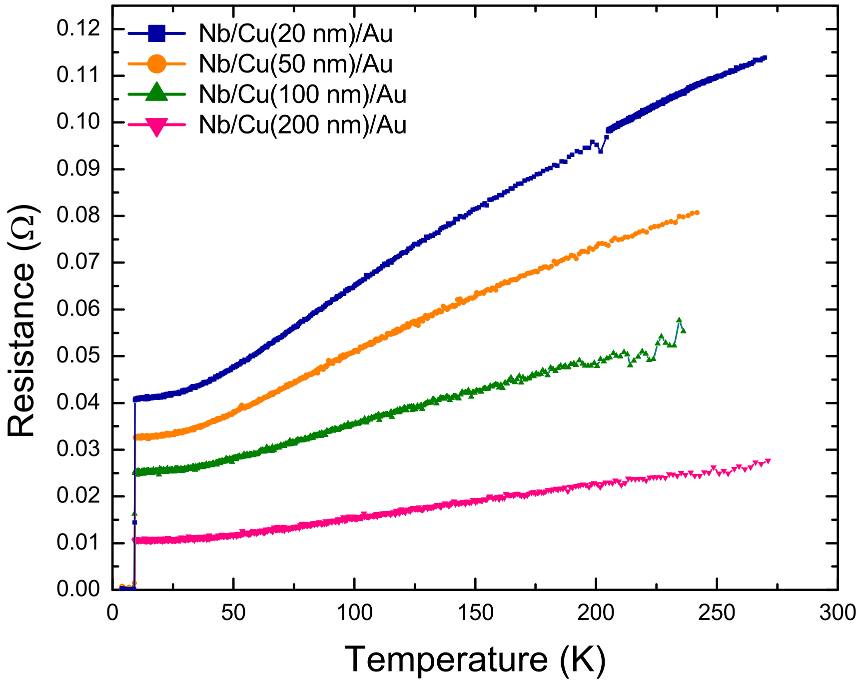

Figure 4.7: Critical temperature of Nb/Cu(20 nm, 50 nm, 100 nm or 200 nm)/Au film on SiO_2 witness die.

Table 4.1: Resistance information of Nb/Cu(20 nm, 50 nm, 100 nm or 200 nm) films deposited on SiO_2 die) at room temperature and before transition temperature.

Cu thickness (nm)	R_{sq} (Ω/□)@ RT	R (Ω)@ RT	R (Ω)@ right before transiton
20	0.897	0.134	0.0406
50	0.691	0.089	0.0325
100	0.447	0.0594	0.02497
200	0.205	0.0299	0.0104

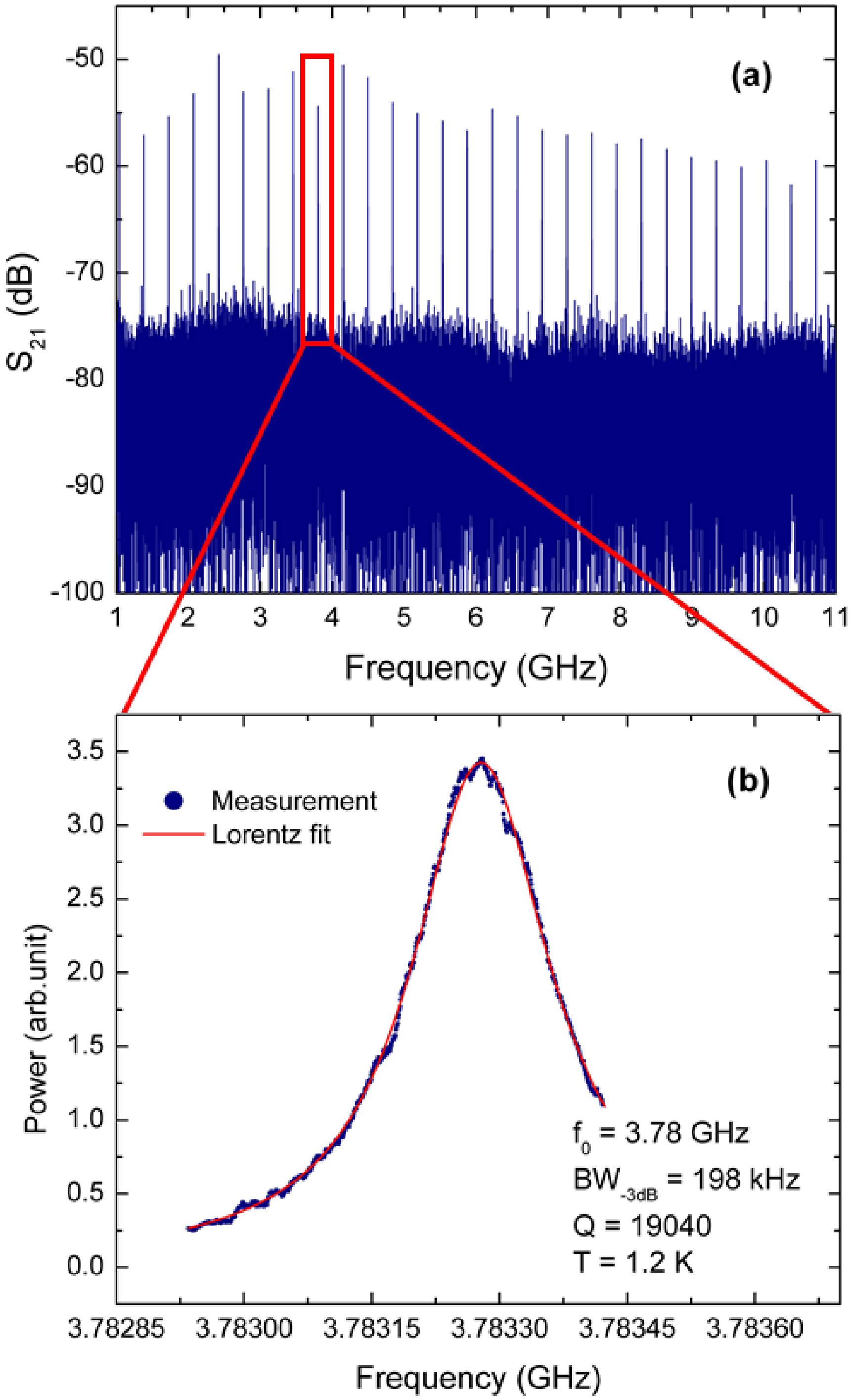

Figure 4.8: S_{21} measurement results of a 27 cm long Nb/Cu(20 nm)/Au(10 nm) resonator measured at 1.2 K. (a) Broadband view of the 3rd through 31st harmonics. (b) Zoomed-in view of the 11th harmonic, superimposed with the best-fit Lorentzian function (used to calculate quality factor Q).

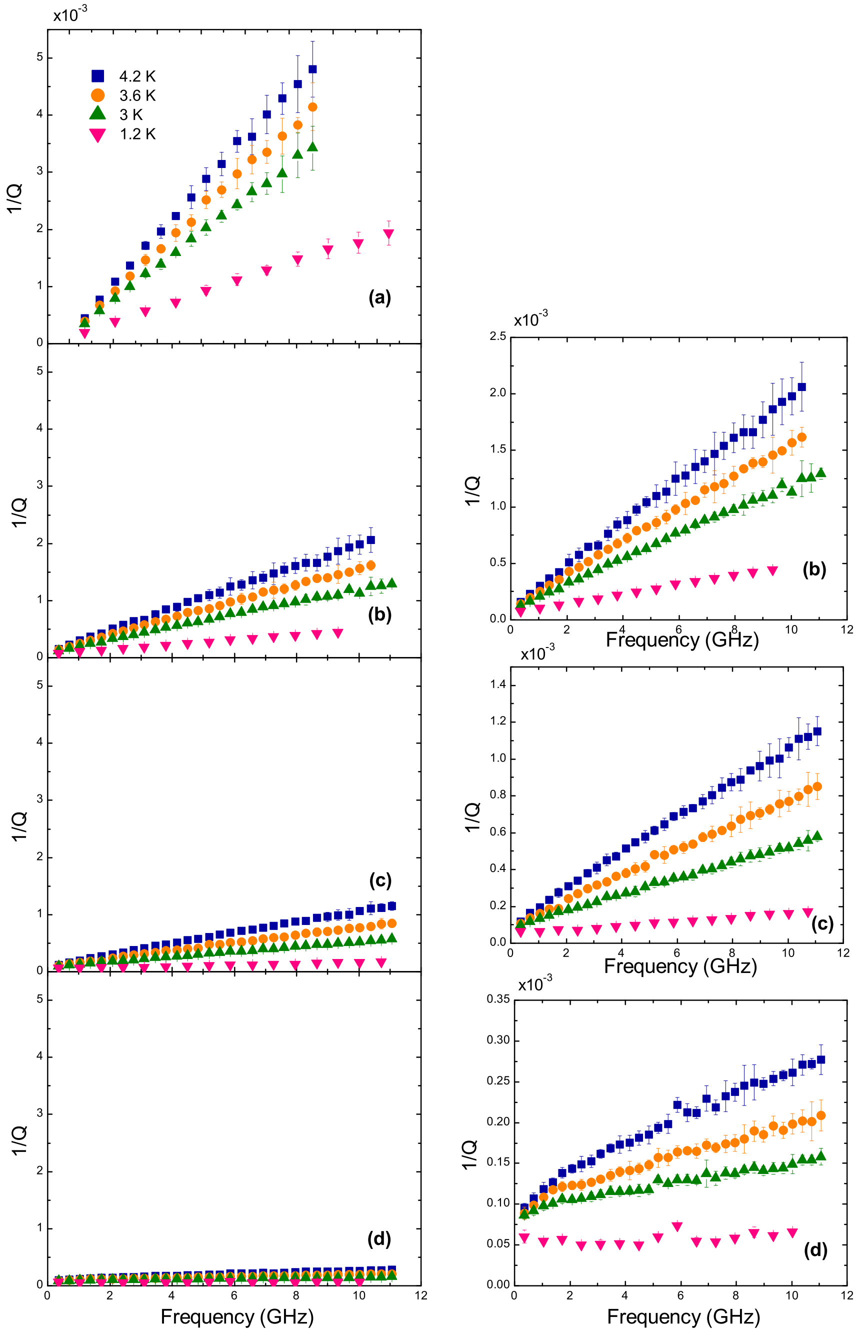

Figure 4.9: $1/Q$ vs. resonant frequencies at various temperatures. (a) Nb/Cu(200 nm) (b) Nb/Cu(100 nm) (c) Nb/Cu(50 nm) (d) Nb/Cu(20 nm). Side plots are close-up view of the $1/Q$ vs. resonant frequency plot of Nb/Cu(100, 50 and 20 nm) samples.

The S_{21} measurement result of the Nb/Cu(20 nm) sample at 1.2 K is shown in Figure 4.8(a). In this Figure, we also provide one of the representative Lorentz fit result for one of the resonant harmonic shown as Figure 4.8(b). The summarized Q-factor results of this series of Nb/Cu resonators is shown in Figure 4.9 at various temperatures. We plot $1/Q$ vs. resonant frequency for each of the Cu thicknesses at 4.2 K, 3.6 K, 3 K and 1.2 K. In order to compare the different samples, we set the scale to be the same for these plots. To observe the temperature impact on each of the sample with different Cu thickness clearly, the side plot shows an enlarged plot for the 50 nm, 100 nm and 200 nm cases at each of the temperatures. Corresponding to the results in Figure 4.9, all of the samples show a significant reduction of the conductor loss as measurement temperature is decreased. Furthermore, all of the Nb/Cu samples followed the rule of: $1/Q \times f_0 =$ constant, similar to Nb resonators.

Based on the proximity effect, the Cu region begins to show superconductivity as the measurement temperature decreases, leading to lower conductor loss. Since all of our samples go through the Nb/Cu(20 nm) deposition process at the same time, we yield four samples with the same superconductor (Nb) layer and the same superconductor-normal metal (Cu) interface. This allows us to quantify the proximity effect in these samples with different Cu thickness.

In Figure 4.10 and Figure 4.11, we summarize the slope and intercept information from the $1/Q$ vs. resonant frequency plots. From Figure 4.10, we can clearly see these slopes exhibit an exponential relationship with the thickness of the Cu cladding layer. We can assume the proximity effect on all of these samples are similar at each of the measurement temperatures, since the Nb layer and Nb/Cu interface are all identical. Then we can explain the slope difference is caused by differences due to Cu thickness. The more free electrons remaining in the Cu layer, the more conductor loss will be observed at all the measurement temperatures [86].

From Figure 4.11, we can clearly see that when the Cu thickness is below 50 nm, the samples yield almost the same intercept value. This indicates that when the Cu layer is less

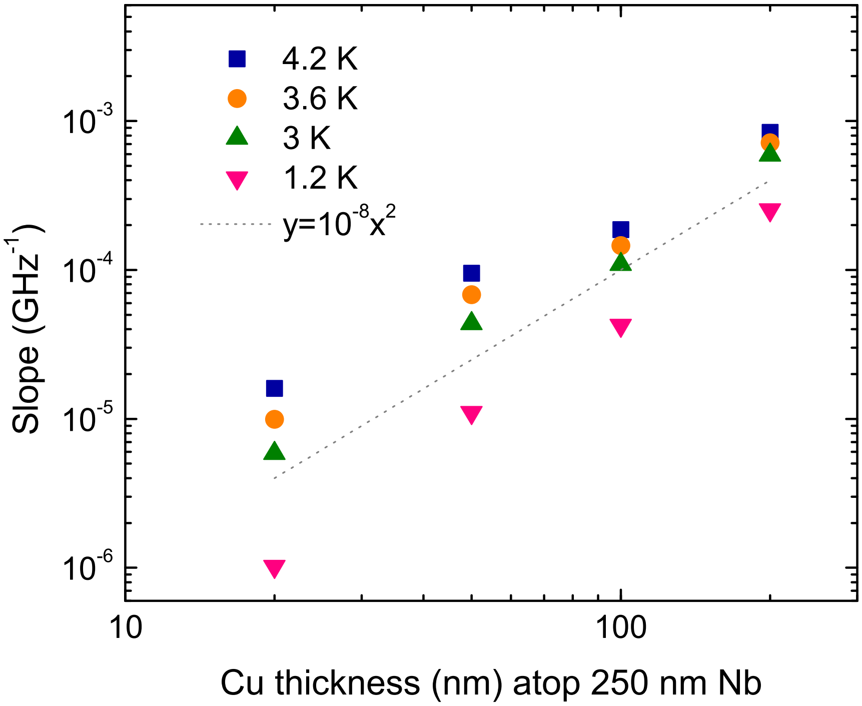

Figure 4.10: Slope of $1/Q$ vs. resonance frequencies plots of Nb/Cu(20, 50, 100 and 200 nm) resonators at 4.2, 3.6, 3, and 1.2 K. The data at each temperature approximately follow a square law, as is evidenced by their having slopes on this log-log plot parallel to the illustrated square-law function.

than 50 nm, the dielectric loss still dominates the overall loss, instead of the conductor loss. But, when the Cu thickness is greater than 100 nm, we observe a higher intercept value, and the Nb/Cu(200 nm) sample shows the highest intercept value. This indicate that when we have too thick of Cu capping layer, the conductor loss, as opposed to the dielectric.

We analyzed the RF Rs of the set of Nb/Cu(20, 50, 100, and 200 nm) resonators by using the same methodology as the Ti/Nb series of resonators. The results for different thicknesses of Cu on the Nb resonators at different temperatures are shown in Figure 4.12. We observed the same trend as the Ti/Nb samples, which is that surface resistance decreases as temperature decreases. At 1.2 K, which is far below the Nb transition temperature (Tc 9.1 K), the un-paired electron density in the Nb layer is significantly lower, such that it can be ignored. Therefore the surface resistance difference should solely be due to the top Cu cladding layer. Since we have the same Nb layer and Nb/Cu interface, the coherence length

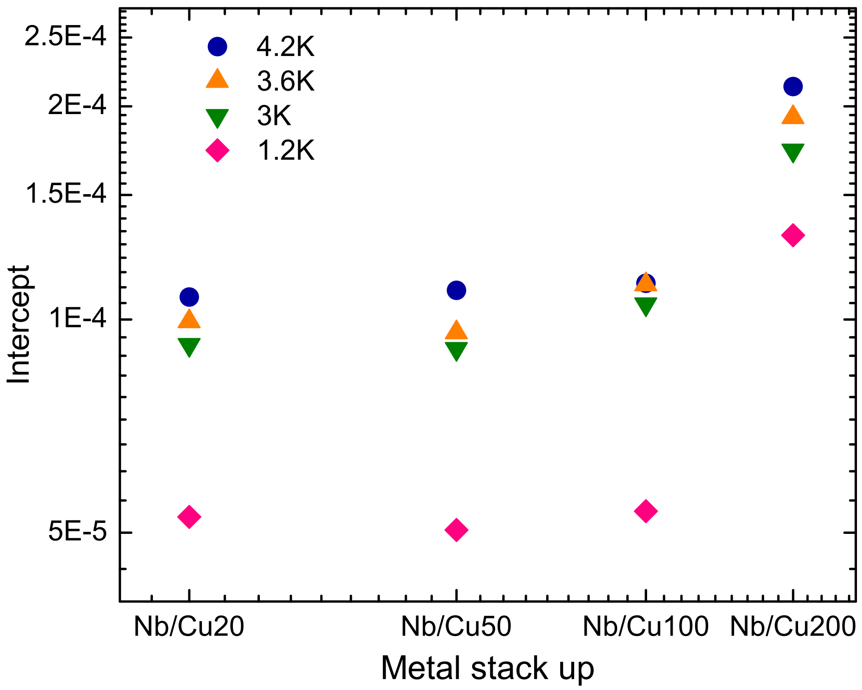

Figure 4.11: Intercept summary from $1/Q$ vs. resonance frequencies plots of Nb/Cu(20 nm, 50 nm, 100 nm or 200 nm) resonators at various temperatures.

in the Cu layer of all of the four samples at this temperature should be the same. Therefore, the additional surface resistance seen in the thicker Cu samples can be attributed to the non-proximitized electrons in the Cu layer.

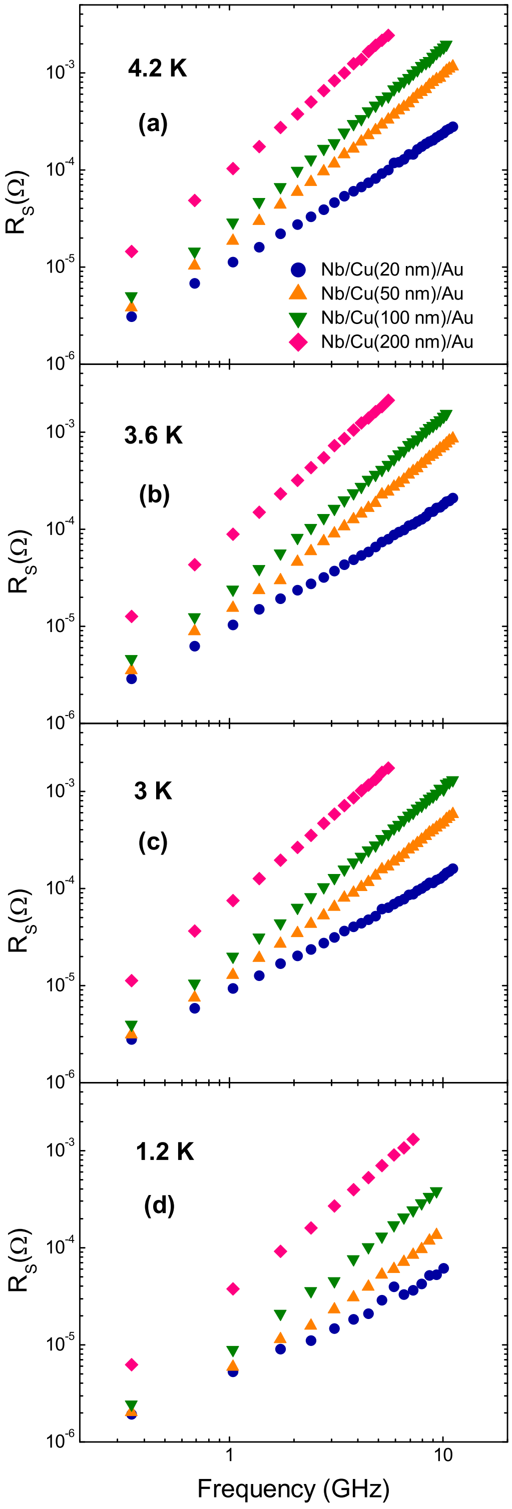

Figure 4.12: Residual surface resistance of Nb/Cu(20 nm, 50 nm, 100 nm or 200 nm) resonators at (a) 4.2 K, (b) 3.6 K, (c) 3 K and (d) 1.2 K.

4.2 Embedded microstrip resonator on polyimide at cryogenic temperatures

4.2.1 Nb embedded microstrip resonator on polyimide at cryogenic temperatures

Polyimide is widely used in multilayer structures as a thermal insulation layer, especially at cryogenic temperatures [91–93]. There are several groups who have reported multi-layer flexible circuits based-on polyimide dielectric and several of them focus on cryogenic applications, such as a filter [94]. But none have reported on superconducting flexible multi-layer microwave structures.

We have successfully fabricated and characterized superconducting embedded microstrip transmission line structures, which show the potential to build more complex multi-layer structures. In this work, 25 cm long Nb embedded microstrip resonators were built and characterized at cryogenic temperatures (below 4.2 K). We used a Kapton stencil to define the UBM connection pad area when we spin on the top layer polyimide. By keeping the spin speed the same as the bottom layer and cured at 350°C, it yields a top polyimide (PI-2611) layer of $\sim$10 μm thick after a curing process. The bottom layer remained $\sim$20 μm (two spin-on process, cured at 350°C N_2 oven after each of the spin-on process) thick as previous resonators. The cross section of this embedded sample, as well as the non-embedded version, are shown in Figure 4.13. The quality factor of non-embedded and embedded resonator measurement results at different temperatures are shown in Figure 4.14 and 4.15 respectively. For comparison, we plot Q-factor measurement results of the embedded and non-embedded Nb resonator on PI-2611 together, which is shown in Figure 4.16. From the $1/Q$ vs. resonance frequencies plot, we find the embedded version shows more loss (higher slope) at both 4.2 K and 1.2 K than the non-embedded version. For the 1.2 K case, we observe that the non-embedded sample shows the "no-BCS" flat-line shape, while the embedded sample shows BCS-related losses. There are two possible reasons that may cause the lower Q-factor in these embedded resonators. The first possible reason is the low

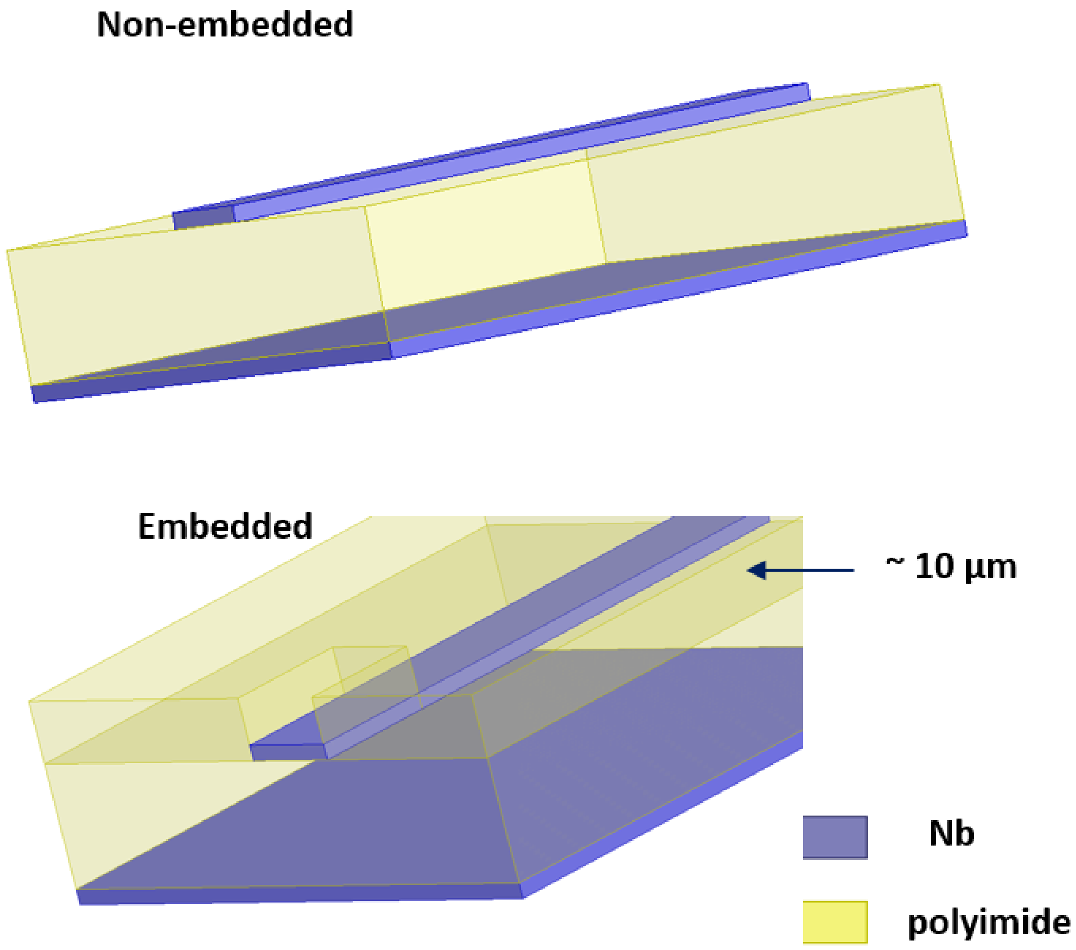

Figure 4.13: Cross section of embedded and non-embedded Nb resonators on thin film polyimide.

temperature (225°C) cured polyimide film may have a different loss tangent value compare to the normal temperature (350°C) cured films. Another possibility is that the Nb quality degraded during the top polyimide curing process. Here, we suspect the reason for low Q values in the embedded resonator is the Nb degradation. We will show results that this case in a later section.

Similar tests were also carried out on a photo-definable polyimide (HD-4100). We used a 25 cm long meander resonator to do this test, as well. For comparison, the bottom layer polyimide was cured (350°C) at the same time for both embedded and non-embedded versions. All of the Nb signal traces were deposited at the same time, as well as the bottom

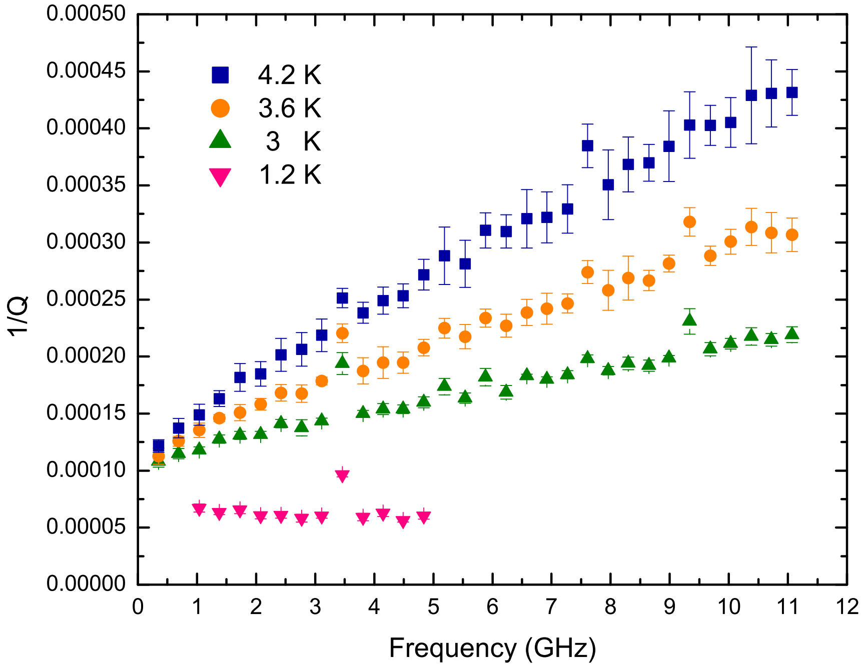

Figure 4.14: $1/Q$ vs. resonance frequencies of Nb non-embedded microstrip resonator on PI-2611 at various temperatures.

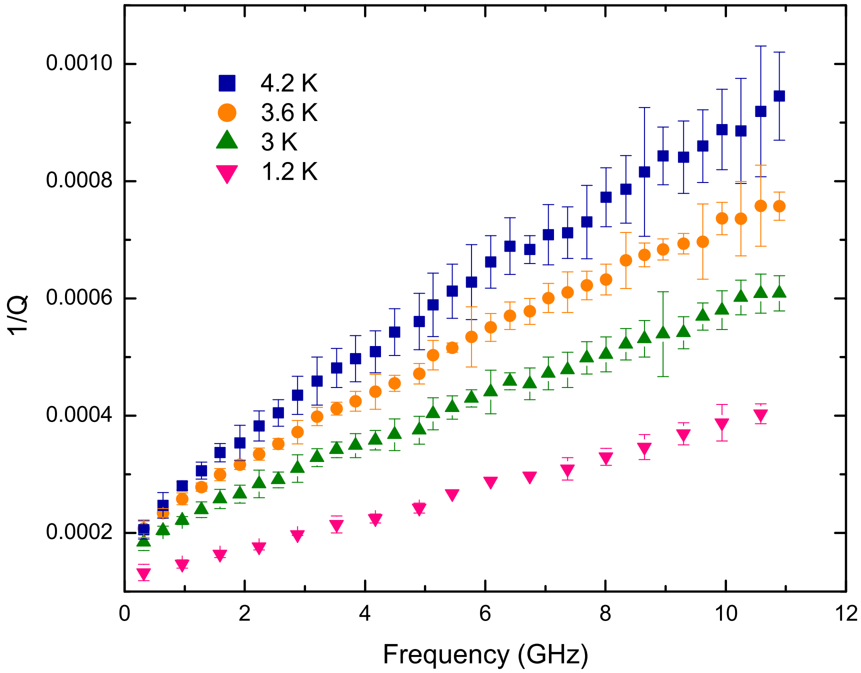

Figure 4.15: $1/Q$ vs. resonance frequencies of Nb embedded microstrip resonator on PI-2611 at various temperatures.

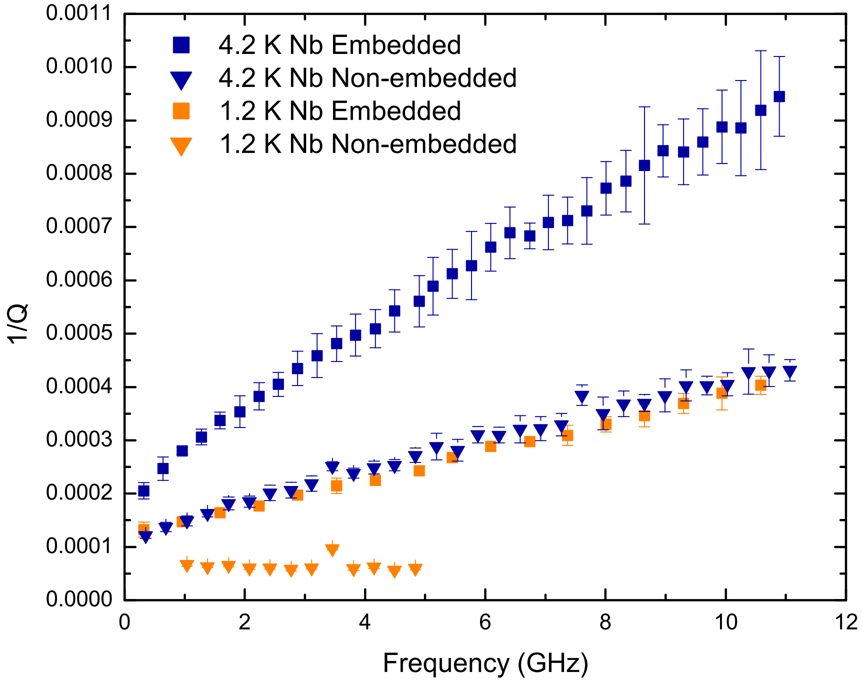

Figure 4.16: $1/Q$ vs. resonance frequencies of embedded and non-embedded Nb microstrip resonators on PI-2611 comparison at 4.2 K and 1.2 K.

ground plane, to prevent the Nb variation from different deposition runs. Both of the top layer HD-4100 is cured (225°C, $\sim$10 μm) at the same time. In order to reduce the humidity effects on the dielectric, all the samples were baked in a vacuum oven at 90°C for two hours before measurement. Then we characterized these resonators in the pulse tube cryostat from 4.2 K to 1.2 K. The Q-factor measurement results of a non-embedded and a embedded Nb resonator on HD-4100 are shown in Figure 4.17 and Figure 4.18. Figure 4.19 is the comparison of the Q-factor between non-embedded and embedded Nb resonators on HD-4100. We can see the embedded version of Nb resonator on HD-4100 shows different level of degradation at both 4.2 K and 1.2 K compare to the non-embedded Nb resonator. Further more, we also prepare both embedded and non-embedded Nb resonator on low temperature cured HD-4100 substrate (225°C, $\sim$20 μm) for investigating whether the low temperature cured HD-4100 will cause extra loss. In this case, we also keep the top polyimide layer of the embedded version as $\sim$10 μm thick and cured at 225°C. The Q-factor measurement results of these non-embedded and embedded Nb resonator are shown in Figure 4.20 and

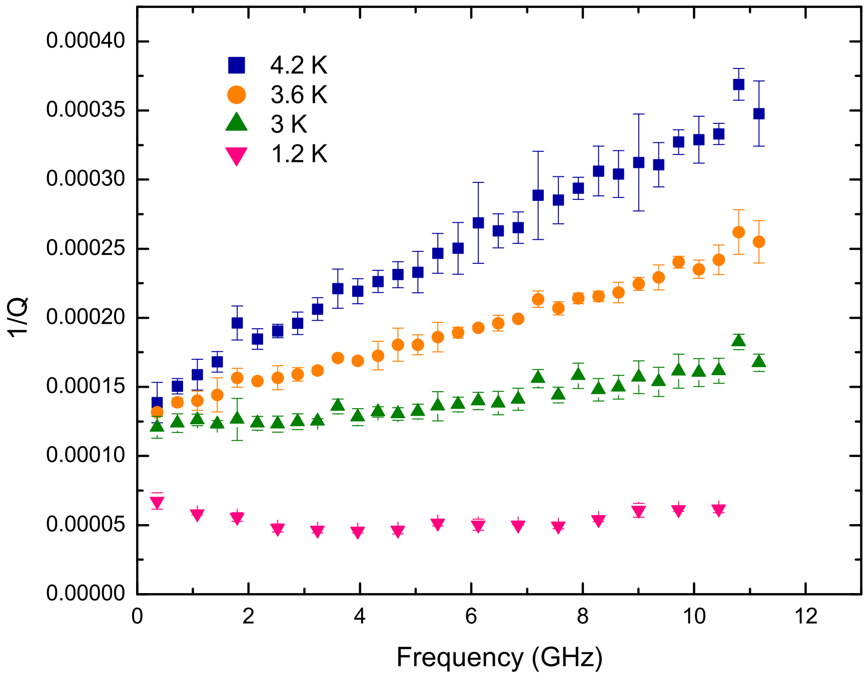

Figure 4.17: $1/Q$ vs. resonance frequencies of non-embedded Nb resonator on 350°C cured HD-4100 at various temperatures.

4.21, separately. The comparison result of these two resonators are shown in Figure 4.19. We can see it shows the similar result as the resonators on 350°C cured HD-4100, which is the Nb consistently shows degradation after a top polyimide layer curing process no matter on which type of substrates.

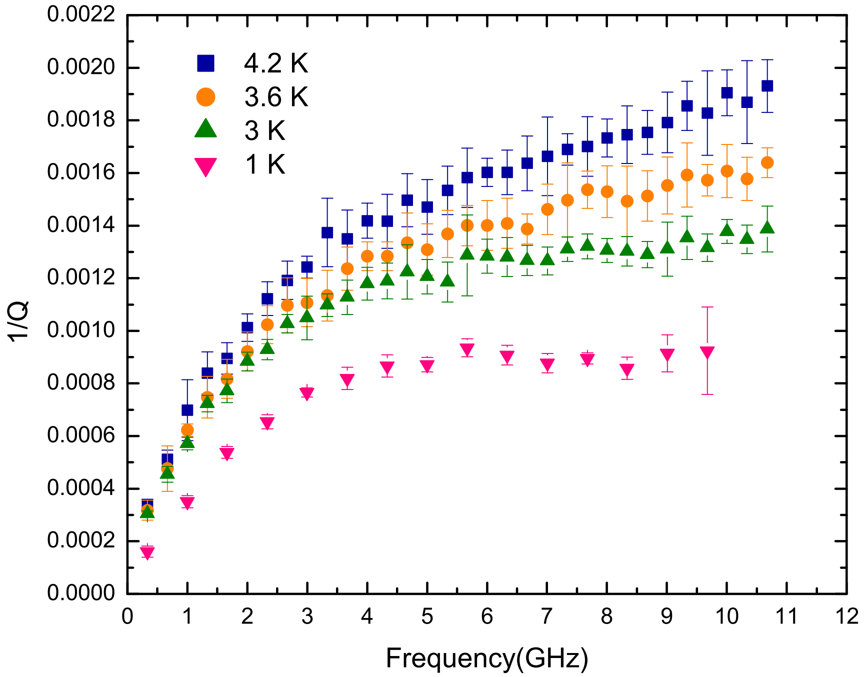

Figure 4.18: $1/Q$ vs. resonance frequencies of embedded Nb resonator on 350°C cured HD-4100 at various temperatures.

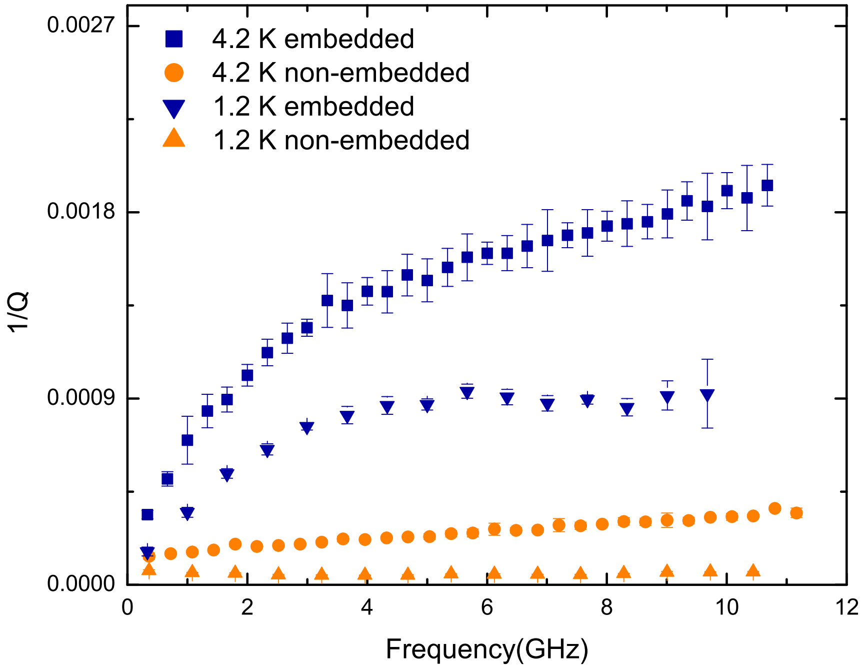

Figure 4.19: $1/Q$ vs. resonance frequencies of embedded Nb resonator on 350°C cured HD-4100 measured at 4.2 K and 1.2 K.

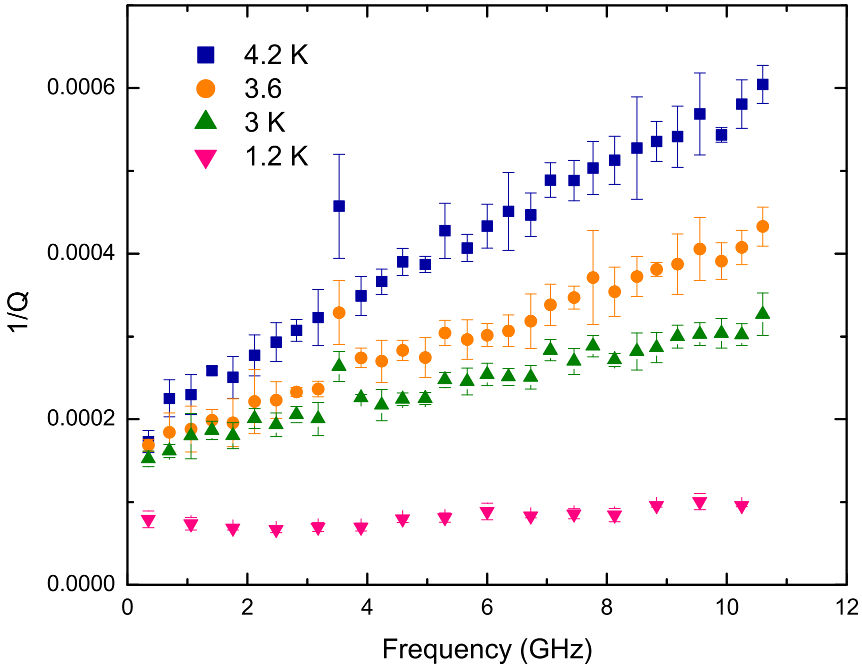

Figure 4.20: $1/Q$ vs. resonance frequencies of non-embedded Nb resonator on low temperature (225°C) cured HD-4100 substrate at various temperatures.

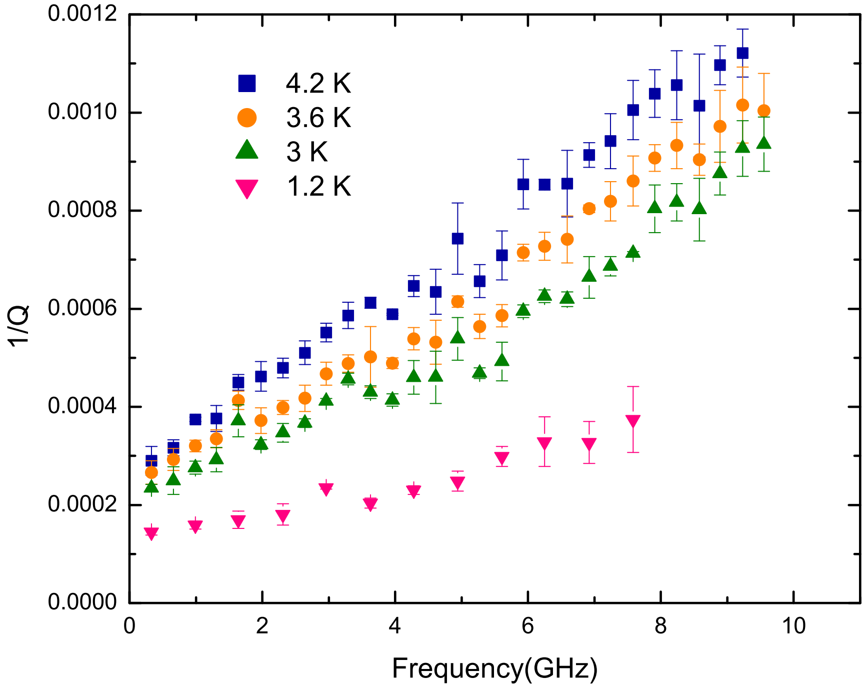

Figure 4.21: $1/Q$ vs. resonance frequencies of embedded Nb resonator on low temperature (225°C) cured HD-4100 substrate at various temperatures.

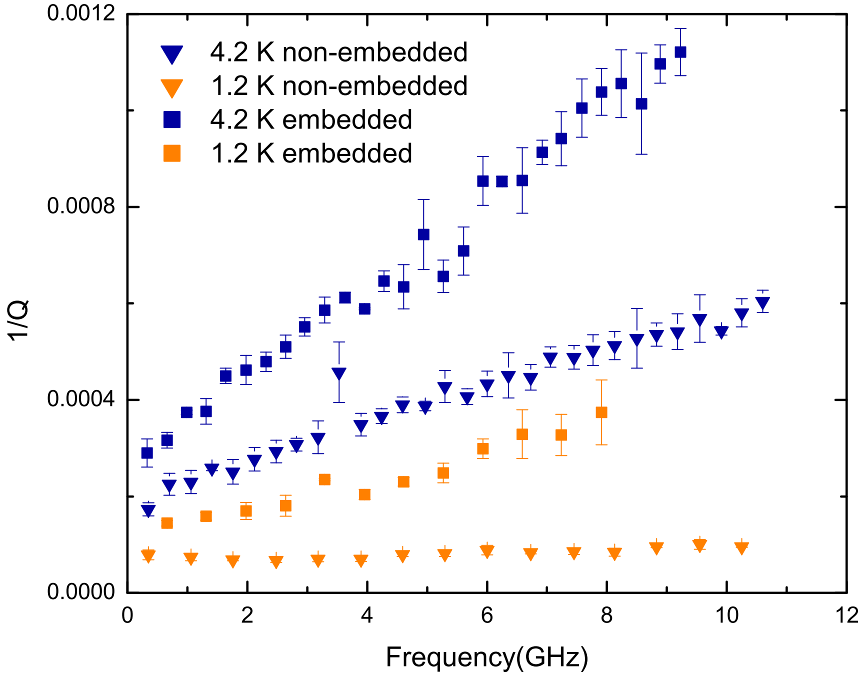

Figure 4.22: $1/Q$ vs. resonance frequencies of embedded and non-embedded Nb microstrip resonators on low temperature (225°C) cured HD-4100 comparison at 4.2 K and 1.2 K.

4.2.2 Al/Nb/Al embedded microstrip resonator on polyimide

We observed in the previous section that bare Nb can be degraded when exposed to a polyimide curing process to cure a top/embedding polyimide layer. In order to prevent the Nb quality from degrading during the curing process of the top layer polyimide, we investigated different metal cladding on Nb layer for protecting the Nb film. The result shows a thin Al (20 nm) layer can efficiently protect Nb quality from degradation during the curing process [95]. We also needed to determine the impact of the protective normal metal layer on the conductor loss. Again, resonators are ideal structures for explaining these effects.

Therefore, we fabricated non-embedded Nb/Al resonators on PI-2611 to quantify the extra conductor loss caused by the Al layer. The Q-factor measurement results of this type of resonator are shown in Figure 4.23. The comparison between non-embedded Nb resonator and non-embedded Nb/Al resonator is shown in Figure 4.24. From the measurement results, we observed the Al layer does cause some extra loss at higher temperatures (above 1.2 K). But when the temperature reaches approximately 1.2 K, the Al capped Nb trace shows comparable results of the Nb trace. The T_c of Al is $\sim$1.2 K so it make sense that the Al layer begins to exhibit superconductivity at this temperature and exhibit lower loss.

Next, an embedded Nb/Al resonator on PI-2611 was fabricated to test whether the Al can protect the Nb layer in order to obtain a higher Q compare to an unprotected Nb embedded resonator. The thickness of the protective Al layer was 20 nm and the top polyimide layer was kept it at $\sim$10 μm, which is the same as all the other embedded resonators. The cross section of this type of resonator, as well as the non-embedded version, are shown in Figure 4.25. The Q-factor measurement results of this embedded Nb/Al resonator on PI-2611 are shown in Figure 4.26. This result shows a higher Q-factor than the embedded Nb resonator but still doesn't show as high as the non-embedded version.

We proceeded under the assumption that the Nb quality was degrading during the top polyimide layer curing process and the Al layer keeps this degradation from happening. For

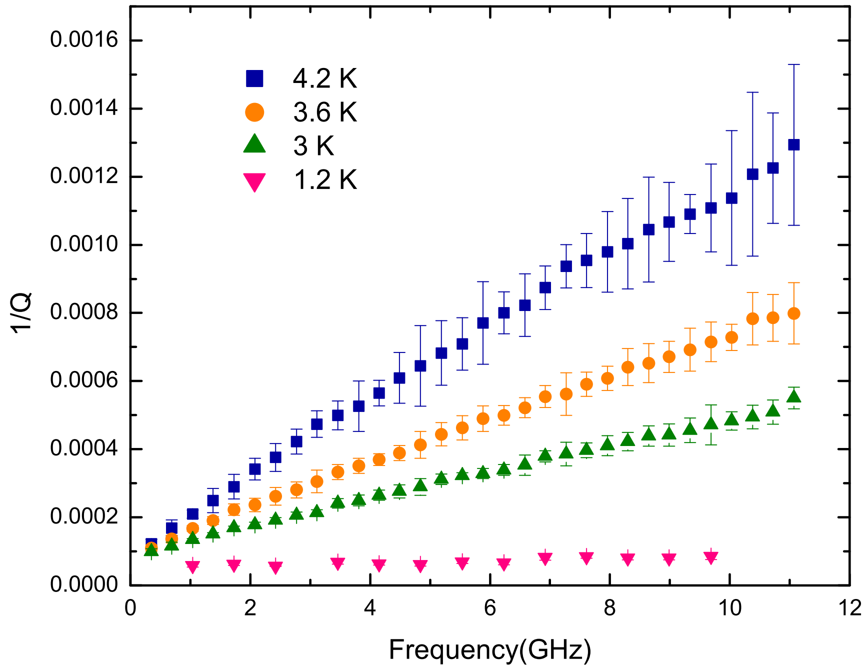

Figure 4.23: $1/Q$ vs. resonance frequencies of non-embedded Nb/Al resonator on PI-2611 measured at various temperatures.

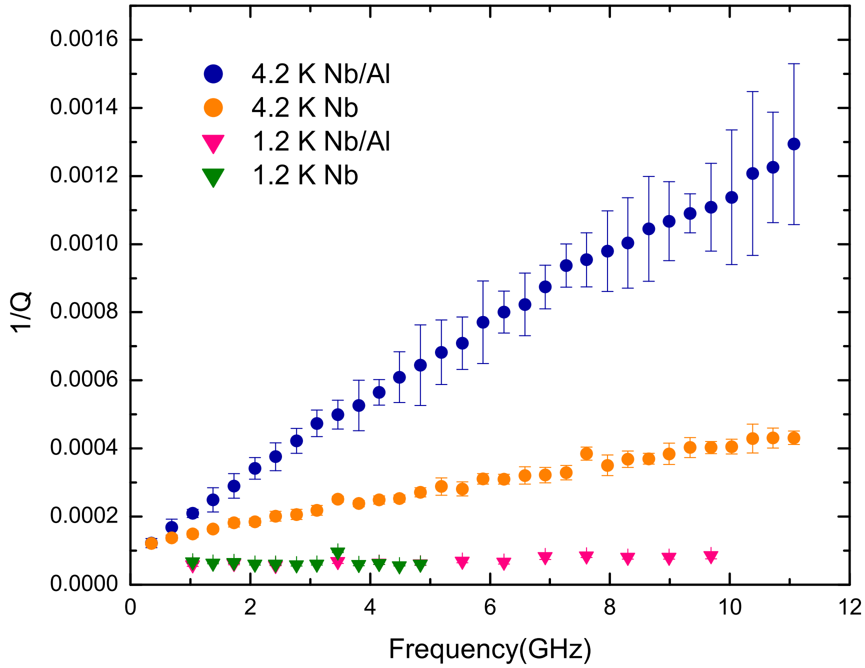

Figure 4.24: $1/Q$ vs. resonance frequencies of non-embedded Nb/Al and Nb resonators on PI-2611 comparison at 4.2 K and 1.2 K.

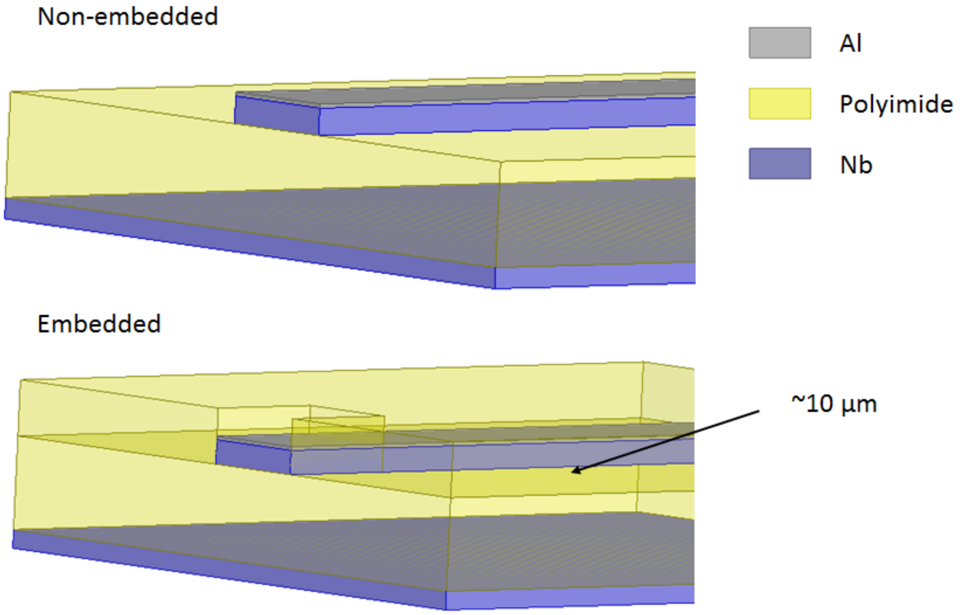

Figure 4.25: Cross section of embedded and non-embedded Nb/Al resonators on thin film polyimide.

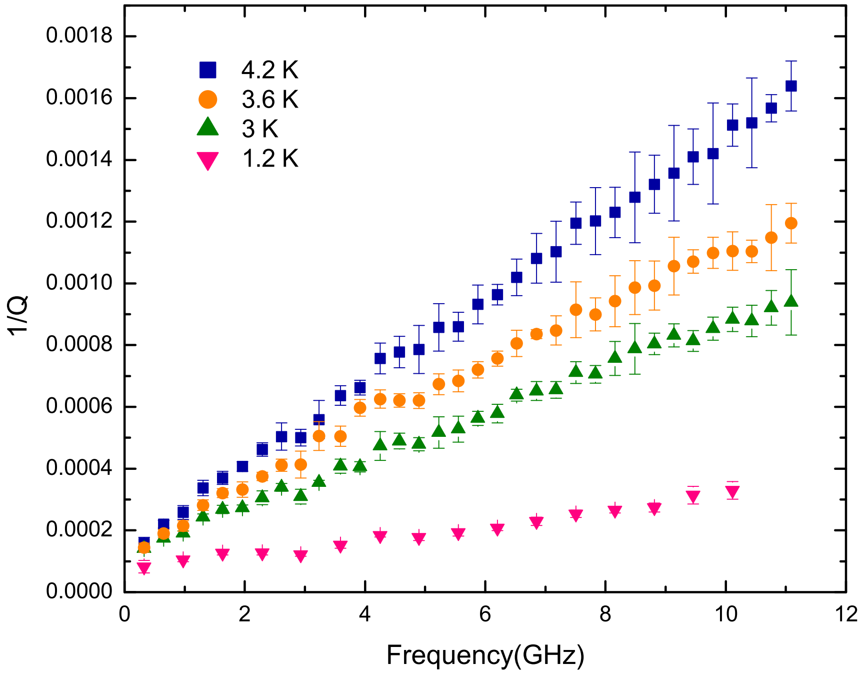

Figure 4.26: 1/Q vs. resonance frequencies of embedded Nb/Al resonator on PI-2611 measured at various temperatures.

the Nb/Al case, even though we protected the top surface of the Nb film by adding a thin Al layer, the bottom surface of the Nb film is still directly in contact to the bottom polyimide layer, and is still potentially being degraded during the top layer polyimide process.

Therefore, an Al/Nb/Al structure was considered for the signal layer metal stack up. The cross section of this type of resonator, as well as the non-embedded version, are shown in Figure 4.27. The quality factor measurement results of embedded Al/Nb/Al resontor on PI-2611 are shown in Figure 4.28. From this plot, we can clearly see the Q-factor improved comparing to other embedded resonators at 1.2 K. The summary results of all types of embedded resonators with a different signal metal combination are shown in Figure 4.29. There is a clear Q value improvement for the embedded Al/Nb/Al resonator compared to other embedded resonators. This provides strong evidence that a thin Al layer, above and below the Nb layer, can effectively protect the Nb signal layer from being degraded during subsequent processing steps. This Al/Nb/Al sandwich metal structure is suitable

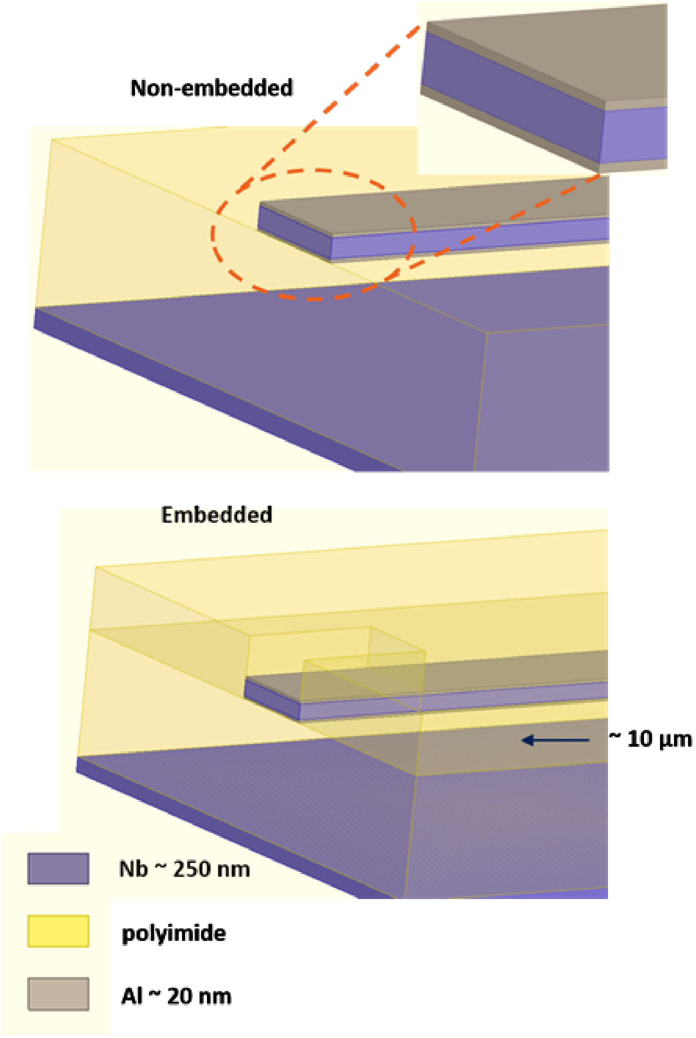

Figure 4.27: Cross section of embedded and non-embedded Al/Nb/Al resonators on polyimide.

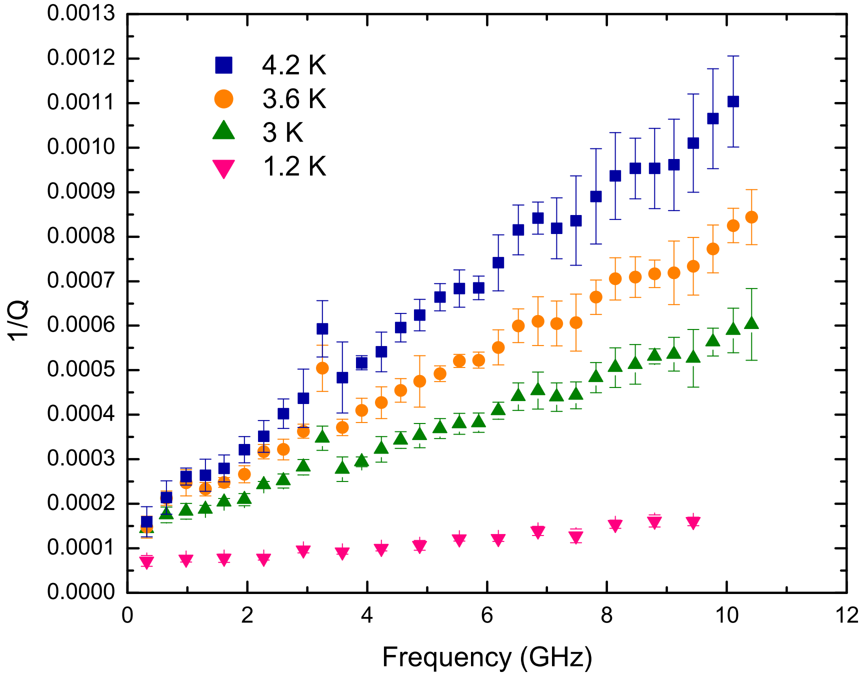

Figure 4.28: $1/Q$ vs. resonance frequencies of embedded Al/Nb/Al resonator on PI-2611 measured at various temperatures.

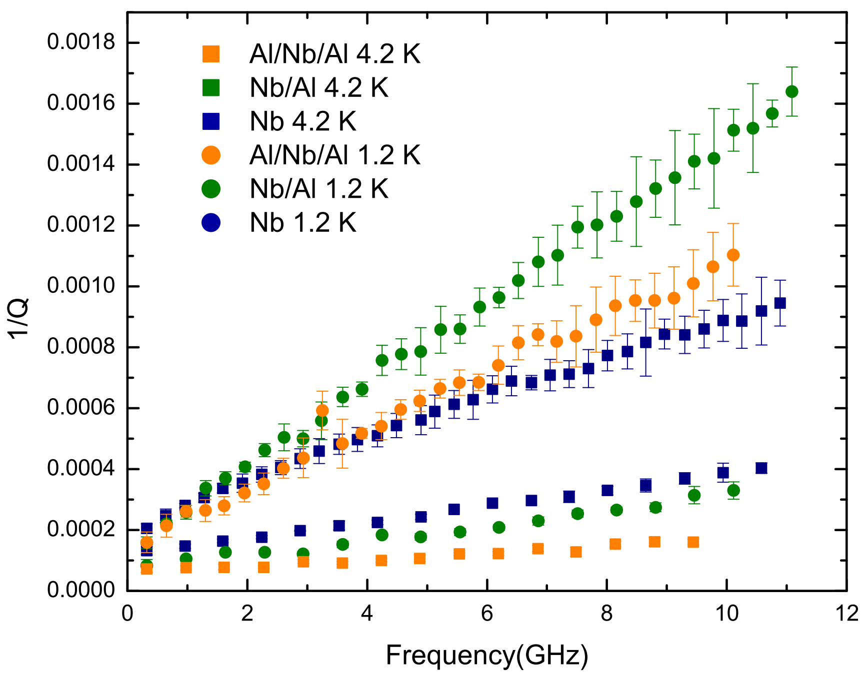

Figure 4.29: $1/Q$ vs. resonance frequencies of embedded Al/Nb/Al, Nb/Al and Nb resonators on PI-2611 comparison at 4.2 K and 1.2 K.

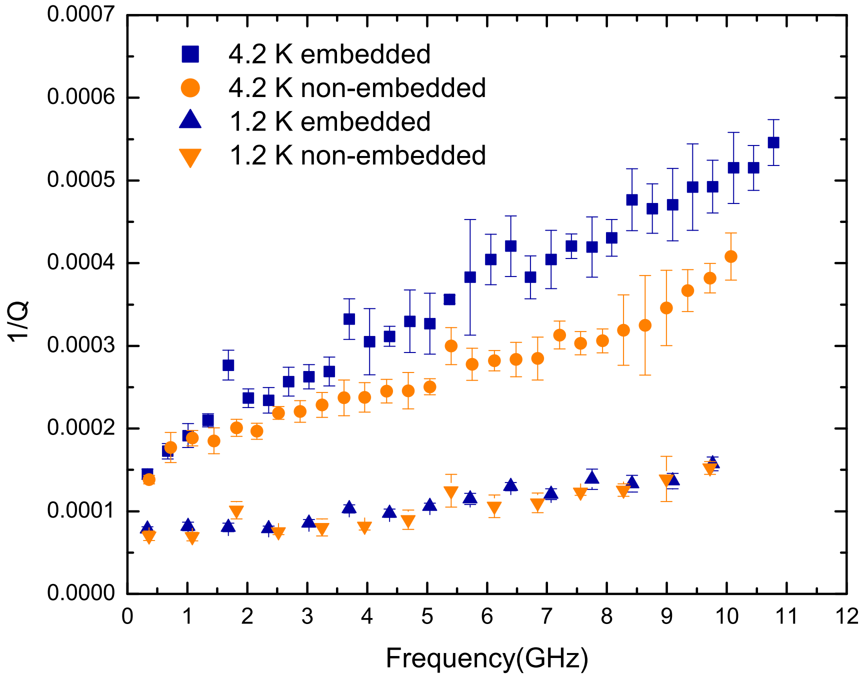

Figure 4.30: $1/Q$ vs. resonance frequencies of embedded and non-embedded Al/Nb/Al resonator on HD-4100 comparison at 4.2 K and 1.2 K.

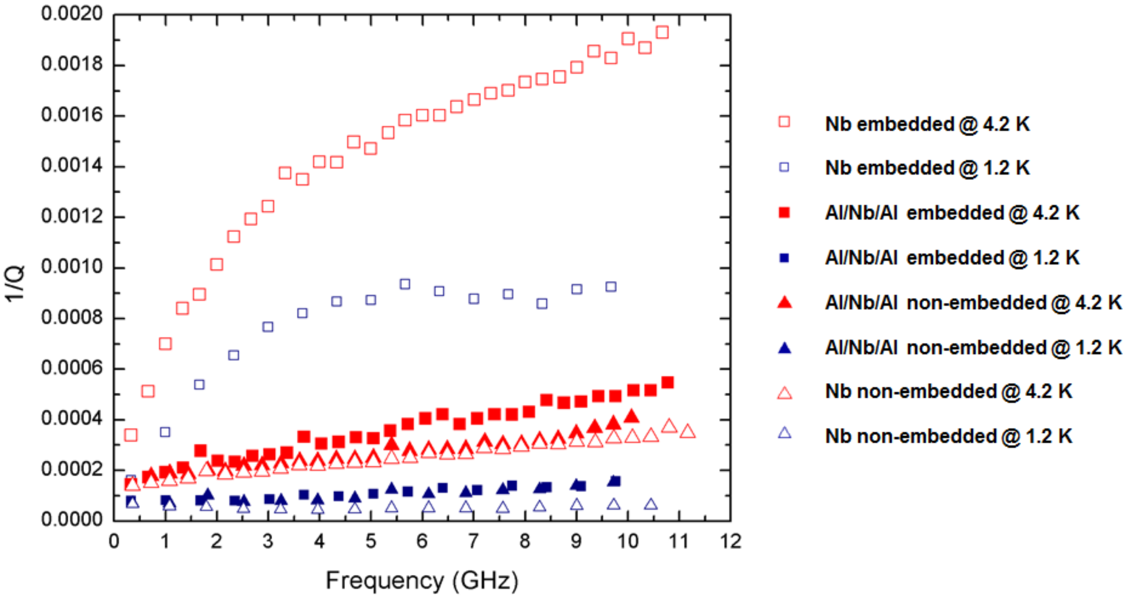

Figure 4.31: $1/Q$ vs. resonance frequencies of embedded Al/Nb/Al, Nb/Al and Nb embedded resonators on HD-4100 comparison at 4.2 K and 1.2 K.

and potential to be useful for building more complex polyimide based multi-layer microwave structures.

Another photo-definable polyimide, HD-4100, was also investigated in this work. All of the bottom layer polyimide (20 μm thick HD-4100, cured at 350°C) were prepared at the same time. For comparison, we deposited Al/Nb/Al signal layer together for both embedded and non-embedded resonators. In order to avoid normal metal causing extra conductor loss, we chose Nb as ground side metal. The ground side Nb was also deposited at the same time for all of these resonators. Furthermore, the top layer polyimide (225° cured HD-4100, $\sim$10 μm), on both embedded Nb and embedded Al/Nb/Al resonator, were all cured at the same time. The comparison results of the embedded, non-embedded Al/Nb/Al resonator on HD-4100 are shown in Figure 4.30. The summary results of embedded, non-embedded Nb resonator and embedded, non-embedded Al/Nb/Al resonators are shown in Figure 4.31. In this figure, we removed the error bar for clarification. We can clearly see at 1.2 K, the Al/Nb/Al embedded and non-embedded resonators show comparable results. The Al/Nb/Al embedded resonator shows slightly lower Q than the non-embedded version because the electrical field passes through more dielectric volume than the non-embedded version. However, the embedded Nb resonator shows much lower Q than the embedded Al/Nb/Al resonator, which provides further evidence that the Nb quality of the signal layer gets degraded during the top layer dielectric curing process and that Al can be a useful protection layer.

Chapter 5

Conclusion

The results of this work indicate that superconductors such as Nb and NbN can only realize superconductivity on selected substrates, especially non-crystalline flexible substrates, such as Kapton polyimide. Based on our experimental results, we believe that surface roughness of the substrate material could potentially be the reason we observed superconductivity suppression of NbN films, especially for narrow line structures. The narrow lines that that we defined were only 119 μm wide on Kapton by using traditional photolithography methods. The patterned lines were the width that would be used in a microstrip resonator or line to have a characteristic impedance of 50 Ω. These lines were as process monitors to measure the transition temperature (T_c) of superconducting thin films. We studied various types of commonly available Kapton, including EN, HN, and FN series. NbN and Nb narrow lines consistently showed fully transition ($R_{dc} = 0$ when $T \leq T_c$) on E-series (EN and Tab-E) Kapton.

Therefore, we selected E-series Kapton with 2 mil thickness as our substrate material for the fabrication of superconducting resonators. The purpose was to characterize the dielectric properties of the E-series Kapton, which could then be used for flex cable fabrication. Therefore, we purposefully built Cu and Nb resonators on these E-series Kapton to extract the microwave dielectric information at cryogenic temperatures. We measured both types of resonators at temperatures below 6 K and extracted a relative dielectric constant of 3.2 in the 2-10 GHz range, with loss tangents less than 0.001. The properties of these films are important for designing microwave electronics and flexible interconnects based on Kapton. These results show that Kapton has promising microwave properties that could potentially be used in future cryogenic systems.

In this work, we were also interested in characterizing the microwave properties of various types of spin on polyimide films such as PI-2611 and HD-4100. We designed and fabricated high quality factor Nb half-wavelength microstrip resonators. In order to characterize the dielectric at various frequencies, different lengths of resonators were designed and fabricated. Both types of polyimide films were measured in a pulse tube as free standing films with edge launch connectors attached. For a 5 cm long resonator, we measured Q-factors that were in excess of 13 000 for PI-2611 and 17 000 for HD-4100 at approximately 1 K. This shows that the 20 μm polyimide (PI-2611 and HD-4100) thin films provide a loss tangent at 2 GHz of less than 1.0×10^{-4}. These results indicate that these materials can potentially be used as substrate materials for future cryogenic microwave devices and cables.

We also studied the impact of humidity on the microwave performance of both types of polyimide films at cryogenic temperatures. Here we reported the dielectric constant and loss tangent changes of these thin film polyimide at cryogenic temperatures during the humidity-recovery treatment. Superconducting Nb resonators were fabricated directly onto thin polyimide film and characterized at 1 to 4.2 K to extract the microwave properties changes. Both of them show increasing dielectric loss during the humidity treatment, while this effect can be eliminated after a bake out process. Both types of polyimide film shows the ability to recover after a bake out treatment. PI-2611 dielectric constant exhibited greater sensitivity to humidity exposure than the HD-4100 film.

In addition, to studying the dielectric sensitivity to humidity exposure, we also looked at the impact of underlayer and cladding of Nb on microwave loss. We therefore focused on thin Ti (10 nm, 50 nm) underlayer and also different thickness Cu (20 nm, 50 nm, 100 nm and 200 nm) as cladding layers. All of these different metal stack ups exhibited superconductivity at relatively the same transition temperature of ∼9 K. The quality factor measurement result showed all the normal metal layer induce an additional conductor loss while these losses are reduced significantly along with the decreasing temperature to a residual surface resistance as expected for a superconductor in the Bardeen-Cooper-Schrieffer (BCS) theory [96]. Based on the experimental results, we found when this normal layer is thin enough below (50 nm), it does not introduce significant metal loss at ∼1 K.

In order to build multilayer structures such as stripline in the future, we also built embedded microstrip lines on these dielectrics. The experimental results indicate the Nb film quality is degraded and superconductivity is lost at high curing temperatures. In order to finish the curing process on top of the Nb layer, we chose a lower curing temperature (225°C) process. We were able to successfully build embedded superconducting microstrip transmission resonators based on a low-temperature curing process. While the results show the Nb thin film quality still is degraded even after the curing temperature of the top polyimide layer was lowered. Here we then proposed a solution by using Al/Nb/Al encapsulation metal structure instead of Nb only to build this embedded structure. The result shows the both Al layer (20 nm) protects the Nb quality against degradation during the curing process. Even though the Al layer introduces conductor loss at a higher temperature range (above 1.2 K), the conductor loss decreases significantly when the temperature is below 1.2 K.

Chapter 6

Future work

Superconducting resonators can provide accurate loss tangent information of a dielectric at various cryogenic temperatures. There are several dielectrics that are commonly used in device packaging that may provide improved microwave and mechanical properties at cryogenic temperatures. Therefore, superconducting resonators could be fabricated and measured in a similar fashion to the work presented.

There were several issues that were discussed in this dissertation that would need to be explored further. First, we mentioned measurements of narrow (120 μm) Nb lines that exhibited superconductivity on E-series Kapton, but not on other types of Kapton. We suspected the surface defects on the other types of Kapton prevented the Nb from becoming superconducting. It would be useful to undertake a comprehensive study of the Kapton surface (optical microscopy, AFM and SEM) to determine the types of defects that can cause the superconductivity suppression. The result of this study would provide a framework for selecting similar types of dielectric films. Second issue we observed, was an abnormal second harmonic (lower Q than expected) when we measured superconducting resonators on polyimide films, at present we have not determined the root cause. We suspect the second harmonic abnormality is related to the humidity level of the sample or the location of the sample in the measurement chamber. To understand the reason we observed a second harmonic decrease in Q, would allow us to either improve our measurement system or how we interfaced to the sample.

We also demonstrated embedded microstrip resonators that showed promising results. Therefore a logical next-step would be to build multi-layer superconducting microwave structures. The benefit of developing fully enclosed microwave structure includes providing better protection to superconductor from the environment and handling. In our current work, we successfully built embedded microstrip resonators by using low temperature (225°C) cured polyimide with an Al/Nb/Al sandwich structure that kept the Nb quality from degrading. A multi-layer structure such as stripline structure, would require corresponding stripline resonator to characterize the effective dielectric constant as well as the dielectric loss. Although for stripline, vias will be required to route the ground plane and signal line to the top most dielectric layer. Vias introduce significant fabrication challenges, but first steps should involve using normal-conductor vias and then proceed to a fully-superconducting stripline, therefore paving the way for integrating other microwave structures in-situ such as attenuators.

Another area that may require improvement, is the method we make connections to our flex cables. Development of a suitable cryogenic microwave packaging fixture, where a flex cable could be easily mounted and measured repeatedly would save significant time in assembly and testing. Currently, we use edge launch SMA connectors and solder to the microstrip resonators directly. The assembling process causes a lot of variation from both the soldering process and handling aspect. Currently, the SMA connector we have used are heavy, which can potentially cause damage to our thin samples. If we can replace the edge launch connector by a fixed package case such as the one shown in Figure 6.1, we could easily replace the sample when we need to measure it, this would simplify the assembling process. Furthermore, these package fixtures can potentially be used to measure longer transmission line structure such as a one-meter long microstrip line by including a fixture at the end of each cable. At last, wire bonding will allow more narrow traces in the design. Currently, our narrowest connection pad is 120 μm wide for soldering, which introduces significant mismatch and hinders the microwave performance especially in our transmission line designs.

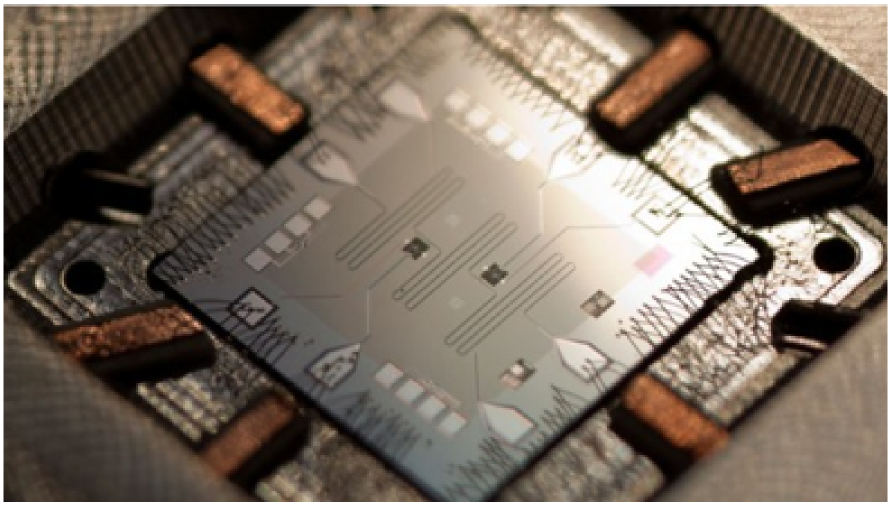

Figure 6.1: The UCSB von Neumann quantum computer. Measurement package for resonators and superconducting qubits. This is adapted from [97].

Bibliography

[1] M. Tinkham, *Introduction to superconductivity.* Courier Corporation, 1996.

[2] P.-G. De Gennes, *Superconductivity of metals and alloys (advanced book classics).* Perseus Books Group, 1999.

[3] (2013) Superconductors - what do we know. [Online]. Available: http://physicsrebel.blogspot.com/2013/02/superconductors-what-do-we-know.html

[4] C. Kittel, *Introduction to solid state physics*, 7th ed. New York: Wiley, 1995.

[5] J. Eck. (2007) Type 1 superconductors and a periodic chart comparison. [Online]. Available: http://www.superconductors.org/type1.htm

[6] J. Halbritter, "RF residual losses, surface impedance, and granularity in superconducting cuprates," *Journal of applied physics*, vol. 68, no. 12, pp. 6315–6326, 1990.

[7] C. Kircher, "Superconducting proximity effect of Nb," *Physical Review*, vol. 168, no. 2, p. 437, 1968. [Online]. Available: http://dx.doi.org/10.1103/PhysRev.168.437

[8] H. Padamsee, *RF Superconductivity: Volume II: Science, Technology and Applications.* John Wiley & Sons, 2009.

[9] R. Kleiner and W. Buckel, *Superconductivity: An Introduction.* John Wiley & Sons, 2015.

[10] S. M. Anlage. (2002) Superconductors and cryogenics in microwave subsystems. [Online]. Available: http://anlage.umd.edu/Anlage%20ASC2002%20SCandCryoMicroSub%20Tutorial%20Talk.pdf

[11] J. R. Waldram, *Superconductivity of metals and cuprates.* CRC Press, 1996.

[12] T. Van Duzer and C. W. Turner, *Principles of superconductive devices and circuits.* Prentice Hall, 1981.

[13] W. Buckel, *Superconductivity. Fundamentals and applications. 3. rev.* John Wiley & Sons, 1984.

[14] J. Quateman, "T_c suppression and critical fields in thin superconducting Nb films," *Physical Review B*, vol. 34, no. 3, p. 1948, 1986.

[15] W. Van Huffelen, T. Klapwijk, and E. T. M. Suurmeijer, "Critical temperature of thin niobium films on heavily doped silicon," *Physical Review B*, vol. 47, no. 9, p. 5151, 1993.

[16] R. Meservey and B. B. Schwartz. (1996) Characteristic lengths in superconductors. [Online]. Available: http://hyperphysics.phy-astr.gsu.edu/hbase/solids/chrlen.html

[17] W. R. Hudson and R. J. Jirberg, "Superconducting properties of niobium films," *NASA Technical Brief*, Jun. 1971.

[18] N. B. Kopnin, *Theory of nonequilibrium superconductivity.* Oxford University Press, 2001, vol. 110.

[19] J. Ekin, *Experimental Techniques for Low-Temperature Measurements: Cryostat Design, Material Properties and Superconductor Critical-Current Testing.* Oxford university press, 2006.

[20] D. R. Tilley and J. Tilley, *Superfluidity and superconductivity.* CRC Press, 1990.

[21] W. Carr Jr, *AC loss and macroscopic theory of superconductors.* CRC Press, 2001.

[22] R. Kleiner, R. Hott, T. Wolf, G. Zwicknagl, M. Belogolovskii, S. T. Ruggiero, S. C. Wimbush, F. Grilli, and F. Sirois, *Applied Superconductivity: Handbook on Devices and Applications.* Wiley Online Library, 2015.

[23] T. Van Duzer, C. Turner, D. McDonald, and A. F. Clark, "Principles of superconductive devices and circuits," *Physics Today*, vol. 35, p. 80, 1982.

[24] U. of Cambridge. (2008) Superconductivity. [Online]. Available: http://www.doitpoms.ac.uk/tlplib/superconductivity/printall.php

[25] P. Visani, "Superconducting proximity effect between silver and niobium," Ph.D. dissertation, Diss. Naturwiss. ETH Zürich, Nr. 9046, 1990. Ref.: AC Mota; Korref.: JL Olsen; Korref.: TM Rice, 1990.

[26] W. McMillan, "Tunneling model of the superconducting proximity effect," *Physical Review*, vol. 175, no. 2, p. 537, 1968.

[27] I. Banerjee, Q. Yang, C. M. Falco, and I. K. Schuller, "Superconductivity of Nb/Cu superlattices," *Solid State Communications*, vol. 41, no. 11, pp. 805–808, 1982.

[28] I. Banerjee, Q. S. Yang, C. M. Falco, and I. K. Schuller, "Anisotropic critical fields in superconducting superlattices," *Phys. Rev. B*, vol. 28, pp. 5037–5040, Nov 1983. [Online]. Available: http://link.aps.org/doi/10.1103/PhysRevB.28.5037

[29] V. Cherkez, J. Cuevas, C. Brun, T. Cren, G. Ménard, F. Debontridder, V. Stolyarov, and D. Roditchev, "Proximity effect between two superconductors spatially resolved by scanning tunneling spectroscopy," *Physical Review X*, vol. 4, no. 1, p. 011033, 2014.

[30] C. S. Yung and B. H. Moeckly, "Magnesium diboride flexible flat cables for cryogenic electronics," *IEEE Transactions on Applied Superconductivity*, vol. 21, no. 3, pp. 107–110, 2011.

[31] M.-Y. Cheng, W.-T. Park, A. Yu, R.-F. Xue, K. L. Tan, D. Yu, S.-H. Lee, C. L. Gan, and M. Je, "A flexible polyimide cable for implantable neural probe arrays," *Microsystem technologies*, vol. 19, no. 8, pp. 1111–1118, 2013.

[32] T. Tighe, G. Akerling, and A. Smith, "Cryogenic packaging for multi-GHz electronics," *Applied Superconductivity, IEEE Transactions on*, vol. 9, no. 2, pp. 3173–3176, 1999.

[33] M. Lu, Z. Qian, W. Ren, S. Liu, and D. Shangguan, "Investigation of electronic packaging materials by using a 6-axis mini thermo-mechanical tester," *International Journal of Solids and Structures*, vol. 36, no. 1, pp. 65–78, 1999.

[34] M. Kochi, H. Shimada, and H. Kambe, "Molecular aggregation and mechanical properties of kapton H," *Journal of Polymer Science: Polymer Physics Edition*, vol. 22, no. 11, pp. 1979–1985, 1984.

[35] J. Lawrence, A. Patel, and J. Brisson, "The thermal conductivity of kapton HN between 0.5 and 5 K," *Cryogenics*, vol. 40, no. 3, pp. 203–207, 2000.

[36] H. Yokoyama, "Thermal conductivity of polyimide film at cryogenic temperature," *Cryogenics*, vol. 35, no. 11, pp. 799–800, 1995.

[37] A. Harris, M. Sieth, J. Lau, S. Church, L. Samoska, and K. Cleary, "Note: Cryogenic microstripline-on-kapton microwave interconnects," *Review of Scientific Instruments*, vol. 83, no. 8, p. 086105, 2012.

[38] N. Simon, "Cryogenic properties of inorganic materials for iter magnets: A review," *NIST Internal/Interagency Reports 5030*, pp. 1–205, 1994.

[39] B. Weedy and S. Swingler, "A review of dielectrics for flexible superconducting cables," *Cryogenics*, vol. 24, no. 7, pp. 367–370, 1984.

[40] H. Yamaoka, K. Miyata, and O. Yano, "Cryogenic properties of engineering plastic films," *Cryogenics*, vol. 35, no. 11, pp. 787–789, 1995.

[41] J. Chervenak and J. Mateo, "Flexible microstrip circuits for superconducting electronics," *NASA Technical Brief*, pp. 5–6, Dec. 2013.

[42] H. Matsutani, T. Hattori, M. Ohe, T. Ueno, R. L. Hubbard, and Z. Fathi, "Low temperature curing of polyimide precursors by variable frequency microwave," *Journal of Photopolymer Science and Technology*, vol. 18, no. 2, pp. 327–332, 2005.

[43] S. Bauer and A. S. De Reggi, "Pulsed electrothermal technique for measuring the thermal diffusivity of dielectric films on conducting substrates," *Journal of applied physics*, vol. 80, no. 11, pp. 6124–6128, 1996.

[44] D. C. Thompson, O. Tantot, H. Jallageas, G. E. Ponchak, M. M. Tentzeris, and J. Papapolymerou, "Characterization of liquid crystal polymer (LCP) material and transmission lines on LCP substrates from 30 to 110 ghz," *Microwave Theory and Techniques, IEEE Transactions on*, vol. 52, no. 4, pp. 1343–1352, 2004.

[45] R. Vyas, A. Rida, S. Bhattacharya, and M. M. Tentzeris, "Liquid crystal polymer (LCP): The ultimate solution for low-cost RF flexible electronics and antennas," in *Antennas and Propagation Society International Symposium, 2007 IEEE.* IEEE, 2007, pp. 1729–1732.

[46] G. Wang, D. Thompson, E. M. Tentzeris, and J. Papapolymerou, "Low cost RF MEMS switches using LCP substrate," in *34th European Microwave Conf., Amsterdam, The Netherlands.* Citeseer, 2004.

[47] G. DeJean, R. Bairavasubramanian, D. Thompson, G. Ponchak, M. Tentzeris, and J. Papapolymerou, "Liquid crystal polymer (LCP): a new organic material for the development of multilayer dual-frequency/dual-polarization flexible antenna arrays," *Antennas and Wireless Propagation Letters, IEEE*, vol. 4, pp. 22–26, 2005.

[48] D. J. Chung, S. K. Bhattacharya, and J. Papapolymerou, "Low loss multilayer transitions using via technology on LCP from DC to 40 GHz," in *Electronic Components and Technology Conference, 2009. ECTC 2009. 59th.* IEEE, 2009, pp. 2025–2029.

[49] V. Palazzari, S. Pinel, J. Laskar, L. Roselli, and M. M. Tentzeris, "Design of an asymmetrical dual-band WLAN filter in liquid crystal polymer (LCP) system-on-package technology," *Microwave and Wireless Components Letters, IEEE*, vol. 15, no. 3, pp. 165–167, 2005.

[50] L. Chen, M. Crnic, Z. Lai, and J. Liu, "Process development and adhesion behavior of electroless copper on liquid crystal polymer (LCP) for electronic packaging application," *Electronics Packaging Manufacturing, IEEE Transactions on*, vol. 25, no. 4, pp. 273–278, 2002.

[51] R. Wormald, S. David, G. Panaghiston, and R. Jeffries, "A low cost packaging solution for microwave applications," in *European Microwave Integrated Circuits Conference, 2006. The 1st.* IEEE, 2006, pp. 205–208.

[52] K. J. Jayaraj, T. E. Noll, and D. Singh, "RF characterization of a low cost multichip packaging technology for monolithic microwave and millimeter wave integrated circuits," in *Signals, Systems, and Electronics, 1995. ISSSE'95, Proceedings., 1995 URSI International Symposium on.* IEEE, 1995, pp. 443–446.

[53] R. N. Dean Jr, J. Weller, M. Bozack, B. Farrell, L. Jauniskis, J. Ting, D. Edell, and J. Hetke, "Novel biomedical implant interconnects utilizing micromachined LCP," in *Optical Science and Technology, the SPIE 49th Annual Meeting.* International Society for Optics and Photonics, 2004, pp. 88–99.

[54] G. Zou, H. Gronqvist, Z. Lai, U. SodervalI, and J. Liu, "High frequency flip chip interconnection on liquid crystal polymer substrate using anisotropic conductive adhesive," in *Polymers and Adhesives in Microelectronics and Photonics, 2004. POLYTRONIC 2004. 4th IEEE International Conference on.* IEEE, 2004, pp. 137–140.

[55] S.-H. Hwang, K.-S. Jeong, and J.-C. Jung, “Thermal and mechanical properties of amorphous copolyester (PETG)/LCP blends,” *European polymer journal*, vol. 35, no. 8, pp. 1439–1443, 1999.

[56] T. J. Dingemans, S. van der Zwaag, A. Knijnenberg, E. S. Weiser, and B. J. Jensen, “Novel liquid crystal thermoset resins for cryogenic fuel tank applications,” in *The 24th international congress of the aeronautical sciences*, 2004.

[57] D. Evans and J. Morgan, “Low temperature mechanical and thermal properties of liquid crystal polymers,” *Cryogenics*, vol. 31, no. 4, pp. 220–222, 1991.

[58] M. D. Henry, S. Wolfley, T. Monson, B. G. Clark, E. Shaner, and R. Jarecki, “Stress dependent oxidation of sputtered niobium and effects on superconductivity,” *Journal of Applied Physics*, vol. 115, no. 8, p. 083903, 2014.

[59] M. Lucci, S. Sanna, G. Contini, N. Zema, V. Merlo, M. Salvato, H. Thanh, and L. Davoli, “Electron spectroscopy study in the NbN growth for NbN/AlN interfaces,” *Surface Science*, vol. 601, p. 26472650, 2007.

[60] C. Sinclair and S. Nightingale, “An equivalent circuit model for the coplanar waveguide step discontinuity,” *1992 IEEE Microwave Symposium Digest MTT-S*, pp. 1461–1464, 1992.

[61] A. Megrant, C. Neill, R. Barends, B. Chiaro, Y. Chen, L. Feigl, J. Kelly, E. Lucero, M. Mariantoni, P. OMalley *et al.*, “Planar superconducting resonators with internal quality factors above one million,” *Applied Physics Letters*, vol. 100, no. 11, p. 113510, 2012.

[62] J. M. Heinola and K. Tolsa, “Dielectric characterization of printed wiring board materials using ring resonator techniques: A comparison of calculation models,” *IEEE Transactions on Dielectrics and Electrical Insulation*, vol. 13, no. 4, pp. 717–726, 2006.

[63] B. A. Mazin, “Microwave kinetic inductance detectors,” Ph.D. dissertation, Citeseer, 2004.

[64] E. Belohoubek and E. Denlinger, “Loss considerations for microstrip resonators,” *Microwave Theory and Techniques, IEEE Transactions on*, vol. 23, no. 6, pp. 522–526, 1975.

[65] J. Hornibrook, E. Mitchell, and D. Reilly, “Superconducting resonators with parasitic electromagnetic environments,” *arXiv preprint arXiv:1203.4442*, 2012.

[66] B. Sanders. (2013) Distant artificial atoms cooperate by sharing light, physicists show. [Online]. Available: http://phys.org/news/2013-11-distant-artificial-atoms-cooperate-physicists.html

[67] A. Wallraff, D. I. Schuster, A. Blais, L. Frunzio, R.-S. Huang, J. Majer, S. Kumar, S. M. Girvin, and R. J. Schoelkopf, “Strong coupling of a single photon to a superconducting qubit using circuit quantum electrodynamics,” *Nature*, vol. 431, no. 7005, pp. 162–167, 2004.

[68] B. A. Mazin, P. K. Day, K. D. Irwin, C. D. Reintsema, and J. Zmuidzinas, "Digital readouts for large microwave low-temperature detector arrays," *Nuclear Instruments and Methods in Physics Research Section A: Accelerators, Spectrometers, Detectors and Associated Equipment*, vol. 559, no. 2, pp. 799–801, 2006.

[69] S. McHugh, B. A. Mazin, B. Serfass, S. Meeker, K. OBrien, R. Duan, R. Raffanti, and D. Werthimer, "A readout for large arrays of microwave kinetic inductance detectors," *Review of Scientific Instruments*, vol. 83, no. 4, p. 044702, 2012.

[70] R. Bai, G. A. Hernandez, Y. Cao, J. A. Sellers, C. D. Ellis, D. B. Tuckerman, and M. C. Hamilton, "Cryogenic microwave characterization of kapton polyimide using superconducting resonators," in *Microwave Symposium (IMS), 2016 IEEE MTT-S International.* IEEE, 2016, pp. 1–4.

[71] G. A. Hernandez, R. Bai, Y. Cao, J. A. Sellers, C. D. Ellis, D. B. Tuckerman, and M. C. Hamilton, "Microwave performance of niobium/kapton superconducting flexible cables," *IEEE Transactions on Applied Superconductivity*, In review.

[72] S. Cherednichenko, P. Yagoubov, K. Ilin, G. Goltsman, and E. Gershenzon, "Large bandwidth of NbN phonon-cooled hot-electron bolometer mixers on sapphire substrates," in *Proc. 8th Int. Symp. on Space Terahertz Technology*, 1997.

[73] C. M. Chorey, K.-S. Kong, K. B. Bhasin, J. Warner, and T. Itoh, "YBCO superconducting ring resonators at millimeter-wave frequencies," *Microwave Theory and Techniques, IEEE Transactions on*, vol. 39, no. 9, pp. 1480–1487, 1991.

[74] D. B. Tuckerman, M. C. Hamilton, D. J. Reilly, R. Bai, G. A. Hernandez, J. M. Hornibrook, J. A. Sellers, and C. D. Ellis, "Flexible superconducting nb transmission lines on thin film polyimide for quantum computing applications," *Superconductor Science and Technology*, vol. 29, no. 8, p. 084007, 2016.

[75] J.Molla, A.Ibarra, J.Margineda, J.M.Zamarro, and A.Hernandez, *Dielectric properties measurement system at cryogenic temperaturas and microwave frequencies.* Centro De Investigaciones EnergÉticas, Medioambientales Y TecnolÓgicas, 1994.

[76] S. Metz, A. Bertsch, and P. Renaud, "Partial release and detachment of microfabricated metal and polymer structures by anodic metal dissolution," *Microelectromechanical Systems, Journal of*, vol. 14, no. 2, pp. 383–391, 2005.

[77] J. Ku, V. Manucharyan, and A. Bezryadin, "Superconducting nanowires as nonlinear inductive elements for qubits," *Physical Review B*, vol. 82, no. 13, p. 134518, 2010.

[78] H. Mohebbi, O. Benningshof, I. Taminiau, G. Miao, and D. Cory, "Composite arrays of superconducting microstrip line resonators," *Journal of Applied Physics*, vol. 115, no. 9, p. 094502, 2014.

[79] A. Den Ouden, S. Wessel, E. Krooshoop, and H. Ten Kate, "Application of Nb/sub 3/Sn superconductors in high-field accelerator magnets," *IEEE Transactions on Applied Superconductivity*, vol. 7, no. 2, pp. 733–738, 1997.

[80] H. ten Kate, H. Weijers, and J. van Oort, "Critical current degradation in Nb/sub 3/Sn cables under transverse pressure," *IEEE transactions on applied superconductivity*, vol. 3, no. 1, pp. 1334–1337, 1993.

[81] H. Oguro, S. Awaji, K. Watanabe, M. Sugimoto, and H. Tsubouchi, "Prebending effect for mechanical and superconducting properties of Nb-rod-processed Cu-Nb internal-reinforced wires," *IEEE Transactions on Applied Superconductivity*, vol. 24, no. 3, pp. 1–4, 2014.

[82] V. Kushnir, S. Prischepa, C. Cirillo, and C. Attanasio, "Proximity effect and interface transparency in Nb/Cu multilayers," *Journal of Applied Physics*, vol. 106, no. 11, 2009.

[83] D. V. Baxter, S. Steenwyk, J. Bass, and W. Pratt Jr, "Resistance and spin-direction memory loss at Nb/Cu interfaces," *Journal of applied physics*, vol. 85, no. 8, pp. 4545–4547, 1999.

[84] A. Tesauro, A. Aurigemma, C. Cirillo, S. Prischepa, M. Salvato, and C. Attanasio, "Interface transparency and proximity effect in Nb/Cu triple layers realized by sputtering and molecular beam epitaxy," *Superconductor Science and Technology*, vol. 18, no. 1, p. 1, 2004.

[85] P. Kneisel, "Use of the titanium solid state gettering process for the improvement of the performance of superconducting rf cavities," *Journal of the Less Common Metals*, vol. 139, no. 1, pp. 179–188, 1988. [Online]. Available: http://dx.doi.org/10.1016/0022-5088(88)90340-2

[86] M. Pambianchi, L. Chen, and S. M. Anlage, "Complex conductivity of proximity-superconducting Nb/Cu bilayers," *Physical Review B*, vol. 54, no. 5, p. 3508, 1996.

[87] S. Zou, R. Bai, G. A. Hernandez, V. Gupta, Y. Cao, J. A. Sellers, C. D. Ellis, D. B. Tuckerman, and M. C. Hamilton, "Influence of fatigue and bending strain on critical currents of niobium superconducting flexible cables containing ti and cu interfacial layers," *IEEE Transactions on Applied Superconductivity*, In review.

[88] R. Bai, G. A. Hernandez, Y. Cao, J. A. Sellers, C. D. Ellis, D. B. Tuckerman, and M. C. Hamilton, "Microwave loss measurements of copper-clad superconducting niobium microstrip resonators on flexible polyimide substrates," *IEEE Transactions on Applied Superconductivity*, Accept.

[89] A. Gubin, K. Ilin, S. Vitusevich, M. Siegel, and N. Klein, "Dependence of magnetic penetration depth on the thickness of superconducting Nb thin films," *Physical Review B*, vol. 72, no. 6, p. 064503, 2005.

[90] J. H. Takemoto, C. M. Jackson, R. Hu, J. F. Burch, K. P. Daly, and R. W. Simon, "Microstrip resonators and filters using high-T_c superconducting thin films on $LaAlO_3$," *Magnetics, IEEE Transactions on*, vol. 27, no. 2, pp. 2549–2552, 1991.

[91] T. Miyakita, R. Hatakenaka, H. Sugita, M. Saitoh, and T. Hirai, "Development of a new multi-layer insulation blanket with non-interlayer-contact spacer for space cryogenic mission," *Cryogenics*, vol. 64, pp. 112–120, 2014.

[92] J. Demko, J. Fesmire, W. Johnson, and A. Swanger, "Cryogenic insulation standard data and methodologies," in *Advances in Cryogenic Engineering: Transactions of the Cryogenic Engineering Conference-CEC, American Institute of Physics*, vol. 59, 2014, pp. 463–470.

[93] J. Stark, K. Leonhard, and F. Bennett Jr, "Cryogenic thermal control technology summaries," *NASA Technical Brief*, p. 142p, Dec. 1974.

[94] W. Schwab, F. Boegelsack, and W. Menzel, "Multilayer suspended stripline and coplanar line filters," *Microwave Theory and Techniques, IEEE Transactions on*, vol. 42, no. 7, pp. 1403–1407, 1994.

[95] V. Gupta, J. A. Sellers, C. D. Ellis, S. Zou, G. A. Hernandez, R. Bai, Y. Cao, D. B. Tuckerman, and M. C. Hamilton, "Preserving nb superconducvity in thin film flexible structures," *Additional Papers and Presentations*, vol. 2016, no. DPC, pp. 002 075–002 094, 2016.

[96] D. Hafner, M. Dressel, and M. Scheffler, "Surface-resistance measurements using superconducting stripline resonators," *Review of Scientific Instruments*, vol. 85, no. 1, p. 014702, 2014.

[97] B. Dodson. (2012, Feb.) Quantum computer with separate CPU and memory represents significant breakthrough. [Online]. Available: http://www.gizmag.com/quantum-computer-von-neumann/21340/

Appendix A

Fabrication travelers

In this chapter, the fabrication process is described in greater detail. Each step is outlined with the appropriate step (e.g. bake, spin-on, etc.).

Step No.	Process	Parameters	Remarks
		Signal Line Definition	
1	Clean Kapton	Cut Kapton and Rinse in acetone/methanol/IPA	
2	Dehydration bake	Vacuum oven at 110°C for 20 minutes	
3	HMDS Coat	Place in HMDS beaker for 10 minutes	HMDS is found in an amber bottle
4	PR	AZ-9245: spin speed 1. 1700 RPM t=5s, a=500 RPM/s 2. 2200 RPM t=25s a= 1000 RPM/s	
5	Soft Bake	hotplate bake at 110°C t=90s	
6	Mask Alignment	Exposure time: 25 seconds Alignment gap: 25μm	Mask:M1
7	Development	3:1 DI Water: AZ 400k. Agitate solution prior to placing	
		wafer in solution. Rinse in DI water and N_2 blow dry Ratio: 150 mL of DI water, 50 mL Developer	2 minute development time
8	Nb Deposition	a. 2 minutes of ion milling at 1 kV. b. P= 1 kW/6.1 mTorr/30 minutes	
9	Lift-off	Rinse in acetone/methanol/IPA	
		Under Bump Metallization	
10	Dehydration Bake	Vacuum oven at 110°C for 20 minutes	
11	HMDS Coat	Place in HMDS beaker for 10 minutes	HMDS is found in an amber bottle
12	PR	AZ-9245: spin speed 1. 1700 RPM t=5s, a=500 RPM/s 2. 2200 RPM t=25s a= 1000 RPM/s	
13	Soft Bake	hotplate bake at 110°C t=90s	
14	Mask Alignment	Exposure time: 25 seconds Alignment gap: 25μm	Mask:UBM
15	Development	3:1 DI Water: AZ 400k. Agitate solution prior to placing	
		wafer in solution. Rinse in DI water and N_2 blow dry Ratio: 150 mL of DI water, 50 mL Developer	2 minute development time
16	UBM	a. 2 minutes of ion milling at 1 kV. b. Ti: 500 Å(2Å/s), Cu: 5000Å(2Å/s)	
17	Lift-off	Rinse in acetone/methanol/IPA	
		Ground Plane Metallization	
18	Backside Sample	Mount sample onto a wafer with the backside exposed	
19	Nb Deposition	a. 2 minutes of ion milling at 1 kV. b. P= 1 kW/6.1 mTorr/30 minutes	

Table A.1: Microstrip Traveler on Kapton 1/1

Step No.	Process	Parameters	Remarks
		Dielectric spin-on steps to achieve 20 μm	
1	Release Layer	a. 2 minutes of ion milling at 1 kV b. 250 Å Cr, 500 Å Al	
2	Dehydration Bake	Vacuum oven at 110°C for 20 minutes	
3	Adhesion Promoter	VM652. Spin speed 1. 500 RPM a=500 rpm/s 2. 3000 RPM a=1000 rpm/s t=30s	
4	Soft Bake	hotplate bake at 120°C t=60s	
5	PI Spin	1. 500 rpm a=500 rpm/s t=5s, 2. 1600 RPM a=1000 RPMs/s t=30s	
6	Bake	hotplate bake at 120°C t=5 mins.	
7	Cure	Profile 2 (350°C Cure)	
8	Plasma	150 W for 25 seconds	
9	Dehydration bake	vacuum oven at 110°C for 20 minutes	
10	Adhesion promoter	VM652. Spin speed 1. 500 RPM a=500 rpm/s 2. 3000 RPM a=1000 rpm/s t=30s	
11	Soft bake	hotplate bake at 120°C t=60s	
12	PI Spin	1. 500 rpm a=500 rpm/s t=5s, 2. 1600 RPM a=1000 RPMs/s t=30s	
13	Bake	hotplate bake at 120°C t=5 mins.	
14	Cure	Profile 2 (350°C Cure)	
		Signal line definition	
15	Dehydration bake	vacuum oven at 110°C for 20 minutes	
16	HMDS Coat	Place in HMDS beaker for 10 minutes	HMDS is found in an amber bottle
17	PR	AZ-9245: spin speed 1. 1700 RPM t=5s, a=500 RPM/s 2. 2200 RPM t=25s a= 1000 RPM/s	
18	Soft bake	hotplate bake at 110°C t=90s	
19	Mask alignment	exposure time: 25 seconds Alignment gap: 25μm	Mask:M1
20	Development	3:1 DI Water: AZ 400k. Agitate solution prior to placing wafer in solution. Rinse in DI water and N_2 blow dry Ratio: 150 mL of DI water, 50 mL Developer	2 minute development time
21	Nb Deposition	a. 2 minutes of ion milling at 1 kV. b. P= 1 kW/6.1 mTorr/30 minutes	
22	Lift-off	Rinse in acetone/methanol/IPA	

Table A.2: Microstrip Traveler on Polymide 1/2

Step No.	Process	Parameters	Remarks
		Under bump metallization	
23	Dehydration bake	Vacuum oven at 110°C for 20 minutes	
24	HMDS coat	Place in HMDS beaker for 10 minutes	HMDS is found in an amber bottle
25	PR	AZ-9245: spin speed 1. 1700 RPM t=5s, a=500 RPM/s 2. 2200 RPM t=25s a= 1000 RPM/s	
26	Soft Bake	hotplate bake at 110°C t=90s	
27	Mask alignment	Exposure time: 25 seconds Alignment gap: 25μm	Mask:UBM
28	Development	3:1 DI Water: AZ 400k. Agitate solution prior to placing wafer in solution. Rinse in DI water and N_2 blow dry Ratio: 150 mL of DI water, 50 mL Developer	2 minute development time
29	UBM	a. 2 minutes of ion milling at 1 kV. b. Ti: 500 Å(2Å/s), Cu: 5000Å(2Å/s)	
30	Lift-off	Rinse in acetone/methanol/IPA	
		Release Sample & Ground Plane Metallization	
28	PR	AZ-9245: spin speed 1. 1700 RPM t=5s, a=500 RPM/s 2. 2200 RPM t=25s a= 1000 RPM/s	
31	Soft Bake	hotplate bake at 110°C t=90s	
32	Dice samples	Use profile ANG/5inch profile	
33	Salt Solution	2M (Moles/L) solution of NaCl based on 1L of H20. (a) Pour 500 mL of DI water into beaker (b) 117 gramsof NaCl. Pour into beaker and fill with water until 1L	
34	Sample Release	Connect ground to the metal mesh, and apply 0.6 V to the sample	
35	Surface clean	rinse in acetone/methanol/IPA, followed by DI water	
36	Backside Sample	Mount sample onto a wafer with the backside exposed	
37	Nb Deposition	a. 2 minutes of ion milling at 1 kV. b. P= 1 kW/6.1 mTorr/30 minutes	

Table A.3: Microstrip Traveler on Polyimide 2/2

Step No.	Process	Parameters	Remarks
		Dielectric spin-on steps to achieve 20 μm	
1	Release Layer	a. 2 minutes of ion milling at 1 kV b. 250 Å Cr, 500 Å Al	
2	Dehydration bake	Vacuum oven at 110°C for 20 minutes	
3	Adhesion promoter	VM652. Spin speed 1. 500 RPM a=500 rpm/s 2. 3000 RPM a=1000 rpm/s t=30s	
4	Soft bake	hotplate bake at 120°C t=60s	
5	PI Spin	1. 500 rpm a=500 rpm/s t=5s, 2. 1600 RPM a=1000 RPMs/s t=30s	
6	Bake	hotplate bake at 120°C t=5 mins.	
7	Cure	Profile 2 (350°C Cure)	
8	Plasma	150 W for 25 seconds	
9	Dehydration bake	Vacuum oven at 110°C for 20 minutes	
10	Adhesion promoter	VM652. Spin speed 1. 500 RPM a=500 rpm/s 2. 3000 RPM a=1000 rpm/s t=30s	
11	Soft bake	hotplate bake at 120°C t=60s	
12	PI Spin	1. 500 rpm a=500 rpm/s t=5s, 2. 1600 RPM a=1000 RPMs/s t=30s	
13	Bake	hotplate bake at 120°C t=5 mins.	
14	Cure	Profile 2 (350°C Cure)	
		Signal Line Definition	
15	Dehydration Bake	Vacuum Oven at 110°C for 20 minutes	
13	HMDS Coat	Place in HMDS beaker for 10 minutes	HMDS is found in an amber bottle
14	PR	AZ-9245: spin speed 1. 1700 RPM t=5s, a=500 RPM/s 2. 2200 RPM t=25s a= 1000 RPM/s	
15	Soft Bake	hotplate bake at 110°C t=90s	
16	Mask alignment	Exposure time: 25 seconds Alignment gap: 25μm	Mask:M1
17	Development	3:1 DI Water: AZ 400k. Agitate solution prior to placing wafer in solution. Rinse in DI water and N_2 blow dry Ratio: 150 mL of DI water, 50 mL Developer	2 minute development time
18	Nb Deposition	a. 2 minutes of ion milling at 1 kV. b. P= 1 kW/6.1 mTorr/30 minutes	
19	Lift-off	Rinse in acetone/methanol/IPA	

Table A.4: Embedded Microstrip Traveler 1/2

Step No.	Process	Parameters	Remarks
		Top Layer Polyimide spin-on	
20	Dehydration bake	Vacuum oven at 110°C for 20 minutes	
21	Adhesion promoter	VM652. Spin speed 1. 500 RPM a=500 rpm/s 2. 3000 RPM a=1000 rpm/s t=30s	
22	Soft bake	hotplate bake at 120°C t=60s	
23	PI Spin	1. 500 rpm a=500 rpm/s t=5s, 2. 1600 RPM a=1000 RPMs/s t=30s	
24	Bake	hotplate bake at 120°C t=5 mins.	
25	Cure	Profile 6 (225°C Cure)	
		Under Bump Metallization	
26	Dehydration Bake	Vacuum oven at 110°C for 20 minutes	
27	HMDS Coat	Place in HMDS beaker for 10 minutes	HMDS is found in an amber bottle
28	PR	AZ-9245: spin speed 1. 1700 RPM t=5s, a=500 RPM/s 2. 2200 RPM t=25s a= 1000 RPM/s	
29	Soft Bake	hotplate bake at 110°C t=90s	
30	Mask Alignment	Exposure time: 25 seconds Alignment gap: 25μm	Mask:UBM
31	Development	3:1 DI Water: AZ 400k. Agitate solution prior to placing wafer in solution. Rinse in DI water and N_2 blow dry Ratio: 150 mL of DI water, 50 mL Developer	2 minute development time
32	UBM	a. 2 minutes of ion milling at 1 kV. b. Ti: 500 Å(2Å/s), Cu: 5000Å(2Å/s)	
33	Lift-off	Rinse in acetone/methanol/IPA	
		Release Sample & Ground Plane Metallization	
34	PR	AZ-9245: spin speed 1. 1700 RPM t=5s, a=500 RPM/s 2. 2200 RPM t=25s a= 1000 RPM/s	
35	Soft Bake	hotplate bake at 110°C t=90s	
36	Dice samples	Use profile ANG/5inch profile	
37	Salt Solution	2M (Moles/L) solution of NaCl based on 1L of H20. (a) Pour 500 mL of DI water into beaker (b) 117 gramsof NaCl. Pour into beaker and fill with water until 1L	
38	Sample Release	Connect ground to the metal mesh, and apply 0.6 V to the sample	
39	Surface clean	rinse in acetone/methanol/IPA, followed by DI water	
40	Backside Sample	Mount sample onto a wafer with the backside exposed	
41	Nb Deposition	a. 2 minutes of ion milling at 1 kV. b. P= 1 kW/6.1 mTorr/30 minutes	

Table A.5: Embedded Microstrip Traveler 2/2